

VECTOR FILTERING TECHNIQUE FOR RECOVERY OF
STATIONARY STOCHASTIC PROCESSES
CONTAMINATED BY BROAD-BAND NOISE

CENTRE FOR NEWFOUNDLAND STUDIES

**TOTAL OF 10 PAGES ONLY
MAY BE XEROXED**

(Without Author's Permission)

EUGENE VICTOR GUY



**VECTOR FILTERING TECHNIQUE
FOR RECOVERY OF STATIONARY STOCHASTIC PROCESSES
CONTAMINATED BY BROAD-BAND NOISE**

By

© Eugene Victor Guy, B.Sc., B.Ed., M.Sc.

A thesis submitted to the School of Graduate
Studies in partial fulfilment of the
requirements for the degree of
Master of Engineering

Faculty of Engineering and Applied Science
Memorial University of Newfoundland

May, 1995



National Library
of Canada

Acquisitions and
Bibliographic Services Branch

395 Wellington Street
Ottawa, Ontario
K1A 0N4

Bibliothèque nationale
du Canada

Direction des acquisitions et
des services bibliographiques

395, rue Wellington
Ottawa (Ontario)
K1A 0N4

Your file *Votre référence*

Our file *Notre référence*

THE AUTHOR HAS GRANTED AN IRREVOCABLE NON-EXCLUSIVE LICENCE ALLOWING THE NATIONAL LIBRARY OF CANADA TO REPRODUCE, LOAN, DISTRIBUTE OR SELL COPIES OF HIS/HER THESIS BY ANY MEANS AND IN ANY FORM OR FORMAT, MAKING THIS THESIS AVAILABLE TO INTERESTED PERSONS.

L'AUTEUR A ACCORDE UNE LICENCE IRREVOCABLE ET NON EXCLUSIVE PERMETTANT A LA BIBLIOTHEQUE NATIONALE DU CANADA DE REPRODUIRE, PRETER, DISTRIBUER OU VENDRE DES COPIES DE SA THESE DE QUELQUE MANIERE ET SOUS QUELQUE FORME QUE CE SOIT POUR METTRE DES EXEMPLAIRES DE CETTE THESE A LA DISPOSITION DES PERSONNE INTERESSEES.

THE AUTHOR RETAINS OWNERSHIP OF THE COPYRIGHT IN HIS/HER THESIS. NEITHER THE THESIS NOR SUBSTANTIAL EXTRACTS FROM IT MAY BE PRINTED OR OTHERWISE REPRODUCED WITHOUT HIS/HER PERMISSION.

L'AUTEUR CONSERVE LA PROPRIETE DU DROIT D'AUTEUR QUI PROTEGE SA THESE. NI LA THESE NI DES EXTRAITS SUBSTANTIELS DE CELLE-CI NE DOIVENT ETRE IMPRIMES OU AUTREMENT REPRODUITS SANS SON AUTORISATION.

ISBN 0-612-06124-8

Canada

Abstract

The objective of this project has been to develop a filtering technique which will enable the recovery of a wide-sense stationary, stochastic signal process, from a two-dimensional image. It is assumed that the image is contaminated by a stationary broad-band noise process, having a spatial extent of correlation, represented by c , which is much less than the spatial extent of correlation within the signal process. Under such conditions, it is possible to derive a three-channel Wiener filter which operates on the past values of a coherent data sequence, in order to predict a future value. By setting the prediction gap, α , to be greater than c , the predicted output sequence will be a noise-suppressed version of the input. The three-channel filter accepts as input, three rows of the image, and then produces a single output which is a filtered estimate of the signal process occurring within the middle row of the input triplet. Each row within this triplet is separated by a distance, β , which is held constant for all row triplets during the filtering operation. After operating on all possible row triplets, the same procedure is repeated for column triplets. It has been demonstrated that the three-channel filter has a greater capacity for noise-suppression, when compared to single-channel versions. By choosing the value of β to be greater than c , this noise suppression capability is optimized.

This research has verified that the three-channel Wiener filter is effective in suppressing correlated speckle noise, within ocean wave scenes imaged by airborne Synthetic Aperture Radar. However, due to the exponentially-damped nature of the correlation functions which characterize the bandpass signal process within such images, it has also been shown that the filtered estimates are directly dependent upon the values chosen for α and β . In fact, if two different filtering operators are derived, each with a different combination of values for α and β , then they will each produce a different filtered estimate after operating on the same input image. Consequently, the accuracy of the filtering operation will vary according to the choices which are

made regarding these parameters. The most accurate filtered estimates of the bandpass process are achieved with small parametric values. Since α must assume a value which is greater than c , and since it is preferable that β should also, it logically follows that the extent of noise correlation within any image will predetermine the degree of accuracy which can be achieved by use of this technique.

The three-channel Wiener filtering technique will have practical noise-suppression applications, relating to the extraction of more accurate wave feature information from speckle-contaminated SAR images of ocean scenes. Furthermore, since the use of large α and β restricts recovery to only a portion of a bandpass signal, this technique may be suitable for the isolation and enhancement of low-frequency, low-power wave components, which may be otherwise obscured by higher-frequency wind-generated waves.

Acknowledgements

Valuable support from a number of parties, has been very much appreciated during the execution of this project. Grateful acknowledgement is extended to the following:

Dr. Rafaat H. Khan (Centre for Cold Ocean Resources Engineering / Faculty of Engineering and Applied Science) undertook the role of Supervisor during this research. He provided many pertinent insights into the broad array of problems which were encountered while developing the filtering technique.

The efforts of Dr. Paris Vachon and Ms. Cathryn Bjerkelund, of the Canada Centre for Remote Sensing, were instrumental in arranging for the provision of SAR data. Dr. Vachon also provided information which was useful in developing an understanding of the attributes of SAR data processing.

Mr. Kenneth J. Hickey (Centre for Cold Ocean Resources Engineering) provided the FORTRAN program, which was used in order to extract the SAR data from the CCRS tape format.

The Government of Newfoundland and Labrador, Department of Education, provided financial assistance in the form of an Atlantic Accord Career Development Scholarship.

The Centre for Computer-Aided Engineering (CCAE), within the Faculty of Engineering, provided access to computer resources and expertise which were crucial to the completion of this project.

The Centre for Cold Ocean Resources Engineering (C-CORE) provided access to all in-house facilities during the course of this research.

Table of Contents

CHAPTER ONE: PROJECT OVERVIEW AND DISCUSSION OF BACKGROUND MATERIAL	
1.1	Introduction and Specification of Scope 1
1.2	Nature of the Speckle Phenomenon 4
1.2.1	The Process of Speckle Formation 4
1.2.2	Modelling the Speckle and Signal Interaction 6
1.2.3	Inadequacies of Existing Speckle Filters 8
1.2.4	Speckle and Signal Model for SAR Images of Ocean Scenes 10
1.3	Motivation for New Approach to Speckle Suppression 11
CHAPTER TWO: ANALYTICAL FORMULATION OF TECHNIQUE FOR SUPPRESSION OF BROAD-BAND COHERENT NOISE	
2.1	Introduction 14
2.2	Formal Statement of Problem 14
2.3	An Adaptive Filtering Solution to the Signal Recovery Problem 17
2.4	Correlation Characteristics of Imaged Stationary Processes 18
2.4.1	General Derivation of Two-Dimensional and One-Dimensional Correlation Functions 18
2.4.2	Analytical Form of the Two-Dimensional ACF and its One-Dimensional Components 19
2.4.3	Spectral Characteristics Within the Signal Component of the CCF 24
2.5	Block-Adaptive Wiener Filter for Scalar Stochastic Processes 30
2.5.1	Overview 30
2.5.2	Scalar Wiener Filter: Mathematical Derivation 32
2.5.3	Prediction Effectiveness of the Scalar Wiener Filter 34
2.5.4	Scalar Wiener Filter: Frequency-Domain Transfer Function 36

2.5.5	The Scalar Filtering Operation	39
2.6	Block-Adaptive Wiener Filter for Vector Stochastic Processes	46
2.6.1	Overview	46
2.6.2	Three-Channel Wiener Filter: Mathematical Derivation	48
2.6.3	Three-Channel Wiener Filter: Frequency-Domain Transfer Function	51
2.6.4	Achieving Optimum Noise Suppression with the Three-Channel Wiener Filter	54
2.7	Vector Filtering Technique for Reduction of Coherent Noise	56
2.7.1	Overview	56
2.7.2	Minimizing Phase Distortions in the Row and Column Estimates	58
2.7.3	Selection of CCF and ACF Information for Vector Filtering in the Columns	60
2.8	Summary	62

CHAPTER THREE: RESULTS FROM NUMERICAL SIMULATIONS INVOLVING CASE I CORRELATION DATA

3.1	Introduction	63
3.2	Characteristics of Simulated Data Sets	66
3.3	Determination of Optimum Operational Parameters for Filtering Technique	72
3.3.1	Overview	72
3.3.2	Noise Suppression Advantage of a Three-Channel Filter Over the One-Channel Version	74
3.3.3	Influence of α in Determining Noise-Suppression Efficiency	77
3.3.4	Influence of β in Determining Noise-Suppression Efficiency	83
3.3.5	Optimum Method for Selecting Correlation Data When Deriving Column Operators	87
3.4	Evaluation of Filtering Technique for Large ξ	91
3.4.1	Filtering Operations on Simulated Data Sets	91

3.4.2	Influence of α and β Parameters Upon Filter Performance	97
3.5	Summary	103
CHAPTER FOUR: APPLICATION OF FILTERING TECHNIQUE TO OCEAN WAVE SCENES WITHIN SAR IMAGERY		
4.1	Introduction	104
4.2	Image Characteristics	104
4.3	Correlation Characteristics of Imaged Processes	111
4.3.1	Estimation of Two-Dimensional and One-Dimensional Correlation Functions	111
4.3.2	Estimating c , the Spatial Extent of Noise Correlation	120
4.4	Results from Vector Filtering Operations	123
4.4.1	Overview	123
4.4.2	Comparison of Unfiltered and Filtered Image Processes for Nov. 14	124
4.4.3	Comparison of Unfiltered and Filtered Image Processes for Nov. 18	132
4.5	Summary	137
CHAPTER FIVE: INFLUENCE OF WOLD'S DECOMPOSITION UPON VECTOR FILTER FOR CASE II CORRELATION DATA		
5.1	Introduction	140
5.2	Cross-Coherence Function Obtained from Nov. 14 and Nov. 18 Images	141
5.3	Magnitude Response Variations Induced by Changing α and β	146
5.4	Assessment of Recovered Images for Impact Due to Changes in α and β	152
5.5	Summary	163
CHAPTER SIX: CONCLUSIONS		
6.1	Overview	165

6.2	Significant Findings	169
6.3	Practical Applications of Filtering Technique	172
6.4	General Conclusions and Recommendations	173
	REFERENCES	175
APPENDIX I:	DISCRETE FOURIER TRANSFORM REPRESENTATION OF THE SIGNAL CROSS-CORRELATION FUNCTION	178
APPENDIX II:	PROCESSING ALGORITHMS FOR IMPLEMENTATION OF FILTERING TECHNIQUE	185
APPENDIX III:	FREQUENCY RESPONSE MAGNITUDE CHARACTERISTICS OF VECTOR FILTERS	196
APPENDIX IV:	FREQUENCY RESPONSE OF VECTOR FILTER AS FUNCTION OF VARIATIONS IN α AND β	201
APPENDIX V:	FFT ANALYSIS OF RECOVERED IMAGES PRESENTED IN CHAPTER FIVE	206

List of Figures

3.1:	Simulated noise-free wavefields, and wavefield-plus-noise composites with -12 dB SNR.	68
3.2:	One-dimensional autocorrelation functions, for row and column components of the signal-plus-noise processes shown in Figure 3.1.	69
3.3:	<i>1024</i> -point FFT's, showing relative magnitudes of normalized power within row and column components of the noise-free wavefields in Figure 3.1.	70
3.4:	<i>1024</i> -point FFT's, showing relative magnitudes of normalized power within row and column components of the signal-plus-noise composite processes in Figure 3.1.	71
3.5:	Reference wavefield recovered with a standard-attribute operator, $\xi=20$, is shown in (a). This result is definitely superior to the test image obtained with a single-channel operator, shown in (b).	75
3.6:	<i>1024</i> -point FFT's, showing relative magnitudes of normalized power within row and column components of recovered wavefields in Figure 3.5.	76
3.7:	Results obtained for $T_r(f)$, based on <i>1024</i> -point FFT's from the rows and columns of images in Figure 3.5.	78
3.8:	Reference wavefield recovered with a standard-attribute operator, $\xi=20$, is shown in (a). This result is undeniably superior to the test image obtained with $\alpha=1$, shown in (b).	79
3.9:	<i>1024</i> -point FFT's, showing relative magnitudes of normalized power within row and column components of the recovered wavefields shown in Figure 3.8.	81
3.10:	Results obtained for $T_r(f)$, based on <i>1024</i> -point FFT's from the rows and columns of images in Figure 3.8.	82
3.11:	Reference wavefield recovered with a standard-attribute operator, $\xi=20$, is shown in (a). This result is noticeably superior to the test image obtained with $\beta=1$, shown in (b).	84
3.12:	<i>1024</i> -point FFT's, showing relative magnitudes of normalized power within row and column components of the recovered wavefields shown in Figure 3.11.	85
3.13:	Results obtained for $T_r(f)$, based on <i>1024</i> -point FFT's from the rows and columns of images in Figure 3.11.	86

3.14:	Reference wavefield recovered with a standard-attribute operator, $\xi=20$, is shown in (a). This result is clearly superior to the test image, shown in (b), obtained after deriving the column filter from the row-filtered image.	88
3.15:	1024 -point FFT's, showing relative magnitudes of normalized power within row and column components of the recovered wavefields shown in Figure 3.12.	89
3.16:	Results obtained for $T_r(f)$, based on 1024 -point FFT's from the rows and columns of images in Figure 3.14.	90
3.17:	Results obtained with three-channel filter, for $\xi=60$. The normalized power spectra in (c) and (d) are 1024 -point FFT's, obtained from the recovered wavefield in (b). The original noise-free wavefield, and wavefield-plus-noise composite, are seen in (a).	92
3.18:	Results obtained with three-channel filter, for $\xi=150$. The normalized power spectra in (c) and (d) are 1024 -point FFT's, obtained from the recovered wavefield in (b). The original noise-free wavefield, and wavefield-plus-noise composite, are seen in (a).	94
3.19:	Results for $T_r(f)$, based on 1024 -point FFT's which were obtained from noise-contaminated and filtered versions of the simulated wavefields.	95
3.20:	Magnitude response of the vector Wiener filter, as a function of adjustments to correlation shape parameters α and β	98
3.21:	Wavefields recovered using standard-attribute operator, $\xi=150$, for selected values of correlation shape parameter α , with constant value of shape parameter $\beta=2$	101
3.22:	Wavefields recovered using standard-attribute operator, $\xi=150$, for selected values of correlation shape parameter α , with shape parameter $\beta=\alpha$	102
4.1:	Geometry of SAR imaging process.	106
4.2:	Means (bottom trace) and positive standard deviations (top trace), for the row and column components of Nov. 14 and Nov. 18 signal-plus-noise processes.	109
4.3:	Normalized autocorrelation data, obtained from 1024×1024 subscene of Nov. 14 image.	112
4.4:	Normalized autocorrelation data, obtained from 1024×1024 subscene of Nov. 18 image.	113
4.5:	Normalized one-dimensional autocorrelation functions, for the row and column components of the Nov. 14 and Nov. 18 signal-plus-noise processes.	116
4.6:	Normalized one-dimensional row and column CCF's for Nov. 14 image, extracted from the two-dimensional ACF of Figure 4.3.	118

4.7:	Normalized one-dimensional row and column CCF's for Nov. 18 image, extracted from the two-dimensional ACF of Figure 4.4.	119
4.8:	Normalized ACF and CCF sections, from column components of Nov. 14 and Nov. 18 images.	121
4.9:	Noise-contaminated SAR image is shown in (a), for Nov. 14 wavefield. The recovered wavefield, based on standard-attribute operator with $\alpha=\beta=3$, $\xi=200$, is shown in (b).	125
4.10:	Enlarged subscenes from the unfiltered and filtered images in Figure 4.9.	127
4.11:	1024-point FFT's, for the row and column components of the unfiltered and filtered images shown in Figure 4.9.	129
4.12:	Power transfer functions, mapping unfiltered row and column spectra to their respective filtered spectra, for Nov. 14 image.	131
4.13:	Noise-contaminated SAR image is shown in (a), for the Nov. 18 wavefield. The recovered wavefield, based on standard-attribute operator with $\alpha=\beta=3$, $\xi=200$, is shown in (b).	133
4.14:	Enlarged subscenes from the unfiltered and filtered images in Figure 4.13.	135
4.15:	1024-point FFT's, for the row and column components of the unfiltered and filtered images shown in Figure 4.13.	136
4.16:	Power transfer functions, mapping unfiltered row and column spectra to their respective filtered spectra, for Nov. 18 image.	138
5.1:	Numerical estimates of $\gamma_{xy}^2(f \theta, \beta)$, $1 \leq \beta \leq 50$, obtained from the Nov. 14 and Nov. 18 SAR images.	142
5.2:	Magnitude response surfaces derived from column component of Nov. 14 image, for fixed β and varying α . Note the cyclic patterns parallel to the α -axis.	147
5.3:	Magnitude response surfaces derived from column component of Nov. 14 image, for jointly varying $\beta=\alpha$	148
5.4:	Realizations of Nov. 14 bandpass process for $\beta=3$, at three distinct values of α . . .	153
5.5:	Realizations of Nov. 14 bandpass process for $\beta=\alpha$, at three distinct values of α . . .	155
5.6:	Realizations of Nov. 18 bandpass process for $\beta=3$, at three distinct values of α . . .	157
5.7:	Normalized power spectra from column components of recovered wavefield realizations for Nov. 18, are shown in (a) and (b). The power transfer function which maps (a) into (b), is shown in (c).	159
5.8:	Realizations of Nov. 18 bandpass process for $\beta=\alpha$, at three distinct values of α . . .	161

III.1:	Magnitude of frequency response, for filters used in recovery of one-component simulated wavefield presented in Figure 3.17.	197
III.2:	Magnitude of frequency response, for filters used in recovery of three-component simulated wavefield presented in Figure 3.18.	198
III.3:	Magnitude of frequency response, for filters used in recovery of Nov. 14 bandpass process presented in Figure 4.9.	199
III.4:	Magnitude of frequency response, for filters used in recovery of Nov. 18 bandpass process presented in Figure 4.13.	200
IV.1:	Magnitude frequency response surfaces of Nov. 14 row filter, for varying α with fixed β , shown in (a), (b) and (c), and jointly varying $\beta=\alpha$, shown in (d), (e), and (f).	202
IV.2:	Magnitude frequency response surfaces of Nov. 14 column filter, for varying α with fixed β , shown in (a), (b) and (c), and jointly varying $\beta=\alpha$, shown in (d), (e), and (f).	203
IV.3:	Magnitude frequency response surfaces of Nov. 18 row filter, for varying α with fixed β , shown in (a), (b) and (c), and jointly varying $\beta=\alpha$, shown in (d), (e), and (f).	204
IV.4:	Magnitude frequency response surfaces of Nov. 18 column filter, for varying α with fixed β , shown in (a), (b) and (c), and jointly varying $\beta=\alpha$, shown in (d), (e), and (f).	205
V.1:	FFT analysis for recovered images shown in Figure 5.4.	207
V.2:	FFT analysis for recovered images shown in Figure 5.5.	208
V.3:	FFT analysis for recovered images shown in Figure 5.6.	209
V.4:	FFT analysis for recovered images shown in Figure 5.8.	210

List of Principal Symbols

$g(i,j)$	two-dimensional stationary stochastic signal process, generally assumed to be bandpass.
$n(i,j)$	two-dimensional broad-band stationary stochastic noise process.
$x(i,j)$	additive superposition of $g(i,j)$ and $n(i,j)$.
$g_j(i)$	j 'th element within i 'th row component of $g(i,j)$.
$n_j(i)$	j 'th element within i 'th row component of $n(i,j)$.
$x_j(i)$	j 'th element within i 'th row component of $x(i,j)$.
α	forward prediction gap of linear filtering operator.
β	cross-row prediction gap of linear filtering operator.
$\hat{g}_j(j \alpha,\beta)$	j 'th filtered point-estimate of i 'th row scalar signal process, obtained from operation on the <i>noise-contaminated</i> process points, $x_j(j)$, $j=1,2,\dots,N_R$.
$\tilde{g}_j(j \alpha,\beta)$	j 'th filtered point-estimate of i 'th row scalar signal process, obtained from operation on the <i>noise-free</i> signal process points, $g_j(j)$, $j=1,2,\dots,N_R$.
$\hat{n}_j(j \alpha,\beta)$	j 'th filtered point-estimate of i 'th row scalar noise process, obtained from operation on the noise process points, $n_j(j)$, $j=1,2,\dots,N_R$.
$[x_j(j)]_{j=1}^{\xi}$	j 'th element of three-channel vector process, centred on image row i .
$x_{i;\alpha(i)}$	block vector comprised of the ξ elements, $[x_j(j)]_{j=1}^{\xi}$.
$[\hat{g}_j(j \alpha,\beta)]_{j=1}^{\xi}$	j 'th element of i 'th three-channel signal process estimate, centred on row i .
N_C, N_R	number of image pixels along column dimension and row dimension respectively.
x_i	i 'th subset of size N_R , consisting of $x_j(j)$, $j=1,2,\dots,N_R$.
X	set of size $N_C \times N_R$, consisting of x_i , $i=1,2,\dots,N_C$.
$x_{i;\beta}$	three-channel subset, centred on row i and consisting of block vector elements $[x_j(j)]_{j=1}^{\xi}$, over all $j=1,2,\dots,N_R$ inclusive.
X_j	three-channel set consisting of $x_{i;\beta}$, for all $i=\beta+1,\beta+2,\dots,N_C-\beta$, inclusive.
\hat{g}_i	i 'th subset of size N_R , consisting of $\hat{g}_j(j \alpha,\beta)$, $j=1,2,\dots,N_R$.

\hat{G}	set of size $N_c \times N_R$, consisting of $\hat{g}_i, i=1,2,\dots,N_c$.
g_i, G	desired image components which are estimated by \hat{g}_i and \hat{G} respectively.
τ_c, τ_R	correlation lags in column and row dimensions respectively.
$d_{c,k}, d_{R,k}$	column and row damping terms, associated with k 'th negative-exponential component of $R_{xx}(\tau_c, \tau_R)$.
$\omega_{c,k}, \omega_{R,k}$	column and row k 'th sinusoidal components, within two-dimensional signal ACF and one-dimensional signal ACF/CCF.
c	spatial extent of noise correlation in both row and column dimensions.
$R_{gg}(\tau_c, \tau_R)$	two-dimensional autocorrelation function of $g(i,j)$.
$R_{nn}(\tau_c, \tau_R)$	two-dimensional autocorrelation function of $n(i,j)$.
$R_{xx}(\tau_c, \tau_R)$	two-dimensional autocorrelation function of $x(i,j)$.
$r_{gR}(\tau_R 0)$	one-dimensional autocorrelation function, for row data points $g(j)$.
$r_{nR}(\tau_R 0)$	one-dimensional autocorrelation function, for row data points $n(j)$.
$r_{xR}(\tau_R 0)$	one-dimensional autocorrelation function, for row data points $x(j)$.
$r_{gR}(\tau_R \beta)$	one-dimensional cross-correlation function, between row data points $g(j)$ and $g_{i,\beta}(j)$.
$r_{nR}(\tau_R \beta)$	one-dimensional cross-correlation function, between row data points $n(j)$ and $n_{i,\beta}(j)$.
$r_{xR}(\tau_R \beta)$	one-dimensional cross-correlation function, between row data points $x(j)$ and $x_{i,\beta}(j)$.
$r_{gR}(\tau_R)$	subset of coefficients $r_{gR}(\tau_R \beta)$, of size N_R , for which τ_R is non-negative.
$r_{nR}(\tau_R)$	subset within $r_{gR}(\tau_R)$ of size ξ , for which $\theta \leq \alpha \leq \tau_R \leq \alpha + \xi - 1$.
$[r_{gR}(\tau_R \pm \Xi \beta)]_{j,j}$	3×3 matrix comprised of elements $r_{gR}(\tau_R \pm 2\beta)$, $r_{gR}(\tau_R \pm \beta)$, and $r_{gR}(\tau_R 0)$.
$[r_{nR}(\tau_R \pm \Xi \beta)]_{j,j}$	3×3 matrix comprised of elements $r_{nR}(\tau_R \pm 2\beta)$, $r_{nR}(\tau_R \pm \beta)$ and $r_{nR}(\tau_R 0)$.
$R_{t,t}, R_{R,t}$	scalar-element correlation matrix and block-element correlation matrix, used to derive scalar and three-channel vector Wiener filters respectively.
$r_{t,t}, r_{R,t}$	scalar-element correlation vector and block-element correlation vector, used to derive scalar and three-channel vector Wiener filters respectively.

$\gamma_v^2(f \alpha, \beta)$	cross-spectral power coherence function, between rows separated by distance β , for specified α .
ξ	length of filter impulse response.
h_{xy}	filter impulse response function, mapping row (or Channel) y into row (or Channel) x .
$h_{\nu}(r \alpha, \beta)$	r 'th element of filter impulse response function which maps row (or Channel) y into row (or Channel) x .
h	set which consists of $h_{\nu}(r \alpha, \beta)$, for all $r=0, 1, \dots, \xi-1$.
$[h_{\nu}(r \alpha, \beta)]_{1..3}$	r 'th 3×3 element of three-channel impulse response block vector.
$h_{(ij)}$	set which consists of $[h_{\nu}(r \alpha, \beta)]_{1..3}$, for all $r=0, 1, \dots, \xi-1$.
$h_{1..1}, h_{3..3}$	scalar and block-element impulse response vectors, containing scalar and three-channel transfer function elements $h_{\nu}(r \alpha, \beta)$ and $[h_{\nu}(r \alpha, \beta)]_{1..1}$ respectively.
$N_{\nu}(f \beta)$	DFT representation of $r_{\nu\nu}(\tau_R \beta)$.
$N_{\nu}(f 0)$	DFT representation of $r_{\nu\nu}(\tau_R 0)$.
$\hat{N}_{\nu}(f \alpha, \beta)$	DFT representation of $\hat{n}_{\nu}(f \alpha, \beta)$.
$[N_{\nu}(f \pm\Xi\beta)]_{1..3}$	3×3 matrix consisting of elements $N_{\nu}(f \pm 2\beta)$, $N_{\nu}(f \pm\beta)$ and $N_{\nu}(f 0)$.
$G_{\nu}(f \alpha, \beta)$	α -dependent DFT representation of signal correlation component $r_{xy}(\tau_R \beta)$.
$G_{\nu}(f \alpha, 0)$	α -dependent DFT representation of signal correlation component $r_{xy}(\tau_R 0)$.
$G_{\nu}(f \beta)$	α -independent DFT representation of signal correlation component $r_{xy}(\tau_R \beta)$.
$G_{\nu}(f 0)$	α -independent DFT representation of signal correlation component $r_{xy}(\tau_R 0)$.
$[G_{\nu}(f \alpha, \pm\Gamma\beta)]_{1..1}$	3×1 vector consisting of elements $G_{\nu}(f \alpha, \pm\beta)$ and $G_{\nu}(f \alpha, 0)$.
$[G_{\nu}(f \pm\Xi\beta)]_{1..3}$	3×3 matrix consisting of elements $G_{\nu}(f \pm 2\beta)$, $G_{\nu}(f \pm\beta)$ and $G_{\nu}(f 0)$.
$\hat{G}_{\nu}(f \alpha, \beta)$	DFT representation of $\hat{g}_{\nu}(f \alpha, \beta)$.
$\check{G}_{\nu}(f \alpha, \beta)$	DFT representation of $\check{g}_{\nu}(f \alpha, \beta)$.
$H_{\nu}(f \alpha, \beta)$	DFT representation of $h_{\nu}(r \alpha, \beta)$.

$\{H_n(f, \alpha, \beta)\}_{1..J}$	$3 \times J$ vector of elements $H_n(f, \alpha, \beta)$.
$T_i(f)$	\log_{10} -scaled power transfer function.
$P_{NIN}(f)$	normalized power spectra at input to $T_i(f)$.
$P_{NOUT}(f)$	normalized power spectra at output from $T_i(f)$.
$\mathbb{G}(f)_k$	k 'th Fourier component within $G_n(f, \alpha, \beta)$, discussed in Appendix I.

CHAPTER ONE

PROJECT OVERVIEW AND DISCUSSION OF BACKGROUND MATERIAL

1.1 Introduction and Specification of Scope

The mathematical technique which has been developed during this project will achieve noise suppression within a digital image, provided certain statistical assumptions are satisfied by the image data. Subject to these assumptions, any two-dimensional wide-sense stationary (WSS) wavefield which has been contaminated by WSS broad-band correlated noise, may be processed via this technique in order to obtain a noise-suppressed version. The outcome of such processing will be a filtered image, within which the previously occluded wavefield is presented with enhanced clarity. Within the scope of this thesis, utilization of the technique will be limited to extraction of ocean wave features from imagery obtained via airborne synthetic aperture radar (SAR). The objective of this thesis is to provide a mathematical derivation of the filtering technique, and demonstrate its feasibility; the general results of this research, arising from application of the procedure to SAR data, have also been reported in [1].

Airborne and spaceborne SAR systems exhibit a strong potential for accurate assessment of ocean surface conditions. The relative ease with which data can be obtained, and the large spatial extent covered by the imaging radar, means that such measurements are logistically more feasible and statistically more representative, than observations made from the surface. A persistent problem with coherent imaging systems, however, is the introduction of speckle noise which severely degrades the image quality. The mathematics of a speckle process do not usually conform to the assumptions upon which most signal processing algorithms are based. This is because use of linear filtering operations presumes that the signal and noise

processes are additive and independent. In general however, the speckle and signal components of the image are known to interact in a multiplicative manner, and in some cases, the speckle amplitude may also be dependent upon the signal amplitude. Such attributes make speckle noise resistant to many well-known signal processing techniques; partially as a consequence of this, there has been little emphasis placed upon use of the linear filtering operators which will be employed in this thesis.

Furthermore, many filtering algorithms are based on an assumption, that the contaminating process has significant non-zero autocorrelation only at the zero lag of its autocorrelation function (ACF); this is the commonly-referenced white noise. However, in addition to its zero lag, speckle also has significant values at non-zero delays of its ACF; it therefore constitutes a less-commonly encountered process, usually referred to as coloured noise. In cases where the signal-to-noise ratio (SNR) is low, any estimate of the statistical parameters from the underlying image scene will be biased by the unwanted information from the speckle process. This introduces the need for an effective noise-suppression algorithm, which will minimize the capacity of speckle to interfere with the extraction of such information.

While it is well-established that in most cases, speckle contaminates in a multiplicative fashion, this thesis develops a linear mathematical method of suppression for a very special case; herein, the signal and speckle are assumed to be additive and independent, as well as individually WSS. There exists evidence to suggest that this assumption holds, with respect to SAR imagery of ocean wave scenes. The filtering technique which will be discussed, adapts to the desired wavefield component by utilizing information from the one-dimensional row and column autocorrelation functions of the image matrix, as well as the row and column cross-correlation functions (CCF's). This is the basic principle of design for a linear operator known as the Wiener filter, which will be discussed in some detail.

By an appropriate manipulation of the ACF and CCF, this operator forces a decorrelation of frequencies comprising the speckle, while the correlation of frequencies within the wavefield is maintained. In general, it is known that multi-channel Wiener filters, which simultaneously process data on several input channels, are more effective than their single-channel counterparts in achieving such decorrelations. During this project, a three-channel version of the multi-channel filter has been employed; however, in principle, a larger number of channels could also be effectively implemented in order to address the problem which is now being considered. In Chapter Two, a mathematical comparison will be provided in order to demonstrate the overall noise suppression superiority, which the three-channel filter has over the single-channel version. The three-channel filter accepts as input, three neighbouring rows of the image, each of which is separated by a specific distance from the others, and then produces a single row output. Based on the magnitude and phase relationships within and between these rows, the power in the output row is biased towards those frequencies which are coherent across the rows; uncorrelated frequencies are then suppressed during the filtering operation. By starting at the top of the image, the three-channel operation is incrementally shifted one row down and repeated. After the rows have been filtered, the image matrix is transposed to enable filtering of the columns via the same procedure.

Although SAR applications will be the ultimate goal, the general objective of this project is to demonstrate applicability of the three-channel Wiener filtering technique, to the problem of stochastic process recovery in the presence of coloured noise. Pursuant to such a scope, Chapter Two will focus on the mathematical derivation of the scalar Wiener filter, and investigate its performance for the special case of correlated noise. An extension will then be made by deriving a vector version of the filter, after having highlighted those attributes which give it superior noise suppression ability. Chapter Three will then present the results of simulated numerical case studies, designed to provide corroborating information in support of observations made within the context of Chapter Two. Building upon this, Chapter Four will demonstrate the

effectiveness of the filtering technique, by applying it to speckled images of two independent ocean scenes collected by airborne SAR. Subsequent to this, Chapter Five will assess the representativeness of the results obtained in Chapter Four, by investigating the spectral sensitivity of the filter output to changes in the input correlation parameters. In order to establish a general basis for these discussions, the remainder of the current Chapter will focus on the general history of speckle contamination in coherent imaging, and discuss some recent findings which have motivated the technique to be developed in Chapter Two.

1.2 Nature of the Speckle Phenomenon

1.2.1 The Process of Speckle Formation

Speckle contamination occurs when a coherent energy source is reflected from a surface, which is rough in comparison to the wavelength of the electromagnetic energy incident upon it; technical descriptions of this process may be found in [2] & [3]. Under this condition, the reflected wave consists of contributions from many independent scattering features [2], and each contribution will have a magnitude and phase which is determined by the geometry of its particular reflector. If the surface roughness is of a random nature, then it follows that the resulting magnitudes and phases are also random, for any given angle of incidence in relation to the radiating source of the energy. Moreover, for a change in the angle of incidence, the reflected wave will incorporate magnitude and phase components which are again random, but not necessarily independent of the return from the previous angle. Consequently, the returned signal consists of an envelope of coherent, dephased wavelets, which may incorporate relative phase delays of several wavelengths [2].

If a receiver has a resolution cell size such that several of the scattering elements fall within each cell, then the interaction of these dephased components will have a significant impact

upon the detected signal. Since the relative dephasing is random and dependent upon the geometry of the scatterer, then for some resolution cells, the superposition of the dephased wavelets will lead to highly constructive interference; integration of the return energy occurring within these cells will then produce a high intensity. At the opposite extreme, within other cells there will be highly-destructive interference, leading to a very low intensity value after integration. In the remainder of the cells, superpositions will be moderately destructive or constructive [2], producing varying levels of speckle intensity between the extremes. For a matrix of resolution cells, such as an image, the random superposition of wavelets ultimately results in a broad-band random pattern of intensities; this comprises the undesired speckle component, which needs to be suppressed by digital processing. The desired signal component which exists within the noisy image, is created when the backscattering surface also has variations that occur at a scale greater than the incident wavelength. In this situation, a component of the backscatter will also be phase-coherent with adjoining cells; consequently, it will incorporate a phase shift that systematically corresponds to those surface variations which occur at a scale equivalent to the resolution cell size. The image patterns which arise due to these variations, will contain discernible information regarding the surface being imaged; it is this information which needs to be enhanced through digital processing.

The goal of a signal processing operation then, is to separate the desired signal component from the undesired noise subspace of the image. However, a prerequisite to achieving success with any such operation in the intensity domain, is a mathematical model which adequately summarizes how the signal and noise components interact.

1.2.2 Modelling the Speckle and Signal Interaction

A commonly-referenced conceptualization of signal and speckle noise interaction, is the multiplicative noise model, used to describe speckle in both laser and radar applications. It is defined as:

$$x(i,j) = g(i,j) \cdot n(i,j) \quad (1.1)$$

where $n(i,j)$ is a random noise process which is independent of the signal $g(i,j)$. This is the relationship assumed in [2] & [3], and forms the basis of many attempts to suppress speckle by digital processing techniques. One of the earlier such works [4], used this model to develop an optimum restoration filter based on Wiener filtering theory; however, that filtering strategy does not correspond to the technique described in this thesis. Other approaches motivated by this model have involved taking a log transformation of the process in Eq. (1.1), thereby making it additive and allowing for the use of linear filtering operations [5]. By performing such a transform on multiple images of the same scene and then averaging them, the randomly-phased speckle can be somewhat suppressed, resulting in an improved SNR [6]. Still, this does not permit a detailed image recovery because the averaging process will produce some blurring; furthermore, multiple images of the same scene are not always available.

However, inadequacies have been reported regarding the multiplicative model, suggesting that it may only be regarded as an approximation. For instance, it has been shown in [7], that the model does not hold for situations in which the object being imaged contains detail finer than the resolution capability of the imaging system. The authors emphasize the practical significance of this observation, noting that most objects contain detail beyond the resolution of the imaging system being used; however, an alternative model was not suggested. Complementary to this, it has been proposed in [8], that image intensity might be expressed as:

$$i(x) = \left| \left[\sqrt{s(x)} e^{j\theta(x)} \right] \otimes h(x) \right|^2 \quad (1.2)$$

where $h(x)$ is the impulse response of the imaging system, and the symbol \otimes denotes convolution; $s(x)$ is signal intensity and $e^{j\theta(x)}$ is a random phase shift introduced by the speckle process. By working with this representation, a transformation has been developed which forces the speckle and signal to more closely approximate a multiplicative process, thereby permitting development of an optimum linear filter based on the minimum mean-square error criterion.

Many such investigations have been conducted in order to better understand the general problem of speckle in coherent imaging; this is because many inferential techniques used in physics, including laser imaging, are plagued by this phenomenon. However, with particular reference to suppression of speckle in SAR images, the multiplicative model and its related approximations have also been dominant. The purely multiplicative case was assumed in [9], when developing suppression methods based on local statistics from windowed sub-scenes of a SAR image, and later in [10], when reporting on local statistics and sigma filtering methods. Results in [11] suggest an extension to the multiplicative model, by assuming that image intensity may be represented as a convolution between the radar impulse response function, $h(i,j)$, and those terms which comprise Eq. (1.1). This model is expressed as:

$$x(i,j) = \left[g(i,j) \cdot n(i,j) \right] \otimes h(i,j) \quad (1.3)$$

Based on this, an optimum filter has been developed, which adapts to subregions of the image by using locally-estimated parameter values. More recent work, reported in [12], has assumed that an intensity image may be represented as a convolution which involves the terms of Eq. (1.1) and the radar impulse response, but with additive system thermal noise being introduced after the convolution. This relationship may be summarized as:

$$x(i,j) = \{ [g(i,j) \cdot n(i,j)] \otimes h(i,j) \} + v(i,j) \quad (1.4)$$

where $v(i,j)$ represents thermal noise, and $h(i,j)$ is the radar impulse response. From this model, a locally-adaptive two-dimensional block Kalman filter has been developed, which compensates for image degradations due to the multiple effects of speckle noise, additive receiver thermal noise, and linear space-invariant blur [12]. Other results, reported in [13], detail the first approach towards developing a model which takes into account the second-order statistics of speckle. This has permitted development of a family of locally-adaptive suppression filters, based on the assumption that the magnitude of speckle is correlated with the magnitude of the signal.

From these discussions, it is apparent that the speckle and signal interaction has been addressed by a range of modelling strategies. These various models have given rise to an array of filtering algorithms, some of which offer superior performance over others. A comparative study of several such speckle suppression algorithms has recently been reported in [14]. However, since these methods have not been based on the speckle and signal model which forms the basis of work in this project, further investigation of their relative attributes is not warranted.

1.2.3 Inadequacies of Existing Speckle Filters

The research presented in this report makes no claim against either the validity of the techniques discussed above, or the validity of assumptions under which they have been derived. However, the assumptions which facilitated their derivation do impose a common limitation, which is not present with the approach taken in this project. The disadvantage of these techniques is related to the usually non-stationary nature of a speckled SAR image, which implies that statistics computed within any given subscene will not be representative for the entire image. Because large-scale stationarity of the image scene cannot generally be assumed, the filtering operation must continuously adapt to the signal component within each image subscene of some predetermined size. To avoid glossing small-scale variability within the non-stationary signal, the

size of this scene is typically chosen to be very small, thereby ensuring that the process within the subscene is approximately stationary. This is important, because if statistics are derived on a large spatial scale and assumed to come from a stationary process, within a region which is actually non-stationary, then the filter is unable to account for the non-periodic variations in the signal and will not function optimally. Unfortunately, for an image in which the SNR is low, local filter parameters estimated from a small sample size will be severely perturbed by noise; hence, the accuracy of such estimates will not be strong. Consequently, for a non-stationary environment, effectiveness of the speckle-suppression technique is limited by the size of the subscene upon which it is required to operate. In general, the smaller the size, the less accurate this approach becomes, for any given SNR.

However, a significant advantage is gained when the digital process may be regarded as stationary on some large scale, such as the region defined by the borders of the image. Given these conditions, an adaptive filter may be derived based on estimates obtained regionally, from the entire area within the image. This follows from the stationarity assumption, which makes it possible to compute filter parameters via an averaging procedure which simultaneously incorporates all information from the imaged region. Due to the substantially larger sample size which will result, the filter will adapt to the signal component of the image with much greater accuracy. This implies that the regionally-adaptive method will yield superior results in comparison to the locally-adaptive approach, for any given SNR. Within this thesis, it has been assumed that one such example of regional stationarity would be an ocean wave scene as imaged by SAR. Yet, very little effort has been directed towards suppressing speckle in a process which is stationary over the entire scene. This is not surprising, because it corresponds to a small subset of the possible applications of SAR, whereas most filtering procedures developed thus far, have been motivated by a desire to solve the speckle problem for the general range of SAR applications.

1.2.4 Speckle and Signal Model for SAR Images of Ocean Scenes

In addition to regional stationarity, if it is also known that the speckle and signal processes are additive and mutually independent, then the suppression problem is further simplified. This is because linear prediction techniques may then be utilized in order to separate the background image from the speckle. Earlier work regarding SAR imaging of ocean wave scenes [15], continued to assume the multiplicative representation. However, recent findings in [16] do suggest that for an ocean wave scene imaged by SAR, the signal and speckle interact in an additive and independent manner. The theoretical development of this work commences with an assumption that the backscattered complex field received by the SAR, is made up of two statistically independent fields. One of these, the spiky field, is produced by breaking or near-breaking sea waves which produce discrete amplitude fluctuations. The other, which is the background field, arises due to system noise and/or the background of non-breaking waves of uniform scattering amplitude [16]. From this it can be shown that the total image field, A , is represented as the sum of two independent image complex fields:

$$A = A_b + A_s \quad (1.5)$$

where the subscripts b and s denote the background and spiky fields respectively. The image intensity is then defined as:

$$I = A \cdot A^* \quad (1.6)$$

where $*$ denotes complex conjugation. After taking expectations based on ensemble averages, the final image intensity is represented by:

$$\langle I \rangle = \langle I_b \rangle + \langle I_s \rangle \quad (1.7)$$

It is thought that the dominant contribution to the background field is due to additive receiver noise [16]. In most systems, this would be independent of the contribution coming from non-

breaking waves, and implies that the background field might actually be written as the sum of two intensities:

$$\langle I_b \rangle = \langle I_g \rangle + \langle I_r \rangle \quad (1.8)$$

where g represents the intensity due to the wavefield, and r denotes the contribution due to system noise.

Given these considerations, and by combining Eqs. (1.7) & (1.8), it follows that any pixel within a SAR image of an ocean wave scene will have an intensity, $x(i,j)$, which is represented as:

$$x(i,j) = \{ g(i,j) + r(i,j) \} + s(i,j) \quad (1.9)$$

Where again, $g(i,j)$ is the pixel intensity due to the wavefield component, $r(i,j)$ is the intensity due to system noise, and $s(i,j)$ is pixel intensity due to speckle. Clearly, it is possible to collect the speckle and system noise terms into a common noise term, defined as:

$$n(i,j) = r(i,j) + s(i,j) \quad (1.10)$$

This permits the image to be expressed as the following sum of signal and noise components:

$$x(i,j) = g(i,j) + n(i,j) \quad (1.11)$$

Where $n(i,j)$ is assumed to be coherent noise, due to the presence of the speckle component. Since both $r(i,j)$ and $s(i,j)$ are independent of $g(i,j)$, it follows that $n(i,j)$ will also be independent of $g(i,j)$. This establishes the attributes of additiveness and stochastic independence, for the interaction of signal and coherent noise within a SAR ocean wave scene.

1.3 Motivation for New Approach to Speckle Suppression

It has been demonstrated via Eq. (1.11), that for an ocean wave scene obtained by SAR, the wavefield and noise components of the image may be viewed as additive, independent

processes. Furthermore, the fact that the image contains an ocean wavefield, permits an assumption that the overall scene may be regarded as a process which is wide-sense stationary (WSS), at least within the region bounded by the image margins. Within this scene then, there are two independent WSS subcomponents, specifically, the speckle noise and the desired signal; this is also the assumption which has been taken in [16].

An additional consideration arises due to the correlated nature of speckle in WSS scenes, which has also been documented in [15] & [16]. Findings in [16] indicate that the ACF of the speckle decays very rapidly, within only a few lag steps of the zero lag; after this, it approaches some nominal level of power which is very low in comparison to the ACF for the signal component. The implication is that the noise component within any given pixel, has significant correlation with the noise component of other pixels only in its immediate vicinity. This is also supported by results found in [15], which showed that the second-order statistics of a SAR speckle process could be represented as a nearest-neighbour correlation. Given these facts, it is possible to conclude that the spatial extent of correlation within the noise component of the image, is much less than the extent of correlation within the wavefield component.

The above facts prompt recognition that speckle suppression is possible via an alternate technique, which differs in assumption from methods documented thus far. Consequently, it will now be asserted that a new method is feasible, provided that certain mathematical prerequisites are satisfied by the process which has been imaged. Pursuant to this, three conditions necessary for implementation of the technique may be stated as follows:

- (1) The noise and wavefield components of the image must be additive, and mutually stochastically independent.
- (2) The process occurring within the image must be WSS, at least to the regional extent defined by the borders of the image. This implies that both the speckle and signal subcomponents must each be WSS.

- (3) The spatial extent of correlation of the noise process, must be far less than the extent of correlation of the desired signal component.

Given any situation for which such conditions hold, it is the working hypothesis of this thesis, that a linear filter which adapts regionally to the entire image will be capable of effectively suppressing correlated noise. The use of a linear filter is motivated in conjunction with Condition (1), and its regionally-adaptive nature follows from Condition (2). An important ramification due to Condition (3), is that if the spatial dimension of significant noise correlation can be determined, then gapped forward linear prediction may be applied to the image as a means of suppressing the correlated noise. According to linear prediction theory [17], it is possible to derive a linear function which operates on the past values of a coherent data sequence, in order to predict its future values. By this technique, a sequence of data points, $x(1), x(2), \dots, x(n)$, say, may be used to predict point $x(n+\alpha)$, which lies α steps ahead within the set. If the prediction gap, α , between $x(n)$ and $x(n+\alpha)$, is greater than the spatial extent of noise correlation, then only the correlated signal component can be predicted; provided also, that the extent of correlation of the signal is greater than or equal to α . As a consequence of this, the predicted sequence is smoothed by the operator, which suppresses variations occurring at any interval smaller than α . Therefore, choosing α to be larger than the dimension of speckle correlation, implies that the noise will be suppressed when the image is operated upon. Hence, Condition (3) provides motivation for deriving the desired filter as an α -step forward linear predictor. Following from these conclusions, the next Chapter will provide a mathematical formulation of such an operator, and examine how its performance is determined by the correlation characteristics of the wavefield and noise processes which comprise the image.

CHAPTER TWO

ANALYTICAL FORMULATION OF TECHNIQUE FOR SUPPRESSION OF BROAD-BAND COHERENT NOISE

2.1 Introduction

The problem of recovering information from a noisy image has typically been approached by the use of two-dimensional filtering operators, as discussed in [6], [18], [19] & [20]. However, the applicability of one-dimensional techniques to two-dimensional image processing has also been demonstrated in the literature [21], and provides some impetus for the technique to be developed herein. Therefore, this Chapter will detail a method by which a digital image satisfying the constraints of Section 1.3, can be processed by two three-channel linear operators. One operator will adapt to the row dimension of the image, while the other adapts to the column dimension. The row filter triplet then operates to suppress noise within the rows, after which, the column operator triplet is applied in order to reduce noise in the columns. Initially, it will be seen that single-channel filters operating sequentially in this manner, will achieve noticeable and quantifiable noise reduction. However, it will subsequently be demonstrated that vector stochastic process theory can be applied in order to derive three-channel versions of such filters. These vector operators will exhibit superior noise-suppression capabilities, when compared to the single-channel versions.

2.2 Formal Statement of Problem

The problem of obtaining information concerning a two-dimensional stochastic process, in the presence of broad-band coherent noise, will now be formally defined. By way of

introduction, consider an image which consists of a two-dimensional process, $x(i,j)$, defined as:

$$x(i,j) = g(i,j) + n(i,j) \quad (2.1)$$

Such a process is comprised of two components; it will be generally assumed that $g(i,j)$ is a zero-mean, wide-sense stationary, stochastic bandpass signal process, which is independent of the zero-mean, wide-sense stationary, broad-band noise process, represented by $n(i,j)$. The bandpass process, $g(i,j)$, is the *desired signal* about which information is sought. By definition, a stochastic process is bandpass if its power spectrum contains a cluster of frequency components, in a frequency band of some width w , which have significantly higher power in comparison to the nominally non-zero power levels existing at all other points of the spectrum [22]. Such a cluster of frequencies will be referred to as the effective bandwidth of the process. This definition also assumes that the frequency $f=\theta$ is not a part of the cluster; however, note that the power spectrum is not required to be zero at this frequency. In a less-general case, $g(i,j)$ may alternatively be a narrow-band process, having a spectrum which is zero at most frequency points, except for a non-zero cluster of some bandwidth w . With respect to the noise process, $n(i,j)$, its broad-band definition implies that it incorporates components of significantly non-zero power, from *all* frequencies within the spectrum.

The form of Eq. (2.1) reveals that any attempt to compute statistics regarding $g(i,j)$, must inevitably include information from the noise process, thereby biasing estimates of the parameters which are of interest. In general then, if $O[x(i,j)]$ is some linear operator which computes a statistic from the image, the expectation of this statistic will ultimately be expressed as a sum of individual expectations, derived from each of the signal and noise processes:

$$\mathcal{E}\{O[x(i,j)]\} = \mathcal{E}\{O[g(i,j)]\} + \mathcal{E}\{O[n(i,j)]\} \quad (2.2)$$

It is now clear that the desired statistics pertaining to $g(i,j)$ cannot be obtained directly from the unprocessed image.

One such example of the linear operator discussed in Eq. (2.2) is the Discrete Fourier Transform (DFT), and its computationally-efficient counterpart, the Fast Fourier Transform (FFT). An expectation operation involving the DFT produces the well-known periodogram [23]. A periodogram DFT is commonly used in image analysis, and it is often the case that the image data have been gathered specifically in order to extract spectral information via this operation. In fact, the principal application of the filtering technique developed in this thesis, will be image pre-processing in order that more accurate DFT's may be obtained under conditions of low SNR. In order to appreciate the need for this preprocessing, begin by considering that the two-dimensional DFT of $x(i,j)$ is expressed as:

$$\begin{aligned}
 X(f_C, f_R) &= \sum_{n_C=0}^{N_C-1} \sum_{n_R=0}^{N_R-1} x(n_C, n_R) e^{-j f_C n_C} e^{-j f_R n_R} \\
 &= \sum_{n_C=0}^{N_C-1} \sum_{n_R=0}^{N_R-1} g(n_C, n_R) e^{-j f_C n_C} e^{-j f_R n_R} + \sum_{n_C=0}^{N_C-1} \sum_{n_R=0}^{N_R-1} n(n_C, n_R) e^{-j f_C n_C} e^{-j f_R n_R} \\
 &\left\{ f_C = \frac{2\pi k_C}{N_C}, f_R = \frac{2\pi k_R}{N_R} \mid k_C = 0, 1, \dots, N_C-1, k_R = 0, 1, \dots, N_R-1 \right\}
 \end{aligned} \tag{2.3}$$

where N_C and N_R might represent the total number of pixels within each column and each row respectively, but which may actually assume larger values in order to improve angular resolution of f_C and f_R . The column and row frequencies, f_C and f_R , are discrete frequency points which are uniquely defined within the normalized range of $0 \leq (f_C, f_R) < 2\pi$ only. From Eq. (2.3), it is easy to see that a periodogram estimate of the spectrum of $g(i,j)$ will also be biased by the noise component of the image. If the noise has only significant correlation at the zero lag of its ACF, then a bias will be added to the power of all digital frequencies in the spectrum of $g(i,j)$. Although this is theoretically a constant bias, when the FFT is used, several frequencies of the noise process may coincide within the same frequency bin. This combined power produces spurious peaks in the spectrum, which may be so large as to make them indistinguishable from peaks due to the

desired signal. For very low SNR, extensive periodogram averaging may then be required in order to identify the signal portion of the spectrum.

Additional complications are introduced if the noise also has significant correlation at non-zero lags of its ACF. In this case, the noise will have a tapered spectrum, with significantly greater power found in frequencies near DC when compared to frequencies near Nyquist. When this is added to the spectrum resulting from the signal component of the image, then the overall shape of the power spectrum of the image is distorted. For this situation, periodogram averaging will not be capable of restoring a shape which corresponds to the spectrum of the desired signal, because the bias imposed by correlated noise will vary as a function of frequency. Hence, for spectrum estimation in the presence of broad-band correlated noise, it is particularly important that the noise power be minimized prior to performing a Fourier transform. This will ensure that the shape of the resulting power spectrum more accurately reflects the actual spectrum of the desired signal, $g(i,j)$.

2.3 An Adaptive Filtering Solution to the Signal Recovery Problem

A block data-adaptive filter offers considerable promise of effective noise suppression, when operated in a gapped prediction mode subject to the constraints outlined in Section 1.3. This type of filter adapts to the signal component of an image process, after statistically-representative estimates of the correlation functions have been obtained. The block data approach to adaptive filtering offers superior results in comparison to other techniques, because it incorporates parameter estimates based upon all data contained within the image. This differs from locally adaptive methods, such as gradient estimators, which continuously update an ACF by utilizing values in the recent past of a time series, in order to predict a future value. A filter derived from block-data computations, contains information regarding both the entire past and entire future of

a finite time series upon which it operates. This provides superior ability for the anticipation of a future value, within a stationary process.

By selective manipulation of appropriate components within the correlation functions of a stochastic process, the passband of the block data version of an adaptive filter may be adjusted, thereby achieving conformance to the effective bandwidth of a signal process. When this operator is then applied to the image, the noise component which lies outside the passband is severely attenuated, resulting in an image scene which has fewer detectable noise components; this filtered image is an estimate of the desired signal. In order to fully understand the means by which this may be achieved, it will first be necessary to investigate the correlation characteristics of the signal and noise components of the image.

2.4 Correlation Characteristics of Imaged Stationary Stochastic Processes

2.4.1 General Derivation of Two-Dimensional and One-Dimensional Correlation Functions

It is well-known that the correlation functions of WSS stochastic processes contain information pertaining to the frequency content of such signals [17] & [23]. As a prelude to developing one-dimensional filtering operations for a two-dimensional process, it will first be shown that valid one-dimensional ACF's and CCF's may be derived from the two-dimensional ACF of that process. It will then become apparent that a two-dimensional WSS process must consist of two complementary one-dimensional processes, comprising the rows and the columns of the image in which it has been captured. To begin, consider that the ACF of the process described in Eq. (2.1) may be obtained as:

$$\mathcal{E}\{x(i+\tau_c, j+\tau_r) x(i, j)\} = \mathcal{E}\{[g(i+\tau_c, j+\tau_r) + n(i+\tau_c, j+\tau_r)] [g(i, j)+n(i, j)]\} \quad (2.4)$$

where i and j represent the row and column indices respectively, within the image matrix. The symbols τ_c and τ_r , denote the lagged correlation distances along the column direction and along the row direction respectively. Since the cross-covariance information cancels, via the

independence of the two zero-mean processes, the final result is:

$$R_{xx}(\tau_C, \tau_R) = R_{gg}(\tau_C, \tau_R) + R_{nn}(\tau_C, \tau_R) \quad (2.5)$$

For the theoretical developments which follow, it will be assumed that $R_{xx}(\tau_C, \tau_R)$ has been derived via a regional estimate based on the entire image scene. By use of Eq. (2.5), it is possible to separate correlation information pertaining to the rows of the image, from that which pertains to the columns. In order to see this, let the lagged distance between rows be represented by τ_C , and the lagged distance between columns correspond to the value of τ_R . Then, setting $\tau_C = \theta$ in $R_{xx}(\tau_C, \tau_R)$ must yield the regional average of the one-dimensional ACF, $r_{xx}(\tau_R | \theta)$, for the one-dimensional signal-plus-noise process existing in the rows. Similarly, setting $\tau_C = \beta$ produces the regional CCF, $r_{yy}(\tau_R | \beta)$, existing between any two rows, x and y , which are separated by a distance of β . In summary, the one-dimensional regional ACF and CCF's of the image row process are derived as:

$$\begin{aligned} r_{xy}(\tau_R | 0) &= R_{xx}(0, \tau_R) = R_{gg}(0, \tau_R) + R_{nn}(0, \tau_R) \\ r_{xy}(\tau_R | \beta) &= R_{xx}(\beta, \tau_R) = R_{gg}(\beta, \tau_R) + R_{nn}(\beta, \tau_R) \end{aligned} \quad (2.6)$$

Furthermore, by the assumption of stationarity, the following very important axiom also holds for the CCF:

$$r_{yx}(-\tau_R | -\beta) = r_{xy}(\tau_R | \beta) \quad (2.7)$$

It is easily seen that by performing the same manipulations on τ_R , it is also possible to derive the one-dimensional ACF and CCF's for the process existing in the columns.

2.4.2 Analytical Form of the Two-Dimensional ACF and its One-Dimensional Components

In developing an analytical form for the two-dimensional ACF, it will be assumed that the signal stochastic process, $g(i, j)$, has an ACF which can be approximated as the sum of n exponentially-damped, two-dimensional sinusoids. This model has been chosen because it offers

the greatest flexibility in representing a bandpass process. Often, the spectrum of such a process can include more than one cluster of frequencies, each with power levels which are significantly greater than the overall nominally non-zero levels; the use of n terms facilitates proper representation of this case. As well, this representation permits modelling of a narrow-band spectrum, merely by setting the exponential damping factors to zero. Moreover, in Chapter Four, it will be seen that this model adequately accommodates the form of two-dimensional ACF's which will be derived from SAR images of ocean scenes. Therefore, building upon discussions found in [24], the two-dimensional ACF of $g(i,j)$ may be represented as:

$$R_{gk}(\tau_C, \tau_R) = \sum_{k=1}^n a_k e^{-d_{kC}|\tau_C| - d_{kR}|\tau_R|} \cos(\omega_{kC}\tau_C + \omega_{kR}\tau_R) \quad (2.8)$$

$$-(N_C-1) \leq \tau_C \leq (N_C-1), \quad -(N_R-1) \leq \tau_R \leq (N_R-1)$$

Here the index k denotes the k 'th element of some set of size n ; N_C and N_R represent the total number of pixels in each column and each row of the image, respectively. The digital phasor increment pairs, ω_{kC} and ω_{kR} , are defined to be:

$$\omega_{kC} = \frac{2\pi\lambda_{kC}}{L_C}, \quad \omega_{kR} = \frac{2\pi\lambda_{kR}}{L_R}$$

where $(L_C, L_R) \in \mathbb{N}$, $L_C < N_C$, $L_R < N_R$

$$\text{and } (\lambda_{kC}, \lambda_{kR}) \in \{(\lambda_{1C}, \lambda_{1R}), \dots, (\lambda_{nC}, \lambda_{nR})\} \subseteq \{(\lambda_{kC}, \lambda_{kR}) \in \mathbb{I}^2 \mid 0 \leq \lambda_{kC} < L_C, 0 \leq \lambda_{kR} < L_R\} \quad (2.9)$$

It will be assumed that $L_C \ll N_C$ and $L_R \ll N_R$; since N_C and N_R are the dimensions of the image, this implies that the two-dimensional ACF will incorporate many cycles of its lowest-frequency component. Furthermore, the subset indicated in Eq. (2.9) is defined to be a not-necessarily-contiguous subset of \mathbb{I}^2 .

In Eq. (2.8), the term a_k represents the amplitude of the k 'th two-dimensional sinusoid in the ACF. For each such sinusoid, the terms d_{kC} and d_{kR} represent the damping factors along the

column dimension and the row dimension respectively. For any given k , these terms may or may not be equal; this accommodates the possibility that an imaging system gathers information for the row dimension, in a manner which differs from that by which it obtains column information. Since it is known that an imaged scene will be affected by the point spread function of the imaging system, it follows that this influence must ultimately be reflected in the autocorrelation data which are extracted from that scene. By convention similar to above, it will be assumed that each amplitude factor and each damping factor pair, represent the k 'th elements of their respective not-necessarily-contiguous subsets of size n , defined as:

$$a_k \in \{ a_1, \dots, a_n \} \subset \{ a \in \mathbf{R} \mid 0 < a < \infty \} \quad (2.10)$$

$$(d_{kC}, d_{kR}) \in \{ (d_{1C}, d_{1R}), \dots, (d_{nC}, d_{nR}) \} \subset \{ (d_C, d_R) \in \mathbf{R}^2 \mid 0 \leq d_C < \infty, 0 \leq d_R < \infty \}$$

Therefore, Eqs. (2.8), (2.9), and (2.10) describe the general approximation of the ACF for a two-dimensional bandpass stochastic process contained in a digital image. In the special case where the damping factors are identically zero and the process is narrow-band, the ACF in Eq. (2.8) reduces to a sum of n periodic sinusoids, with each k 'th component having an amplitude of a_k .

With respect to the noise component of $x(i,j)$, shown in Eq. (2.1), it will generally be assumed that $n(i,j)$ is a correlated process, having a two-dimensional ACF which is approximated as:

$$R_{nn}(\tau_C, \tau_R) = \sum_{u=-c}^c \sum_{v=-c}^c \Delta(u,v) \delta(\tau_C - u, \tau_R - v) \quad (2.11)$$

Here, $\Delta(u,v)$ represents the amplitude of a two-dimensional delta function, $\delta(\tau_C, \tau_R)$, and the constant c is a non-negative integer which defines the extent of correlation of the noise process. While it may actually be the case that the extent of noise correlation in one dimension of the image is greater than in the other, the magnitude of c should represent the maximum of these two values. It will eventually become apparent that the derivation of row and column filters using

different minimum prediction gaps, as permitted by two different values of c , would produce generally undesirable results. From Eq. (2.11), it is clear that $R_{xx}(\tau_c, \tau_R)$ is equal to zero for either $|\tau_c| > c$ or $|\tau_R| > c$; a special form of Eq. (2.11) occurs when $c=0$, in which case the contaminating process consists of white noise only.

From Eq. (2.6), and by setting $\tau_c=0$ in Eqs. (2.8) and (2.11), the one-dimensional regional ACF for the row component of the image process now becomes:

$$r_{xy}(\tau_R | 0) = \sum_{k=1}^n a_k e^{-d_{ik}|\tau_R|} \cos(\omega_{kR} \tau_R) + \sum_{\nu=-c}^c \Delta(0, \nu) \delta(0, \tau_R - \nu) \quad (2.12)$$

$$= r_{xy}(\tau_R | 0) + r_{xy}(\tau_R | 0), \quad \text{where } -(N_R-1) \leq \tau_R \leq (N_R-1)$$

Careful inspection of Eq. (2.12) will lead to four important conclusions, which will have significant implications for subsequent discussions:

- (1) $r_{xy}(\tau_R | 0)$ contains no information regarding the phase of frequencies relative to one another within a given row.
- (2) For values of $|\tau_R| > c$, the row ACF contains only information relating to the row component of signal process $g(i, j)$, that is, $r_{xy}(\tau_R | 0) = r_{xy}(\tau_R | 0)$. This is due to the fact that any contribution to the ACF from the row component of $n(i, j)$, is zero for these values of τ_R .
- (3) If the damping factors, d_{iR} , are identically zero, then for $|\tau_R| > c$, there exists some integer, η , such that $r_{xy}(\tau_R | 0)$ is periodic; that is, $r_{xy}(|\tau_R| | 0) = r_{xy}(|\tau_R| + |\eta| | 0)$ and $r_{xy}(-|\tau_R| | 0) = r_{xy}(-|\tau_R| - |\eta| | 0)$.
- (4) If the damping factors are not identically zero, then the ACF will decay as $|\tau_R|$ becomes large, and the periodicity property will no longer hold. In particular, if $d_{iR} > d_{iR} > \dots > d_{iR}$, then for $|\tau_R| = |q| > c$, where q is close to c say, the cosine component associated with d_{iR} will experience moderate attenuation in comparison to that of the

cosine component associated with d_{LR} . However, for very large q , the component governed by d_{LR} will exhibit severe attenuation when compared to that of the component governed by d_{LC} .

Also, by Eq. (2.6), the regional CCF of the row process is derived by setting $\tau_c = \beta$ in $R_{xx}(\tau_c, \tau_R)$, where β is the desired distance between any two rows of the image. By inspection of Eqs. (2.8) and (2.11), it is seen that this will yield:

$$r_{xy}(\tau_R | \beta) = \left\{ \begin{array}{l} \sum_{k=1}^n a_k e^{-d_{LC}|\beta| - d_{LR}|\tau_R|} \cos(\omega_{LC}\beta + \omega_{LR}\tau_R) \\ + \sum_{u=c}^c \sum_{v=c}^c \Delta(u, v) \delta(\beta - u, \tau_R - v) \end{array} \right\} \quad (2.13)$$

$$= r_{Rxy}(\tau_R | \beta) + r_{nxy}(\tau_R | \beta), \quad \text{where } -(N_R-1) \leq \tau_R \leq (N_R-1)$$

Study of Eq. (2.13) will also lead to four significant conclusions:

- (1) $r_{Rxy}(\tau_R | \beta)$ contains a constant phase term, $\omega_{LC}\beta$, which is introduced by the column dimension of imaged wavefield $g(i, j)$. This indicates that the CCF retains information regarding the phase relationships which exist between the row components of the desired signal process. It is, in fact, this very phase relationship which preserves the one-dimensional process existing in the columns.
- (2) The noise component, $r_{nxy}(\tau_R | \beta)$, can be removed, either by choosing $\beta > c$ prior to deriving the CCF or by taking $|\tau_R| > c$ afterwards.
- (3) Similar to the ACF, the CCF will also exhibit periodicity for $|\tau_R| > c$ if the damping factors are all zero. For non-zero damping factors, the CCF behaves in the same manner as does the ACF for observation (4) above.
- (4) In addition to the damping which occurs as a function of τ_R , the CCF also contains a constant damping term, $e^{-d_{LC}|\beta|}$, which is introduced by the column component of the

two-dimensional ACF. Therefore, if at least one of the damping factors is non-zero, then the power and shape of the CCF will be altered by changes which occur in either τ_R or β .

Generally-speaking, it has been convention to treat the ACF and CCF as separate entities, despite the fact that they are mathematically very similar. Specifically, by inspection of Eqs. (2.12) and (2.13), it is seen that the ACF may be regarded as a special case of the CCF, for which the parameter β is zero. Given this, most subsequent mathematical discussions involving correlation information will take a unified approach, by working only with the analytical form of the CCF. The corresponding result for the ACF may then be instantly realized, merely by setting $\beta = 0$. Furthermore, throughout this report, correlation functions for which *all* damping factors are identically zero, will be referred to as Case I correlation data. Functions which exhibit *only* positive damping factors, will be referred to as Case II; combinations of zero and positive damping factors will define Case III correlation data.

2.4.3 Spectral Characteristics Within the Signal Component of the CCF

The spectral content of the signal component of the CCF, will eventually be shown to have a significant impact upon the filtering technique being developed. Consequently, a detailed examination of the frequency-domain representation for this portion of the CCF is now warranted.

To begin, consider a subset of size N_R , comprised of contiguous coefficients taken from the right-hand side of $r_{g^{(y)}; \tau_R}(\beta)$, for which the correlation lag is non-negative. This subset may be represented as:

$$r_{g^{(y)}; \tau \geq 0} = \{ r_{g^{(y)}; \tau_R}(\beta) \mid 0 \leq \tau_R \leq N_R - 1 \} = \{ r_{g^{(y)}}(0 \mid \beta), r_{g^{(y)}}(1 \mid \beta), \dots, r_{g^{(y)}}(N_R - 1 \mid \beta) \} \quad (2.14)$$

where the elements of $r_{g^{(y)}; \tau \geq 0}$ are ordered according to increasing values of τ_R . By analysis of

$r_{xy}(\tau)$, it is desired to obtain information regarding the spectral content within the row component of its generating stochastic process, $g(i, j)$. This analysis will be performed upon some contiguous, ordered subset of chosen size $\xi \ll N_R$, found within $r_{xy}(\tau)$ and defined to be:

$$r_{gxy}(\tau; \alpha) = \{ r_{gxy}(\tau_R | \beta) \mid \alpha \leq \tau_R \leq \alpha + \xi - 1 \} = \{ r_{gxy}(\alpha | \beta), \dots, r_{gxy}(\alpha + \xi - 1 | \beta) \} \quad (2.15)$$

where α is a non-negative integer, $0 \leq \alpha \leq N_R - \xi$. By changing the value of α , given fixed ξ , it is possible to window several equal-length subsets of the CCF, in order that an independent spectral analysis may be performed upon each one. The frequency-domain mapping of $r_{gxy}(\tau)$, represented as $G_{xy}(f | \alpha, \beta)$, will be achieved via the one-dimensional Discrete Fourier Transform (DFT), formally defined as:

$$G_{xy}(f | \alpha, \beta) = \sum_{k=0}^{\xi-1} r_{gxy}(k + \alpha | \beta) e^{ifk} \quad (2.16)$$

$$\text{for, } f \in \left\{ \frac{2\pi\zeta}{\xi} \mid \zeta = 0, \dots, \xi - 1 \right\}$$

$$\text{and, } 0 \leq \alpha \leq N_R - \xi$$

It will be assumed that ξ can be chosen such that $(\xi/L_R) \in \mathbb{N}$; that is, L_R from Eq. (2.9) divides ξ with zero remainder. The reason for this assumption will become apparent from the discussion in Appendix I. Furthermore, by use of the well-known identity:

$$\cos(\theta) = \frac{e^{-j\theta} + e^{j\theta}}{2} \quad (2.17)$$

the spectral analysis will be performed only for the negative complex exponential component of each cosine term occurring in $r_{xy}(\tau_R | \beta)$. Given these considerations, and for any chosen values of α and β occurring in the signal component of Eq. (2.13), the frequency-domain behaviour of $r_{xy}(\tau_R | \beta)$ may be categorized by three possible cases, based upon values taken by the damping coefficients, d_{kC} and d_{kN} , $k=i, \dots, n$.

2.4.3.1 Case I: Damping Coefficients are Identically Zero

Consider first, a case for which the damping coefficients are identically zero, such that $d_{kR}=d_{kI}=0$, for $k=1,2,\dots,n$ in Eq. (2.13). In Appendix I, it has been shown that upon evaluation of the DFT in Eq. (2.16), $G_{xy}(f|\alpha,\beta)$ may be expressed as:

$$G_{xy}(f|\alpha,\beta) = \sum_{k=1}^n \xi \frac{a_k}{2} e^{-j(\omega_{kI}b + \omega_{kR}a)} \delta(f - \omega_{kR}) \quad (2.18)$$

From this it is clear that the spectrum of $r_{xy}(\tau_R|\beta)$ contains complex phase terms, introduced by the α and β parameters. Assuming that $\omega_{kR} \neq \omega_{hR}$, for $a \neq b$, it is seen that for any k 'th frequency, ω_{kR} say, only the k 'th component of the summation on the RHS of Eq. (2.18) is non-zero for fixed f . This condition has been imposed by the presence of the delta function, and shows that for any given f , only one of the n terms can be non-zero. This implies that for any two arbitrary disjoint frequency pairs, $(\omega_{kR}, \omega_{kI})$ and $(\omega_{hR}, \omega_{hI})$ say, the a 'th complex vector never interacts with the b 'th complex vector during the summation operation which defines $G_{xy}(f|\alpha,\beta)$. This is because when the frequency response due to the first pair is non-zero, the frequency response due to the second must be zero, and vice-versa. For any f therefore, it follows that the resultant of the vector summation in Eq. (2.18) is still the k 'th non-zero complex vector. Hence, the *magnitude* of this resultant is constant for all α , and the only change which the resultant will experience due to varying α , is an angular advance of its phasor.

To extend this argument further, suppose now that for $l < p \leq n$, there exists p terms in Eq. (2.18), all of which have the *same* value for ω_{kR} , but each of which has a *distinctive* phase term, ω_{kI} . In this case there must be p terms involved in the summation of Eq. (2.18), however, for each term, the initial phase value, ω_{kI} , is independent of α . Careful thought will reveal, that these p complex vectors will maintain their same magnitudes and *relative* positions in the z -plane for all α ; again, the magnitude of the complex vector resulting from the summation will be

independent of α . The ultimate conclusion, is that magnitude information for each value of f in Eq. (2.18) is independent of α . Consequently, the spectral power representation of $r_{xy}(\tau_R|\beta)$ will be constant for all values assumed by this parameter under Case I. For the same reasons just given, it is also easy to verify that variations in the value of β will have no effect upon the shape of the spectrum.

A special case of Eq. (2.18) may be derived by setting $\alpha=\beta=0$, which produces the autospectrum for the row component of $g(i,j)$. In this situation, it is easy to see that $G_{yy}(f|0,0)$ is defined as:

$$G_{yy}(f|0,0) = \sum_{k=1}^n \xi \frac{a_k}{2} \delta(f - \omega_{kR}) \quad (2.19)$$

Therefore, it has now been shown that the one-sided autospectrum of the row component of $g(i,j)$ consists of lines only, when the damping coefficients are identically zero.

2.4.3.2 Case II: Damping Coefficients are all Non-Zero

Given the case in which all damping factors are non-zero, derivations presented in Appendix I reveal that the DFT of $r_{xy}(\tau_R|\beta)$ may be expressed as:

$$G_{xy}(f|\alpha, \beta) = \sum_{k=1}^n \frac{a_k}{2} e^{-\left(d_{kR}|\beta\right) \cdot d_{kR} \left[\frac{2\pi + \xi - 1}{2}\right]} e^{-j\left(\omega_{kR}\beta \cdot \left[\frac{2\omega_{kR} \cdot f - \omega_{kR}}{2}\right]\right)} \frac{\sinh\left(d_{kR} \xi / 2\right)}{\sinh\left[\left(d_{kR} + j\omega_{kR} - jf\right) / 2\right]} \quad (2.20)$$

Inspection of this equation reveals a situation which is very different from that which was represented by Eq. (2.18). An assessment commences by noting that the \sinh function in the numerator can be zero only if $d_{kR} = 0$ or $\xi = 0$, both of which are impossibilities under the assumptions defining Case II. This means that for every f , $G_{xy}(f|\alpha, \beta)$ is the complex resultant of n complex terms, each of non-zero magnitude. Since, in general, $\omega_{kR} \neq \omega_{jR}$ for $k \neq j$, the n complex vectors in Eq. (2.20) will not maintain constant relative distances in the z -plane as α

changes. This implies that for any fixed f , the complex resultant of the summation will vary with changes in α . Hence, the magnitude of the resultant will in part be determined by the degree of constructive or destructive interference, which occurs during addition of the n complex terms. This suggests that for each f , variations in the magnitude of $G_{xy}(f|\alpha,\beta)$ would be cyclical if α were to increase without bound. In addition to this, the relative contributions from the exponential damping factors will also change with α , more rapidly for some of the n components than for others. When these considerations are taken into account, they clearly demonstrate that the spectral representation of the bandpass process is directly dependent upon α , and the DFT of $r_{x\alpha}(\tau_k|\beta)$ cannot be uniquely defined. It is also easy to see, for fixed α , that varying the value of β will have an equivalent effect. Therefore, magnitude information pertaining to any f in the spectrum is directly affected by the values which these parameters assume.

An examination of the special case in which $\alpha=\beta=0$, reveals that the autospectrum of the bandpass process existing in the rows of the image is represented as:

$$G_{xy}(f|0,0) = \sum_{k=1}^n \frac{a_k}{2} e^{-\left(d_{kR} \left[\frac{\xi-1}{2} \right] \right)} e^{-j \left(\left[\frac{f - \omega_{kR}}{2} \right] \right)} \frac{\sinh \{ d_{kR} \xi / 2 \}}{\sinh \{ (d_{kR} + j \omega_{kR} - j f) / 2 \}} \quad (2.21)$$

Therefore, it is easily seen that the autospectrum is also non-zero for all f . It now follows that if the exponential damping factors are all non-zero, then the autospectrum of the row component of $g(i,j)$ can never be represented as a line spectrum.

Further to these observations, consider also the cross-row spectral power coherence function, which indicates the relative power of the bandpass frequency components between any two rows, x and y . This is usually computed with $\alpha=0$ in the one-sided spectrum, and is defined as:

$$\gamma_{xy}^2(f|0, \beta) = \frac{|G_{xy}(f|0, \beta)|^2}{|G_{xx}(f|0, 0)| |G_{yy}(f|0, 0)|} \quad (2.22)$$

Based on the above discussion, since the autospectra and cross-spectra change as a function of β , it also follows that the cross-row coherence function must similarly change with alterations in β . In Chapter Five, evidence of β -induced variations will be presented, in order to verify the presence of Case II data within SAR imagery of two ocean wave scenes.

2.4.3.3 Case III: Damping Coefficients are Combination of Zero and Non-Zero Terms

Lastly, consider the situation in which only some of the n terms in Eq. (2.20) have non-zero damping factors; this is known as a mixed spectrum [25]. In particular, let the first $a < n$ of the terms have identically zero damping factors, and let $G_v(f|\alpha, \beta)$, represent the v 'th term in the summation of Eq. (2.18). Similarly, let the remaining $n-a=b$ of the terms have non-zero damping factors, and let $G_u(f|\alpha, \beta)_u$ represent the u 'th component in the summation of Eq. (2.20). Given these conditions, it follows that the sum of these $n = a + b$ terms is represented as:

$$G_{xy}(f|\alpha, \beta) = \sum_{v=1}^a G_{xy}(f|\alpha, \beta)_v + \sum_{u=1}^b G_{xy}(f|\alpha, \beta)_u \quad (2.23)$$

The implication of this relationship is that if at least one of the damping factors is non-zero, then the influence of $G_u(f|\alpha, \beta)_u$, described by Case II, will mean that a unique spectral estimate cannot be found in $G_{xy}(f|\alpha, \beta)$. Additionally, by the findings obtained under Case II, it also follows that $G_v(f|\alpha, \beta)$ in Case III can never consist of lines only, if at least one damping factor is non-zero.

The facts highlighted by the above three cases, provide information which will be crucial in assessing the capability of the scalar and vector Wiener filters. While Case III correlation has been briefly discussed, this has been conducted only in the interest of completeness. Subsequent investigations will deal exclusively with Case I and Case II data; from these, ramifications for

Case III data will be readily apparent. With this information now established, it is possible to proceed with development of the Wiener filter operators.

2.5 Block-Adaptive Wiener Filter for Scalar Stochastic Processes

2.5.1 Overview

A one-dimensional scalar stochastic process, $x_i = \{x_i(j) | j=1, \dots, N_R\}$, consists of a set of data points, $x_i(j)$, which denote the magnitude of observations made on the process which exists in row i , at discrete points along the column index j . When applying scalar process theory to the digital image of a two-dimensional wavefield, it is assumed that each image row of length N_R , represents a set of point-wise observations. Each such set constitutes the i 'th row realization of a parent stochastic process from which all rows have been generated. This is consistent with the fact that $R_{xx}(l, \tau_R) \equiv r_{xx}(\tau_R | \beta=0)$ represents the expectation associated with the zeroth column lag in the two-dimensional ACF, which has been obtained over all rows of the image. Therefore, the parent process which is represented by $r_{xx}(\tau_R | 0)$ contains information which is common to all rows, due to an averaging of the correlation functions; in fact, this parent process is determined via the *expectation* of ACF's from individual row process realizations. Note also, that it is not possible to characterize any given row realization as ergodic, because, while the two dimensional process is assumed to be of zero mean, it is highly conceivable that the individual row processes may have unequal, non-zero means. This would occur with a situation in which a DC offset in the rows is modulated by a wavefield which exists only in the columns.

Consider now, an arbitrary i 'th row and an arbitrary j 'th point located within that row, say point $g(j)$. Then around this point, there exists a two-dimensional zone within which there is significant correlation relating point $g(j)$ to other points within the i 'th row, and with points in any adjacent $(i \pm \beta)$ 'th row. As verified by the form of Eq. (2.13), the strength of this correlation decays with increases in β and τ_R , if at least some damping coefficients are non-zero. However,

by the assumption of stationarity, an equivalent zone of correlation exists around each and every other point in the image. In terms of the underlying signal process, the cross-row correlation corresponds to a phase shift between rows, which has been introduced by the column component of the two-dimensional signal process. Furthermore, prior to any filtering procedure, there will also exist an additive noise component which has significant correlation both within and between rows. Consequently, in terms of its rows, an unfiltered $N_c \times N_R$ image consists of a set, X , of one-dimensional, noise-perturbed, phase-shifted processes defined as:

$$\begin{aligned} X &= \{x_i \mid i=1, \dots, N_c\} \\ &= \{\{x_1(j) \mid j=1, \dots, N_R\}, \{x_2(j) \mid j=1, \dots, N_R\}, \dots, \{x_{N_c}(j) \mid j=1, \dots, N_R\}\} \end{aligned} \quad (2.24)$$

In a block-adaptive filtering approach, it is desired to derive a set of coefficients, $h = \{h_{ij}(r|\alpha, \beta) \mid r=0, 1, \dots, \xi-1\}$, where the $h_{ij}(r|\alpha, \beta)$ are coefficients belonging to a linear operator of some length ξ . This operator has been designed based on the relationships existing between all x_i and $x_{i,\beta}$ which are $\in X$, where β is some integer which is held constant when obtaining estimates over all the x_i . The information which is required in order to construct this operator, is found within the zone of correlation which surrounds each point in the image.

An estimate of the desired signal occurring within each noisy x_i is represented by the set $\hat{g} = \{\hat{g}_i(j|\alpha, \beta) \mid j=1, \dots, N_R\}$; it may be obtained by applying the linear operator to each $x_{i,\beta}$ via the following convolution operation:

$$\hat{g}_i(j|\alpha, \beta) = \sum_{r=0}^{\xi-1} h_{xy}(r|\alpha, \beta) x_{i,\beta}(j-r-\alpha) \quad (2.25)$$

where α is the length of the prediction gap of the filter. By applying this operation to all elemental subsets of X , it is possible to produce a new set of phase-shifted, one-dimensional, noise-suppressed signal processes, \hat{G} , defined as:

$$\begin{aligned}
\hat{G} &= \{ \hat{g}_i | i=1, \dots, N_C \} \\
&= \{ \{ \hat{g}_1(j | \alpha, \beta) | j=1, \dots, N_R \}, \{ \hat{g}_2(j | \alpha, \beta) | j=1, \dots, N_R \}, \dots, \{ \hat{g}_{N_C}(j | \alpha, \beta) | j=1, \dots, N_R \} \}
\end{aligned}
\tag{2.26}$$

The ultimate product then, is an estimate of the set of one-dimensional signal processes existing in the rows of the image; within this noise-suppressed domain it is possible to obtain more accurate information regarding the signal of interest. For convenience in subsequent notation, observe that \hat{g}_i and \hat{G} are the filtered estimates of their respective actual image components, g_i and G . The desired linear operator which will yield such estimates is the scalar Wiener filter, described in [26], [27], and derived in the next Subsection.

2.5.2 Scalar Wiener Filter: Mathematical Derivation

To formally introduce the derivation of a scalar Wiener filter, begin by considering a case where, for all $x_i \in X$, it is desired to derive a set, h , comprised of ξ linear function coefficients, $h_{xy}(r | \alpha, \beta)$; here, the subscript xy denotes the transfer function of row y into row x . This function is to operate on the row process set $y \equiv x_{i,\beta}$, for the purpose of predicting each j 'th value of the signal process occurring within some proximal, phase-shifted set, $x \equiv x_i$. The prediction is to be based on ξ previous points in the sequence $y \equiv x_{i,\beta}$. Furthermore, relative to the j 'th value of $x \equiv x_i$, the nearest point of row $y \equiv x_{i,\beta}$ is α steps in the past, along the row dimension. This relationship may then be summarized as:

$$h_{xy}(0 | \alpha, \beta) x_{i,\beta}(j - \alpha) + h_{xy}(1 | \alpha, \beta) x_{i,\beta}(j - \alpha - 1) + \dots + h_{xy}(\xi - 1 | \alpha, \beta) x_{i,\beta}(j - \alpha - \xi + 1) = x_i(j)
\tag{2.27}$$

If $\alpha = l$, then this is the one-step predictor commonly referred to in the literature [27]. The derivation process is commenced by rewriting Eq. (2.27) in vector notation as:

$$[h_{xy}(0 | \alpha, \beta) \quad h_{xy}(1 | \alpha, \beta) \quad \dots \quad h_{xy}(\xi-1 | \alpha, \beta)] \times \begin{bmatrix} x_{i,\rho}(j-\alpha) \\ x_{i,\rho}(j-\alpha-1) \\ \vdots \\ x_{i,\rho}(j-\alpha-\xi+1) \end{bmatrix} = x_i(j) \quad (2.28)$$

Multiplying both sides of Eq. (2.28) by the transpose of the stochastic process vector now gives:

$$\begin{aligned} & [h_{xy}(0 | \alpha, \beta) \quad h_{xy}(1 | \alpha, \beta) \quad \dots \quad h_{xy}(\xi-1 | \alpha, \beta)] \times \\ & \begin{bmatrix} x_{i,\rho}(j-\alpha)x_{i,\rho}(j-\alpha) & x_{i,\rho}(j-\alpha)x_{i,\rho}(j-\alpha-1) & \dots & x_{i,\rho}(j-\alpha)x_{i,\rho}(j-\alpha-\xi+1) \\ x_{i,\rho}(j-\alpha-1)x_{i,\rho}(j-\alpha) & x_{i,\rho}(j-\alpha-1)x_{i,\rho}(j-\alpha-1) & \dots & \vdots \\ \vdots & \vdots & \ddots & \vdots \\ x_{i,\rho}(j-\alpha-\xi+1)x_{i,\rho}(j-\alpha) & \dots & \dots & x_{i,\rho}(j-\alpha-\xi+1)x_{i,\rho}(j-\alpha-\xi+1) \end{bmatrix} \\ & = [x_i(j)x_{i,\rho}(j-\alpha) \quad x_i(j)x_{i,\rho}(j-\alpha-1) \quad \dots \quad x_i(j)x_{i,\rho}(j-\alpha-\xi+1)] \end{aligned} \quad (2.29)$$

Upon taking expectations of Eq. (2.29) for all i and all j , the following result is obtained:

$$\begin{aligned} & [h_{xy}(0 | \alpha, \beta) \quad h_{xy}(1 | \alpha, \beta) \quad \dots \quad h_{xy}(\xi-1 | \alpha, \beta)] \times \\ & \begin{bmatrix} r_{xy}(0 | 0) & r_{xy}(1 | 0) & \dots & r_{xy}(\xi-1 | 0) \\ r_{xy}(-1 | 0) & r_{xy}(0 | 0) & \dots & \vdots \\ \vdots & \vdots & \ddots & \vdots \\ r_{xy}(-\xi+1 | 0) & \dots & \dots & r_{xy}(0 | 0) \end{bmatrix} \\ & = [r_{xy}(\alpha | \beta) \quad r_{xy}(\alpha+1 | \beta) \quad \dots \quad r_{xy}(\alpha+\xi-1 | \beta)] \end{aligned} \quad (2.30)$$

Where $r_{xy}(\tau_k | \beta)$ denotes the regional expectation of the one-dimensional CCF for any two rows of the image which are β steps apart, and $r_{xx}(\tau_k | 0)$ represents the regional expectation of the one-dimensional ACF for $x_{i,\rho}$. Note here, that since the RHS of Eq. (2.30) is dependent upon both α and β , then the scalar transfer function occurring on the LHS is also dependent on these parameters; this necessitates use of the notation $h_{xy}(r | \alpha, \beta)$. As well, for notational convenience during subsequent references, Eq. (2.30) may be expressed as:

$$h_{i,\tau} \times R_{\tau,t} = r_{i,\tau} \quad (2.31)$$

The solution for $h_{i,\tau}$ is achieved by multiplying both sides of Eq. (2.30) by the inverse of $R_{\tau,t}$.

2.5.3 Prediction Effectiveness of the Scalar Wiener Filter

The preceding discussions imply that a given realization of the row process, in row $i+\beta$ say, may be used to make predictions about another realization of the same process, in row i say, which is β steps away in the column dimension. This predictability relies upon that relationship which must exist between signal processes in the rows in order that signal processes in the columns be preserved. Within their zone of significant correlation, the individual realizations of the row signal process are not mutually stochastically independent; hence, the behaviour of row $i+\beta$ must have implications for the behaviour of row i . There are however, practical limitations to this assumption of predictability, both between rows and within rows. Such limitations are directly related to the characteristics of the zone of correlation which surrounds each point in the image.

In order that the relationship between filter effectiveness and correlation characteristics of the signal process may be fully understood, it will now be necessary to examine the characteristics of a general linear operator which makes predictions on a noise-free process. Given this, consider the situation in which a two-dimensional stochastic process, $g(i,j)$, exists in an image which is free of noise; the j 'th element within the i 'th row component of this process is represented as $g_i(j)$. In such an instance, it is easy to see that Eq. (2.25) becomes:

$$\hat{g}_i(j|\alpha, \beta) = \sum_{r=0}^{\xi-1} h_{\alpha\beta}(r|\alpha, \beta) g_{i,\beta}(j-r-\alpha) \quad (2.32)$$

where the symbol $\hat{\cdot}$ is used to denote the estimated value of $g_i(j)$ which has been obtained in the absence of noise. Now, if $\tilde{g}_i(j|\alpha, \beta)$ is the estimated value associated with the actual value of $g_i(j)$,

then row process g_i is considered to be *predictable* if:

$$\hat{g}_i(j | \alpha, \beta) - g_i(j) = 0, \quad \text{for all } i \text{ and all } j \quad (2.33)$$

It can be shown [28] that this relationship holds *if and only if* the autospectrum of g_i consists of lines, in the form represented by Eq. (2.19). Of course, it follows from previous discussions that the expected autospectrum of g_i is also the expected autospectrum of $g_{i,p}$, for all i and all β ; this permits the application of Eq. (2.33) to the cross-channel prediction in Eq. (2.32). Consequently, unless the expected autospectrum of g_i consists only of lines, the generating stochastic process is not predictable. In Section 2.4.3, it was shown that for the case of non-zero damping coefficients, $G_{n_i}(f|\alpha,\beta)$ could never be represented as a line spectrum. Hence, for Cases II and III in Section 2.3, it now follows that the output of the Wiener filter from the noise-free operation of Eq. (2.32) cannot satisfy Eq. (2.33).

If a process does not satisfy these conditions, it is possible that it may be described as *weakly predictable*, provided that its spectrum is band-limited. This definition requires that $G_{n_i}(f|\alpha,\beta) = 0$ for $f > \varphi$, where φ is some value between 0 and π . However, for the situation which is of primary interest in this thesis, namely that of Case II data, g_i is merely bandpass. Therefore, as shown by Eq. (2.21), it will have an expected autospectrum which is non-zero for all f , since there are non-zero damping coefficients in the expected ACF. Hence, except for Case I, the process represented by the expected ACF cannot be band-limited, and therefore it does not satisfy the condition for weak predictability. It now follows that $G_{n_i}(f|\alpha,\beta)$ in Case II, and $G_{n_i}(f|\alpha,\beta)_i$ in Case III, both satisfy the definition of an *unpredictable* process as discussed in [28].

This introduces Wold's decomposition, which states that any arbitrary unpredictable process, g_i , say, may be written as the sum:

$$g_i = g_{i,r} + g_{i,p} \quad (2.34)$$

where $g_{i,r}$ is known as a *regular* process, and $g_{i,p}$ is a predictable process. Furthermore, $g_{i,r}$ and

$g_{i,p}$ are orthogonal in the statistical sense, that is $\mathcal{E}\{g_{i,p}(f) \cdot g_{i,r}(f)\} = 0$. Hence, $g_{i,r}(f)$ is a component of $g_i(f)$ which cannot be determined from previous values of the sequence, say $g_i(a)$ for $a < j$. On the other hand, $g_{i,p}(f)$ is predicted exactly by these previous values in the sequence. In fact, it has been shown that if $\tilde{g}_i(f|\alpha, \beta)$ is the predicted value of $g_i(f)$ obtained in the absence of noise, then it must also be the predicted value of $g_{i,p}(f)$, and $\tilde{g}_i(f|\alpha, \beta) = g_{i,p}(f)$ since the regular process component, $g_{i,r}(f)$, cannot be determined from the prediction operation [28]. It can further be shown that $g_{i,p}$ has a spectrum which consists of lines, whereas $g_{i,r}$ has a spectrum which is non-zero for all f and which does not contain lines. The resulting implications for Case II correlation data, is that process g_i may be separated into a component which is predictable by $h_{i,t}$ within Eq. (2.31), and a component which cannot be predicted. For Case III it is seen that there are two predictable components; one has the spectral representation of $G_{yy}(f|\alpha, \beta)$, from Eq. (2.23), and arises naturally due to the undamped portion of the ACF; the other may be defined as $G_{yy}(f|\alpha, \beta)_{sp}$ which arises due to Wold's decomposition of $G_{yy}(f|\alpha, \beta)_e$.

A prolonged examination of the implications arising from these observations is not warranted. In preparation for subsequent discussions, it is merely sufficient to establish a general conclusion for Cases II and III, that, in the absence of noise, $\tilde{g}_i(f|\alpha, \beta) \neq g_i(f)$, hence:

$$\mathcal{E}\{[\tilde{g}_i(f|\alpha, \beta) - g_i(f)]^2\} = \epsilon > 0, \quad \text{for all } i \text{ and for all } j \quad (2.35)$$

Consequently, except for Case I, *even in the absence of noise contamination* there will exist a finite non-zero error variance, ϵ , due to differences between the predicted and actual values of g_i .

2.5.4 Scalar Wiener Filter: Frequency-Domain Transfer Function

In order to address the noise-suppression characteristics of the scalar Wiener filter, it is necessary to examine its performance in the frequency domain. To facilitate this, begin by observing that Eq. (2.30) may be rewritten as:

$$\left\{ \sum_{b=0}^{\xi-1} h_{xy}(b | \alpha, \beta) r_{xy}(\kappa-b | 0) \right\}, \left\{ \sum_{b=0}^{\xi-1} h_{xy}(b | \alpha, \beta) r_{xy}(1-b | 0) \right\}, \dots, \left\{ \sum_{b=0}^{\xi-1} h_{xy}(b | \alpha, \beta) r_{xy}(\xi-1-b | 0) \right\} \Bigg\} \\ = [r_{xy}(\alpha | \beta) \quad r_{xy}(\alpha+1 | \beta) \quad \dots \quad r_{xy}(\alpha+\xi-1 | \beta)] \quad (2.36)$$

This reduces to the Wiener-Hopf equations [26]; recalling that c denotes the extent of noise correlation, and that by choosing $\alpha > c$ it is possible to exclude the noise component from the RHS of Eq. (2.36), the Wiener-Hopf equations may be expressed as:

$$\sum_{b=0}^{\xi-1} h_{xy}(b | \alpha, \beta) r_{xy}(\kappa-b | 0) = r_{gxy}(\kappa+\alpha | \beta), \quad \text{for } \kappa = 0, \dots, \xi-1 \quad \text{AND } \alpha > c \\ \sum_{b=0}^{\xi-1} h_{xy}(b | \alpha, \beta) r_{gxy}(\kappa-b | 0) + \sum_{b=0}^{\xi-1} h_{xy}(b | \alpha, \beta) r_{nxy}(\kappa-b | 0) = r_{gxy}(\kappa+\alpha | \beta) \quad (2.37)$$

The frequency-domain transfer function may be derived by use of the Discrete Fourier Transform, previously defined in Eq. (2.16). Therefore, multiplying both sides of Eq. (2.37) by $e^{i\ell\kappa}$ and taking summations over κ , gives the one-sided spectral representation of the DFT with $\alpha > c$, as:

$$\sum_{\kappa=0}^{\xi-1} \left\{ \sum_{b=0}^{\xi-1} h_{xy}(b | \alpha, \beta) r_{gxy}(\kappa-b | 0) \right\} e^{i\ell\kappa} + \sum_{\kappa=0}^{\xi-1} \left\{ \sum_{b=0}^{\xi-1} h_{xy}(b | \alpha, \beta) r_{nxy}(\kappa-b | 0) \right\} e^{i\ell\kappa} = \\ \sum_{\kappa=0}^{\xi-1} r_{gxy}(\kappa+\alpha | \beta) e^{i\ell\kappa} \quad (2.38)$$

Since, by the properties of the DFT, a time-domain convolution maps to a multiplication operation in the frequency domain, the final result of Eq. (2.38) is a summed product of spectral density functions, expressed as:

$$H_{xy}(f | \alpha, \beta) G_{xy}(f | 0) + H_{xy}(f | \alpha, \beta) N_{xy}(f | 0) = G_{xy}(f | \alpha, \beta) \quad (2.39)$$

Study of Eq. (2.38) will verify that the bandpass spectral estimates on the LHS of Eq. (2.39), are derived from a different set of correlation coefficients than are those on the RHS; however, if

$\alpha < \xi$, then there will be some degree of intersection between the sets. Moreover, the estimate occurring on the RHS is, in general, dependent upon variations in α and β , whereas the estimate from the LHS is not affected by changes in these parameters. Finally then, the frequency-domain transfer function for the scalar Wiener filter may be expressed as:

$$H_{xy}(f | \alpha, \beta) = \frac{G_{xy}(f | \alpha, \beta)}{G_{xy}(f | 0) + N_{xy}(f | 0)} \quad (2.40)$$

Inspection of this equation will readily confirm that since the numerator is affected by changes in α and β , given Case II or Case III spectra, a unique frequency response cannot be obtained. Therefore, a very significant ramification is that the magnitude response characteristics for the passband of this filter will change with any variations in either α or β . In fact, it is only for Case I spectra that the passband magnitude will remain constant over all possible values of these two parameters. In effect then, for Cases II and III, each form of $H_{xy}(f | \alpha, \beta)$ which results from each unique combination of α and β , represents a different realization of Wold's decomposition for the process which is being operated on; some realizations will be closer approximations to the actual signal process than others will be. From this, it also follows that prediction accuracy, as measured by ε in Eq. (2.35), must also vary according to the parametric values which determine the shape of $G_{xy}(f | \alpha, \beta)$.

Of course, the relative phase delay characteristics between frequencies within the transfer function of the filter will also change for Cases II and III, due to variations in the shape parameters of the CCF. This is a direct consequence of the interactions which occur between several non-zero complex terms within $G_{xy}(f | \alpha, \beta)$, which forms the cross-spectrum within the numerator of Eq. (2.40). Further to this, however, it is also very important to understand that the Wiener filter derivation procedure seeks only to minimize the estimation error, ε in Eq. (2.35), for any chosen α and β . This reduces to an optimization problem which imposes no additional constraints on the solution [27]. In particular, there exists no constraint that the filtered output be

undistorted, with respect to the original phase relationships existing between frequencies within process g . This means that, in general, the filtered output will be phase-distorted for all three cases of the CCF previously described. It will later be seen that this distortion can be reversed during the actual filtering operation.

As a final observation, note that in the case of coherent noise, the value of $N_o(f, \theta)$ is not constant for all f . In fact, the noise spectrum tapers such that the magnitude decreases with increasing f . Given the relationship defined by Eq. (2.40), it is easy to see that this uneven noise spectrum will induce a different gain factor for each value of f . This too, will occur under all three cases of the CCF previously described, and implies that even for Case I data, the desired signal cannot be perfectly recovered.

Based on these considerations, it is possible to conclude that a Wiener filter operating in a gapped prediction mode, can never completely recover a stationary process which has been contaminated by coherent noise; hence, for such situations it is a general rule that $\tilde{g}_o(f|\alpha, \beta) \neq g_o(f)$. This establishes one source of error for the filtering technique which is being developed.

2.5.5 The Scalar Filtering Operation

To investigate the effectiveness of the scalar Wiener filter, begin by observing the relationship represented by Eq. (2.40). From comparison of the numerator and denominator terms, it is seen that frequencies which occur with very low magnitude within the signal process, but which occur in the noise process with relatively high magnitude, will lead to a frequency response which is of minimal amplitude. These frequencies comprise the stopband of the filter, and will be suppressed during the filtering operation; it is easy to see that this relationship further impedes the predictability of a bandpass signal, since its lowest-power frequencies will be attenuated. However, frequencies which possess power levels that are approximately equivalent within both

the noise and signal processes, will remain relatively unattenuated; such frequencies will therefore comprise the passband of the filter.

To provide a formal illustration, based on a one-sided spectral representation, let G_f denote the subset of frequencies having significantly above-nominal magnitudes within the spectrum of row signal process g_n , and let N_f be the set of frequencies found in the noise process. By definition, this latter set will contain components from all digital frequencies $0 \leq f \leq \pi$, whereas the former set will contain only some values of f . Similarly, let P_f be the set of unattenuated frequencies which define the passband of the filter, and let S_f represent the set of suppressed frequencies which comprise the stopband. Given these conventions, the passband and stopband relationships may be formally represented as:

$$\begin{aligned} P_f &= G_f \cap N_f = G_f \\ S_f &= N_f - G_f \cap N_f = N_f - G_f \end{aligned} \tag{2.41}$$

Hence, the filter is capable only of suppressing those frequency components of the noise process, which have significantly greater magnitudes than their respective components within the signal process. This reveals that a portion of the noise process will be passed by the filter and continue to contaminate the estimate, \hat{g}_n , of the row process. In fact, the bandwidth of that portion of the noise process which is unsuppressed by the filter, is proportional to the bandwidth of significantly powerful frequencies found within the signal process. The resulting implication is that for any fixed level of noise, effectiveness of the filter will decrease if this effective bandwidth of the signal process is extended.

This establishes a second source of error for the filter, and prompts the rewriting of Eq. (2.25) as:

$$\begin{aligned}
\hat{g}_i(j|\alpha, \beta) &= \sum_{r=0}^{\xi-1} h_{xy}(r|\alpha, \beta) g_{i,\beta}(j-r-\alpha) + \sum_{r=0}^{\xi-1} h_{xy}(r|\alpha, \beta) n_{i,\beta}(j-r-\alpha) \\
&= \tilde{g}_i(j|\alpha, \beta) + \sum_{r=0}^{\xi-1} h_{xy}(r|\alpha, \beta) n_{i,\beta}(j-r-\alpha) \\
\therefore \hat{g}_i(j|\alpha, \beta) &= \tilde{g}_i(j|\alpha, \beta) + \hat{n}_i(j|\alpha, \beta)
\end{aligned} \tag{2.42}$$

where $\hat{n}_i(j|\alpha, \beta)$ is a filtered version of the noise process. Therefore, it has now been shown that $\hat{g}_i(j|\alpha, \beta)$ has two sources of error; one source arises due to the fact that only some components of g_i are predictable, while another occurs because the Wiener filter cannot suppress all noise frequencies.

Based on these conclusions, the one-sided spectrum of \hat{x}_i may now be represented as:

$$\hat{G}_i(f|\alpha, \beta) = |\tilde{G}_i(f|\alpha, \beta)| e^{-j\theta_i(f|\alpha, \beta)} + |\hat{N}_i(f|\alpha, \beta)| e^{-j\theta_i(f|\alpha, \beta)} \tag{2.43}$$

Whereupon it is seen that the LHS is the complex resultant of two independent complex terms occurring on the RHS. Of particular relevance, is the fact that due to the independence of the signal and noise processes, the phase of the noise process is not in any way related to the phase of the signal process. Momentarily ignoring any distortions which may be imposed on $\tilde{G}_i(f|\alpha, \beta)$ due to non-linear phase attributes of the filter, it is seen that $\hat{G}_i(f|\alpha, \beta)$ will be phase-distorted due to the additive effect of the residual noise, $\hat{N}_i(f|\alpha, \beta)$, which is generally not in phase with $\tilde{G}_i(f|\alpha, \beta)$. Consequently, that portion of the noise process which is retained will continue to distort the desired signal. Although the filtered result will represent a significant improvement over the unfiltered version, it will still possess a finite signal-to-noise ratio expressed as:

$$SNR_I = \frac{|\tilde{G}_i(f|\alpha, \beta)|^2}{|\hat{N}_i(f|\alpha, \beta)|^2} \tag{2.44}$$

where the subscript I has been used to denote the fact that this SNR results from the one-channel Wiener filter.

While the retention of noise is unavoidable, in principle it is possible to modify the filtering operation in order to minimize this problem. In this regard, the objective will now be to derive three distinct versions of the scalar transfer function, h_{ij} . For the sake of this immediate discussion, it will be assumed that the signal correlation data are *unaffected by changes in either α or β* , so that all three filters will have an identical frequency response. Pursuant to this, suppose three values are defined for β ; specifically, let these be $-\beta$ and $+\beta$ for $\beta > c$, and $\beta = 0$. Then, let row $x_{i,\beta}$ be referenced as the Channel 1 input, row x_i as the Channel 2 input, and row $x_{i,\beta}$ as the Channel 3 input. Furthermore, in order to simplify notation, let $x_i \equiv x_{i,\beta}$, $x_2 \equiv x_i$, and $x_3 \equiv x_{i,\beta}$, for any i or β ; therefore, x_1 represents the $(i-\beta)$ 'th row, x_2 represents row i , and x_3 represents row $(i+\beta)$. Given this, h_{21} is the time-domain transfer function of Channel 1 into the row estimate for Channel 2, or equivalently, row $x_{i,\beta}$ into row estimate \hat{g}_i . Similarly, h_{22} is the transfer function of x_i into row estimate \hat{g}_i , and h_{23} describes the mapping of $x_{i,\beta}$ into \hat{g}_i .

By operating on their respective $(i-\beta)$ 'th, i 'th, and $(i+\beta)$ 'th rows, the three transfer functions each produce an estimate, \hat{g}_i , of the signal process, g_i , existing in the i 'th row. These operations may now be summarized as:

$$\begin{aligned}
 \hat{g}_{21}(j) &= \sum_{r=0}^{\xi-1} h_{21}(r) x_1(j-r-\alpha) \\
 \hat{g}_{22}(j) &= \sum_{r=0}^{\xi-1} h_{22}(r) x_2(j-r-\alpha) \\
 \hat{g}_{23}(j) &= \sum_{r=0}^{\xi-1} h_{23}(r) x_3(j-r-\alpha)
 \end{aligned} \tag{2.45}$$

where the notation on the LHS denotes the estimate of the Channel 2 process, based on the inputs from Channels 1, 2, or 3. An estimate of the desired signal process for any i 'th row is then expressed as:

$$\hat{g}_2(j) = \frac{1}{3} \sum_{k=1}^3 \hat{g}_{2k}(j) \quad (2.46)$$

This technique incorporates a distinct noise-suppression advantage over the one-channel approach, which is best understood through a frequency-domain representation. Therefore, taking Fourier transforms of the filter outputs in Eq. (2.45) yields a three-channel version of Eq. (2.43), represented as:

$$\begin{aligned} \hat{G}_{21}(f) &= |\hat{G}_2(f)|e^{-j\theta_2(f)} + |\hat{N}_2(f)|e^{-j\alpha_1'(f)} \\ \hat{G}_{22}(f) &= |\hat{G}_2(f)|e^{-j\theta_2(f)} + |\hat{N}_2(f)|e^{-j\alpha_2''(f)} \\ \hat{G}_{23}(f) &= |\hat{G}_2(f)|e^{-j\theta_2(f)} + |\hat{N}_2(f)|e^{-j\alpha_2''(f)} \end{aligned} \quad (2.47)$$

This notation implies that the phase values for all three estimates of the signal process are equal, whereas the phase values for the noise estimates are unequal. To understand this, recall via Eq. (2.40), that the cross-channel transfer functions, h_{2j} and h_{j2} , will incorporate information from the CCF proper. Further to this, by Eqs. (2.20) and (2.18), it has been shown that the CCF retains information describing the relative phase relationships, which exist between the individual row components of the signal process. The incorporation of this phase information into the cross-channel transfer functions, enables these operators to either delay or advance their respective outputs. This is needed, in order that the phase of the signal estimates from Channels 1 and 3, may match the phase of the signal estimate from Channel 2. It is facilitated by the fact that the distance between rows, β , is chosen such that a significant correlation continues to exist between the signal components. However, recall also that this separation distance exceeds the zone of correlation for the noise process, since $\beta > c$. Consequently, the filters have no cross-channel phase information pertaining to the noise process. In fact, for β so restricted, there will be no phase coherence between noise components existing within any two rows which are separated by this distance. Therefore, phase adjustments by the cross-channel filters will properly synchronize

the phases of the signal estimates, but cannot synchronize the phases of those noise frequencies which are also passed, because no consistent cross-channel relationship exists between the noise components. Given that the phase terms of the noise in Eq. (2.47) are random variables, the absence of significant correlation does not necessarily imply that they are independent, however, it does imply that their covariance is zero. This increases the likelihood that, in general:

$$\Omega_2'(f) \neq \Omega_2''(f) \neq \Omega_2'''(f) \quad (2.48)$$

In other words, it is unlikely that these three terms will be equal, after the filtering operation has been performed on any given row triplet in the image; a fact which has been represented in Eq. (2.47).

For the one-sided spectral representation given in Eq. (2.47), it is also seen that the predicted components of the signal process, and the filtered versions of the noise process, are all complex-valued. Ignoring the scalar value of $\frac{1}{3}$, it is seen that the operation in Eq. (2.46) involves the sum of three estimates of the desired signal, and the sum of three filtered versions of the noise process; consequently, the final estimate must still retain a noise component. However, in calculating the SNR, it is apparent that the following relationship will exist for the numerator term:

$$\left| \tilde{G}_2(f)e^{-j\theta_2(f)} + \tilde{G}_2(f)e^{-j\theta_2(f)} + \tilde{G}_2(f)e^{-j\theta_2(f)} \right| = 3 \left| \tilde{G}_2(f) \right| \quad (2.49)$$

This will hold because the three estimates of the signal process are equal in magnitude and phase. However, while the noise components are also equal in magnitude, they are generally unequal in phase. Consequently, summation of the noise terms will yield the relationship:

$$\left| \dot{N}_2(f)e^{-j\alpha_2'(f)} + \dot{N}_2(f)e^{-j\alpha_2''(f)} + \dot{N}_2(f)e^{-j\alpha_2'''(f)} \right| \leq 3 \left| \dot{N}_2(f) \right| \quad (2.50)$$

It now follows that for the three-channel version of the filtering technique, the SNR of the estimate is expressed as:

$$SNR_3 \geq \frac{9|\bar{G}_2(f)|^2}{9|\bar{N}_2(f)|^2} = \frac{|\bar{G}_2(f)|^2}{|\bar{N}_2(f)|^2} = SNR_1 \quad (2.51)$$

$$\therefore SNR_3 \geq SNR_1$$

Hence, for the ideal situation defined above, the SNR achieved via the one-channel filter is the lower limit of the SNR which is achievable via the three-channel application. However, if the restriction that the three passbands be identical is now relaxed, it is clear that with a Case II or Case III CCF, the transfer functions will not be identical and, equally important, their frequency responses will change with adjustments to α and β . Yet, with reference to Eq. (2.51), it is seen that any changes which this might impose on the numerator will also be imposed equally on the denominator; since these are linear operations, it follows that the inequality $SNR_3 \geq SNR_1$ will continue to hold.

A major concern with the three-channel approach defined by Eq. (2.45), is that each filter has been derived independently of the other two. Deriving each filter in this manner, excludes information pertaining to the inter-relationships which exist between all three of the input channels. Such information will be crucial in ensuring that all three filters, despite their different frequency responses, are collectively able to reflect the potentially intricate phase and magnitude relationships which exist between and within the rows of the image. In cases such as this, the use of vector-based multi-channel filtering operations is highly recommended, because they have been developed for this type of problem. This now provides motivation for addressing the noise suppression problem via the principles of vector stochastic process theory, and vector Wiener filtering; such methods will be discussed in the next Section.

2.6 Block-Adaptive Wiener Filter for Vector Stochastic Processes

2.6.1 Overview

The objective now is to develop a vector version of the scalar three-channel filtering array proposed in the previous Section. Within this discussion, vector operations will be limited to three-channel versions of the filters, however, extensions to higher dimensions are certainly achievable. To begin, consider that a three-component vector stochastic process, $x_{i(j)}$, is defined as [17]:

$$x_{i(j)} = \{ [x_i(j)]_{3 \times 1} = [x_{i-\beta}(j) \ x_i(j) \ x_{i+\beta}(j)]^T \mid j=1, \dots, N_R \} \quad (2.52)$$

where $x_{i(j)}$ is a subset consisting of vector elements. Each vector element, $[x_i(j)]_{3 \times 1}$, contained in this subset, denotes a triple-scalar observation obtained from the j 'th position within each of three row stochastic processes. The vector is centred on the i 'th row, from which it acquires its second scalar element, $x_i(j)$, with the first and third scalar elements, $x_{i-\beta}(j)$ and $x_{i+\beta}(j)$, coming from rows $i-\beta$ and $i+\beta$ respectively. In order to avoid ambiguity in notation, the process realizations occurring in the $(i-\beta)$ 'th, the i 'th, and the $(i+\beta)$ 'th rows correspond, respectively, to the Channel 1, Channel 2, and Channel 3 inputs of the three-channel vector Wiener filter which will be derived; this convention is identical to that which was established in Section 2.5.5. The entire image is then perceived as consisting of a set, X_j , of such three-channel row process subsets:

$$\begin{aligned} X_j &= \{ x_{i(j)} \mid i=(\beta+1), \dots, (N_C-\beta) \} \\ &= \{ \{ [x_{\beta+1}(j)]_{3 \times 1} \mid j=1, \dots, N_R \}, \{ [x_{\beta+2}(j)]_{3 \times 1} \mid j=1, \dots, N_R \}, \dots, \{ [x_{N_C-\beta}(j)]_{3 \times 1} \mid j=1, \dots, N_R \} \} \end{aligned} \quad (2.53)$$

Inspection of Eqs. (2.52) and (2.53) will reveal that with respect to actual rows of the image, there must exist some overlap between the $x_{i(j)} \in X_j$. In particular, consider any arbitrary $x_{i(j)}$ centred on the i 'th row of the image; concurrent with this, consider another arbitrary vector process in X_j , $x_{i'+k(i)}$ say, which is centred on the $(i+k)$ 'th row of the image. The common content between these

two vector processes, in terms of physical rows from the image, is determined from the value taken by k in relation to the value which has been chosen for β . The image rows which comprise the intersection of these two vector processes may now be defined as:

$$\begin{aligned} x_{(t)(3)} \cap x_{(t,k)(3)} &= \{ \{x_r(j) \mid j=1, \dots, N_R\}, \{x_{r,\beta}(j) \mid j=1, \dots, N_R\} \}, \text{ for } k = \beta \\ x_{(t)(3)} \cap x_{(t,k)(3)} &= \{ \{x_{r,\beta}(j) \mid j=1, \dots, N_R\} \}, \text{ for } k = 2\beta \\ x_{(t)(3)} \cap x_{(t,k)(3)} &= \emptyset, \text{ otherwise} \end{aligned} \quad (2.54)$$

Some extremely important ramifications which arise due to the relationships within Eq. (2.54), will be discussed later, in Section 2.7.3.

By utilization of vector Wiener filter theory, it is sought to derive a set, h_j , of linear matrix operator coefficients, defined as:

$$h_3 = \{ [h_{xy}(r | \alpha, \beta)]_{3 \times 3} \mid r=0, 1, \dots, \xi-1 \} \quad (2.55)$$

where the r 'th element of h_3 is the 3×3 matrix:

$$[h_{xy}(r | \alpha, \beta)]_{3 \times 3} = \begin{bmatrix} h_{11}(r | \alpha, \beta) & h_{12}(r | \alpha, \beta) & h_{13}(r | \alpha, \beta) \\ h_{21}(r | \alpha, \beta) & h_{22}(r | \alpha, \beta) & h_{23}(r | \alpha, \beta) \\ h_{31}(r | \alpha, \beta) & h_{32}(r | \alpha, \beta) & h_{33}(r | \alpha, \beta) \end{bmatrix} \quad (2.56)$$

The elements of each 3×3 block represent the coefficients of scalar time-domain transfer functions, between the subscripted input channels at the r 'th lag. For each scalar transfer function, the notational convention is identical to that which was established in Section 2.5.5, that is, h_{21} represents the scalar transfer function which maps the Channel 1 input into the estimate for Channel 2, and so on. The set h_3 can be used to form a block vector, h_{j-t} , of block element size $I \times \xi$, within which, each block element consists of a 3×3 matrix of scalar elements. Forming the inner product between h_{j-t} , and a $\xi \times I$ block-element observation vector comprised of the ξ ($3 \times I$) scalar-element blocks, $[x_r(j)]_{1..n}$, will then result in the following block convolution operation:

$$[\hat{g}_i(j | \alpha, \beta)]_{3 \times 1} = \sum_{r=0}^{i-1} [h_{xy}(r | \alpha, \beta)]_{3 \times 3} [x_{i-j-r-\alpha}]_{3 \times 1} \quad (2.57)$$

where $[x_{i-j-r-\alpha}]_{3 \times 1}$ represents the appropriately lagged triple-scalar block-element of vector process $x_{i(t)}$, which is centred on the i 'th row of the image. This then, is the vector version of the three-channel array of scalar transfer functions defined in the previous Section. The output from Eq. (2.57) is a three-element vector, which consists of estimates of the row signal processes occurring on each of the input channels:

$$[\hat{g}_i(j | \alpha, \beta)]_{3 \times 1} = [\hat{g}_{i-\beta}(j | \alpha, \beta) \quad \hat{g}_i(j | \alpha, \beta) \quad \hat{g}_{i+\beta}(j | \alpha, \beta)]^T \quad (2.58)$$

If only the Channel 2 output is retained after the filter operates on each row triplet, then the final product is the set \hat{G}_2 , defined as:

$$\begin{aligned} \hat{G}_2 = & \{ \hat{g}_i | i = (\beta+1), \dots, (N_C - \beta) \} \\ & = \{ \{ \hat{g}_{\beta+1}(j | \alpha, \beta) | j = 1, \dots, N_R \}, \dots, \{ \hat{g}_{N_C - \beta}(j | \alpha, \beta) | j = 1, \dots, N_R \} \} \end{aligned} \quad (2.59)$$

Note how the three-channel configuration of the operator dictates that the 2nd (i 'th row) input channel, can never coincide with the rows $i = 1, \dots, \beta$ or $i = N_C - \beta + 1, \dots, N_C$. Consequently, for rows $i = 1, \dots, \beta$, output estimates from Channel 1 must be used, whereas for rows $i = N_C - \beta + 1, \dots, N_C$, the Channel 3 estimates are used. Denoting the former set of estimates as \hat{G}_1 , and the latter as \hat{G}_3 , the entire filtered image is then represented as $\hat{G} = \hat{G}_1 \cup \hat{G}_2 \cup \hat{G}_3$. The mathematical means by which these estimates may be realized will now be examined.

2.6.2 Three-Channel Wiener Filter: Mathematical Derivation

The procedure by which a multi-channel Wiener filter may be derived is discussed extensively in [29] & [30]. The three-channel version conforms to the same mathematical

principles as for the more general case; moreover, the derivation for any number of channels is merely an extension of the scalar case discussed in Section 2.5.2. Consequently, all previous discussions pertaining to the behaviour of the generalized CCF, for Cases I, II, and III, apply equally to the assessment of the three-channel filter. Given these observations, consider the three-channel extension of the single-channel α -step prediction operation given in Eq. (2.27); it is now desired to predict vector observation $[x_i(j)]_{3 \times 1}$, based on ξ previous vector observations, with the nearest such observation being $\alpha > c$ steps in the past:

$$\begin{aligned} & [h_{xy}(0 | \alpha, \beta)]_{3 \times 3} \times [x_i(j-\alpha)]_{3 \times 1} + [h_{xy}(1 | \alpha, \beta)]_{3 \times 3} \times [x_i(j-\alpha-1)]_{3 \times 1} + \dots \\ & \dots + [h_{xy}(\xi-1 | \alpha, \beta)]_{3 \times 3} \times [x_i(j-\alpha-\xi+1)]_{3 \times 1} = [x_i(j)]_{3 \times 1} \end{aligned} \quad (2.60)$$

Therefore, the observation to be predicted, may be viewed as the result of an inner product between a block transfer function vector comprised of ξ (3×3) matrix elements, and a block signal vector comprised of ξ (3×1) vector elements. In keeping with this interpretation, define the following block vectors:

$$\begin{aligned} h_{3 \times 3\xi} &= [[h_{xy}(0 | \alpha, \beta)]_{3 \times 3} \quad [h_{xy}(1 | \alpha, \beta)]_{3 \times 3} \quad \dots \quad [h_{xy}(\xi-1 | \alpha, \beta)]_{3 \times 3}] \\ x_{i:(0 \xi+1)} &= [[x_i(j-\alpha)]_{3 \times 1}^T \quad [x_i(j-\alpha-1)]_{3 \times 1}^T \quad \dots \quad [x_i(j-\alpha-\xi+1)]_{3 \times 1}^T]^T \end{aligned} \quad (2.61)$$

Then, by the same procedure as for the scalar equations, multiply both sides of Eq. (2.60) by the transpose of signal vector $x_{i:(0 \xi+1)}$, to get:

$$h_{3 \times 3\xi} \times \{ x_{i:(0 \xi+1)} \times x_{i:(0 \xi+1)}^T \} = \{ [x_i(j)]_{3 \times 1} \times x_{i:(0 \xi+1)}^T \} \quad (2.62)$$

Now, let $u=0, 1, \dots, \xi-1$ and $v=0, 1, \dots, \xi-1$ represent indices of the block elements within the matrix $x_{i:(0 \xi+1)} \times x_{i:(0 \xi+1)}^T$, such that $(u, v) = (0, 0)$ represents the location of the (3×3) block element in the upper left corner of the matrix. If the expectation of $x_{i:(0 \xi+1)} \times x_{i:(0 \xi+1)}^T$ is taken over all i , then the resulting expectation of any block element at location (u, v) within the matrix is expressed as:

$$\begin{aligned}
& \mathcal{N} \left\{ [x_i(j-\alpha-u)]_{3,1} \times [x_i(j-\alpha-v)]_{3,1}^T \right\} \\
&= \mathcal{N} \left\{ \begin{bmatrix} x_{i,\beta}(j-\alpha-u)x_{i,\beta}(j-\alpha-v) & x_{i,\beta}(j-\alpha-u)x_i(j-\alpha-v) & x_{i,\beta}(j-\alpha-u)x_{i,\beta}(j-\alpha-v) \\ x_i(j-\alpha-u)x_{i,\beta}(j-\alpha-v) & x_i(j-\alpha-u)x_i(j-\alpha-v) & x_i(j-\alpha-u)x_{i,\beta}(j-\alpha-v) \\ x_{i,\beta}(j-\alpha-u)x_{i,\beta}(j-\alpha-v) & x_{i,\beta}(j-\alpha-u)x_i(j-\alpha-v) & x_{i,\beta}(j-\alpha-u)x_{i,\beta}(j-\alpha-v) \end{bmatrix} \right\}
\end{aligned} \tag{2.63}$$

Carrying out the expectation operation on the RHS of Eq. (2.63) leaves:

$$\begin{aligned}
\mathcal{N} \left\{ [x_i(j-\alpha-u)]_{3,1} \times [x_i(j-\alpha-v)]_{3,1}^T \right\} &= \begin{bmatrix} r_{11}(v-u|0) & r_{12}(v-u|\beta) & r_{13}(v-u|2\beta) \\ r_{21}(v-u|-\beta) & r_{22}(v-u|0) & r_{23}(v-u|\beta) \\ r_{31}(v-u|-2\beta) & r_{32}(v-u|-\beta) & r_{33}(v-u|0) \end{bmatrix} \\
&= [r_{xy}(v-u|\pm \Xi \beta)]_{3,3}, \quad \Xi = 0, 1, 2
\end{aligned} \tag{2.64}$$

By using the same block-element address notation, where now $u=0$ and $v=0, I, \dots, \xi-I$, it is seen that the expectation of the vector outer product on the RHS of Eq. (2.62) is taken as:

$$\begin{aligned}
\mathcal{N} \left\{ [x_i(j-0)]_{3,1} \times [x_i(j-\alpha-v)]_{3,1}^T \right\} &= \begin{bmatrix} r_{g11}(\alpha+v|0) & r_{g12}(\alpha+v|\beta) & r_{g13}(\alpha+v|2\beta) \\ r_{g21}(\alpha+v|-\beta) & r_{g22}(\alpha+v|0) & r_{g23}(\alpha+v|\beta) \\ r_{g31}(\alpha+v|-2\beta) & r_{g32}(\alpha+v|-\beta) & r_{g33}(\alpha+v|0) \end{bmatrix} \\
&= [r_{gxy}(\alpha+v|\pm \Xi \beta)]_{3,3}, \quad \Xi = 0, 1, 2, \text{ and } \alpha > c
\end{aligned} \tag{2.65}$$

Upon forming the difference $\tau_k^{m=v-u}$, it is seen that the final result of taking expectations on both sides of Eq. (2.62) then becomes:

$$\begin{aligned}
& \left[\begin{array}{ccc} [h_{xy}(0 | \alpha, \beta)]_{3 \times 3} & [h_{xy}(1 | \alpha, \beta)]_{3 \times 3} & \dots [h_{xy}(\xi-1 | \alpha, \beta)]_{3 \times 3} \end{array} \right] \times \\
& \left[\begin{array}{ccc} [r_{xy}(0 | \pm \Xi \beta)]_{3 \times 3} & [r_{xy}(1 | \pm \Xi \beta)]_{3 \times 3} & \dots [r_{xy}(\xi-1 | \pm \Xi \beta)]_{3 \times 3} \\ [r_{xy}(-1 | \pm \Xi \beta)]_{3 \times 3} & [r_{xy}(0 | \pm \Xi \beta)]_{3 \times 3} & \dots \vdots \\ \vdots & \vdots & \ddots \vdots \\ [r_{xy}(-\xi+1 | \pm \Xi \beta)]_{3 \times 3} & \dots & \dots [r_{xy}(0 | \pm \Xi \beta)]_{3 \times 3} \end{array} \right] \\
& = \left[[r_{gxy}(\alpha | \pm \Xi \beta)]_{3 \times 3} [r_{gxy}(\alpha+1 | \pm \Xi \beta)]_{3 \times 3} \dots [r_{gxy}(\alpha+\xi-1 | \pm \Xi \beta)]_{3 \times 3} \right]
\end{aligned}$$

where $\Xi = 0, 1, 2$, and $\alpha > c$

$$\therefore h_{3 \times 3\xi} \times R_{3\xi \times 3\xi} = r_{3 \times 3\xi} \tag{2.66}$$

Hence, the steps occurring between Eq. (2.62) and Eq. (2.66) may be summarized as:

$$\begin{aligned}
h_{3 \times 3\xi} \times \mathcal{Z} \left\{ x_{i(3\xi+1)} \times x_{i(3\xi+1)}^T \right\} &= \mathcal{Z} \left\{ [x_i(j)]_{3 \times 1} \times x_{i(3\xi+1)}^T \right\} \\
h_{3 \times 3\xi} \times R_{3\xi \times 3\xi} &= r_{3 \times 3\xi}
\end{aligned} \tag{2.67}$$

From inspection of the scalar elements occurring within the preceding operations, it is easy to see that each block element within $R_{j\xi, j\xi}$ and $r_{j, j\xi}$, retains information regarding the regional inter-relationships which exist between the rows of the image, for chosen α and β . Since the block vector of the impulse response is achieved via solution of Eq. (2.67), it follows that the filter itself must also incorporate this same information.

2.6.3 Three-Channel Wiener Filter: Frequency-Domain Transfer Function

The form of Eq. (2.66) is essentially a block element extension of the scalar element version presented in Eq. (2.30). Consequently, by following the same procedure as for Eq. (2.36) and Eq. (2.37), it is possible to show that the three-channel version of the Wiener-Hopf equations become, for $\alpha > c$ and $\kappa = 0, 1, \dots, \xi-1$:

$$\begin{aligned}
\sum_{b=0}^{\xi-1} \begin{bmatrix} h_{11}(b | \alpha, \beta) & h_{12}(b | \alpha, \beta) & h_{13}(b | \alpha, \beta) \\ h_{21}(b | \alpha, \beta) & h_{22}(b | \alpha, \beta) & h_{23}(b | \alpha, \beta) \\ h_{31}(b | \alpha, \beta) & h_{32}(b | \alpha, \beta) & h_{33}(b | \alpha, \beta) \end{bmatrix} & \times \begin{bmatrix} r_{11}(\kappa-b | 0) & r_{12}(\kappa-b | \beta) & r_{13}(\kappa-b | 2\beta) \\ r_{21}(\kappa-b | -\beta) & r_{22}(\kappa-b | 0) & r_{23}(\kappa-b | \beta) \\ r_{31}(\kappa-b | -2\beta) & r_{32}(\kappa-b | -\beta) & r_{33}(\kappa-b | 0) \end{bmatrix} \\
& = \begin{bmatrix} r_{g11}(\kappa+\alpha | 0) & r_{g12}(\kappa+\alpha | \beta) & r_{g13}(\kappa+\alpha | 2\beta) \\ r_{g21}(\kappa+\alpha | -\beta) & r_{g22}(\kappa+\alpha | 0) & r_{g23}(\kappa+\alpha | \beta) \\ r_{g31}(\kappa+\alpha | -2\beta) & r_{g32}(\kappa+\alpha | -\beta) & r_{g33}(\kappa+\alpha | 0) \end{bmatrix}
\end{aligned} \tag{2.68}$$

The principal focus of this discussion, will be those filtering operations which are required in order to produce the row process estimate occurring at the Channel 2 output; however, note that all discussions pertaining to Channel 2 may also be applied to Channels 1 and 3 in a similar fashion. Therefore, by extracting only the Channel 2 output from the convolution of Eq. (2.68), it is possible to obtain a set of simultaneous equations, defined as:

$$\begin{aligned}
\sum_{b=0}^{\xi-1} [h_{21}(b | \alpha, \beta)r_{11}(\kappa-b | 0) + h_{22}(b | \alpha, \beta)r_{21}(\kappa-b | -\beta) + h_{23}(b | \alpha, \beta)r_{31}(\kappa-b | -2\beta)] \\
& = r_{g21}(\kappa+\alpha | -\beta) \\
\sum_{b=0}^{\xi-1} [h_{21}(b | \alpha, \beta)r_{12}(\kappa-b | \beta) + h_{22}(b | \alpha, \beta)r_{22}(\kappa-b | 0) + h_{23}(b | \alpha, \beta)r_{32}(\kappa-b | -\beta)] \\
& = r_{g22}(\kappa+\alpha | 0) \\
\sum_{b=0}^{\xi-1} [h_{21}(b | \alpha, \beta)r_{13}(\kappa-b | 2\beta) + h_{22}(b | \alpha, \beta)r_{23}(\kappa-b | \beta) + h_{23}(b | \alpha, \beta)r_{33}(\kappa-b | 0)] \\
& = r_{g23}(\kappa+\alpha | \beta)
\end{aligned} \tag{2.69}$$

where $\kappa = 0, 1, \dots, \xi-1$, and $\alpha > c$. Upon multiplying both sides by $e^{j\kappa}$ and then taking summations over κ , it will be seen that this system reduces to the following frequency-domain matrix operation:

$$\left\{ \begin{bmatrix} G_{11}(f|0) & G_{21}(f|-\beta) & G_{31}(f|-2\beta) \\ G_{12}(f|\beta) & G_{22}(f|0) & G_{32}(f|-\beta) \\ G_{13}(f|2\beta) & G_{23}(f|\beta) & G_{33}(f|0) \end{bmatrix} + [N_{1j}(f|\pm\Xi\beta)]_{3 \times 3} \right\} \times \begin{bmatrix} H_{21}(f|\alpha, \beta) \\ H_{22}(f|\alpha, \beta) \\ H_{23}(f|\alpha, \beta) \end{bmatrix} = \begin{bmatrix} G_{21}(f|\alpha, -\beta) \\ G_{22}(f|\alpha, 0) \\ G_{23}(f|\alpha, \beta) \end{bmatrix} \quad (2.70)$$

Here, $[N_{1j}(f|\pm\Xi\beta)]_{3 \times 3}$ is a 3×3 matrix of noise terms which will be investigated in Section 2.6.4. Note also, that the auto- and cross-spectral estimates of the signal components on the LHS, will differ from any corresponding estimates occurring on the RHS. By momentarily ignoring the noise term and focusing only upon the signal spectra, from Eq. (2.70) it is apparent that, in general, $H_{21}(f|\alpha, \beta) \neq H_{22}(f|\alpha, \beta) \neq H_{23}(f|\alpha, \beta)$. That is, the form of the equation implies that there exists no restriction which forces the three terms to be equal for any given f . Moreover, given the fact that the LHS is dependent upon β , as well as the fact that the RHS is dependent upon both α and β , it must follow that *the magnitude response of the three filters will be affected by these terms, if the CCF obeys either Case II or Case III from Section 2.4.3. This implies that the predictable components of a vector bandpass process will change due to any variations in these parameters; a direct extension of the situation for the scalar filter. The presence of the noise terms will also affect the filter performance, yet, as was shown in Section 2.5.5, the influence of noise will be much less severe than for the scalar case.*

It is now desirable to investigate those relationships within the vector filter structure which may influence its noise-suppression capability. However, a direct analytical solution to Eq. (2.70) will not be attempted because it would yield an unwieldy result, involving terms of such ubiquity as to preclude any intuitive analysis. A better approach towards inspecting the role of the noise terms would be to summarize Eq. (2.70) as follows:

$$\{ [G_{xy}(f | \pm \Xi \beta)]_{3 \times 3} + [N_{xy}(f | \Xi \beta)]_{3 \times 3} \} \times [H_{xy}(f | \alpha, \beta)]_{3 \times 1} = [G_{xy}(f | \alpha, \pm \Gamma \beta)]_{3 \times 1}$$

$$\Xi = 0, 1, 2; \quad \Gamma = 0, 1$$
(2.71)

The form of this equation implies that its solution has been subjected to the following constraint:

$$[N_{xy}(f | \pm \Xi \beta)]_{3 \times 3} \times [H(f | \alpha, \beta)]_{3 \times 1} = O_{3 \times 1}$$

$$\Xi = 0, 1, 2$$
(2.72)

where $O_{j \times 1}$ is a 3×1 vector, the elements of which are all zero. The ramifications which this constraint will hold, regarding the noise suppression performance of the three-channel vector Wiener filter, will now be studied.

2.6.4 Achieving Optimum Noise Suppression with the Three-Channel Wiener Filter

In Eq. (2.66), it is to be understood that the scalar ACF coefficients which occur within the block elements on the LHS must contain a noise term, regardless of the value chosen for β . In addition, if $\theta < \beta \leq c$, then the coefficients from the CCF proper will also contain noise terms. Therefore, it follows that the scalar auto-correlation coefficients in Eq. (2.66) *must* contain a noise term, and the scalar cross-correlation coefficients *may* incorporate noise components. For the matrices which occur on the LHS of Eq. (2.70) and Eq. (2.71), this implies that each ij 'th, $i=j$, signal component *must* have a corresponding non-zero noise component in $[N_{xy}(f | \pm \Xi \beta)]_{j,j}$, and that each ij 'th, $i \neq j$, signal component *may* have an associated non-zero noise term in $[N_{xy}(f | \pm \Xi \beta)]_{j,j}$. Hence, the configuration of terms within $[N_{xy}(f | \pm \Xi \beta)]_{j,j}$ will be directly dependent upon the value which has been chosen for β in relation to the value which exists for c . In fact, for a three-channel filter, there are three possible forms which may be taken by $[N_{xy}(f | \pm \Xi \beta)]_{j,j}$:

$$\begin{bmatrix} N_{11}(f|0) & N_{21}(f|-\beta) & N_{31}(f|-2\beta) \\ N_{12}(f|\beta) & N_{22}(f|0) & N_{32}(f|-\beta) \\ N_{13}(f|2\beta) & N_{23}(f|\beta) & N_{33}(f|0) \end{bmatrix} \times \begin{bmatrix} H_{21}(f|\alpha, \beta) \\ H_{22}(f|\alpha, \beta) \\ H_{23}(f|\alpha, \beta) \end{bmatrix} = \begin{bmatrix} 0 \\ 0 \\ 0 \end{bmatrix} \quad \text{for } \beta \leq \left\lfloor \frac{c}{2} \right\rfloor \quad (2.73)$$

$$\begin{bmatrix} N_{11}(f|0) & N_{21}(f|-\beta) & 0 \\ N_{12}(f|\beta) & N_{22}(f|0) & N_{32}(f|-\beta) \\ 0 & N_{23}(f|\beta) & N_{33}(f|0) \end{bmatrix} \times \begin{bmatrix} H_{21}(f|\alpha, \beta) \\ H_{22}(f|\alpha, \beta) \\ H_{23}(f|\alpha, \beta) \end{bmatrix} = \begin{bmatrix} 0 \\ 0 \\ 0 \end{bmatrix} \quad \text{for } \left\lfloor \frac{c}{2} \right\rfloor < \beta \leq c \quad (2.74)$$

$$\begin{bmatrix} N_{11}(f|0) & 0 & 0 \\ 0 & N_{22}(f|0) & 0 \\ 0 & 0 & N_{33}(f|0) \end{bmatrix} \times \begin{bmatrix} H_{21}(f|\alpha, \beta) \\ H_{22}(f|\alpha, \beta) \\ H_{23}(f|\alpha, \beta) \end{bmatrix} = \begin{bmatrix} 0 \\ 0 \\ 0 \end{bmatrix} \quad \text{for } c < \beta \quad (2.75)$$

where $\lfloor \cdot \rfloor$ denotes the integer floor function. From these relationships, it follows that optimum noise suppression will be obtained from the three-channel filter for the case in which $\beta > c$, defined in Eq. (2.75). This can be seen by considering that if the off-diagonal noise spectra are not present, then the only solution for transfer function $[H_{ij}(f|\alpha, \beta)]_{i,j}$ which satisfies Eq. (2.72), is the trivial solution. However, for the two cases corresponding to $\beta \leq c$, in Eq. (2.73) and Eq. (2.74), the existence of the off-diagonal noise terms implies admittance of other solutions. Hence, the off-diagonal terms, if present, will permit an unconstrained solution to the equation, which does not necessarily imply that the transfer function have zero-magnitude frequency response. The intermediate case, in Eq. (2.74), does impose a greater degree of constraint in comparison to Eq. (2.73), but still does not force a trivial solution. Alternatively, the existence of noise terms only on the main diagonal, forces a constrained solution in which the frequency response must be zero.

These conclusions of course, are only truly valid for the case in which the signal component is absent from Eq. (2.71). It is obvious that when the desired signal component is

present, the transfer function must also satisfy the constraints imposed by this matrix as well; therefore, even for the trivial case of Eq. (2.75), the transfer function can never be zero for all f . However, the above argument does make it clear that if the noise terms are present only on the main diagonal, then the filter will achieve noise suppression which is superior in comparison to that which would be achieved via the alternative configurations for $[N_o(f \pm \beta)]_{r,r}$. Based on this analysis, it can be concluded that all filtering applications should be performed with a value for β which is greater than the value observed for c .

2.7 Vector Filtering Technique for Reduction of Coherent Noise

2.7.1 Overview

Numerical derivation of a three-channel Wiener filter is begun by computing an estimated two-dimensional ACF, from an $N_r \times N_r$ image which satisfies the signal and noise model defined by Eq. (2.1). By close inspection of this ACF, it will be possible to make inferences regarding the approximate extent of correlation within the noise process, thereby permitting an estimate of the value for c . Then, after choosing an appropriate value for β such that $\beta > c$, numerical estimates of the one-dimensional row ACF and CCF may be extracted. Upon determining an appropriate value for α such that $\alpha > c$, the auto- and cross-correlation coefficients may then be arranged into the form prescribed by Eq. (2.66). Solution of this block matrix equation will yield the numerical estimates of the matrix impulse response coefficients, which are defined in Eq. (2.56). The scalar impulse response function coefficient sets, h_{21} , h_{22} , and h_{23} , may then be extracted; these are required in order to produce the Channel 2 estimate, g_r , of g_r . The final result will be three scalar filters, each of which incorporates information regarding the inter-relationships between all three channels, as provided by the auto- and cross-correlation data.

The filtering operation then involves the convolution of each impulse response with its respective row process component, found within each row triplet process of the image. By operating on each row triplet, an estimate of the signal process is generated for each i 'th row and stored in a *separate* set. That is, for the image which is being operated on, the row process, x_i , existing in row i , must *not* be replaced by its estimate, \hat{x}_i ; such a practise would affect the eventual estimation of row $i+\beta$, which assumes that all three filter inputs are from noisy rows of the image. Rather, the Channel 2 estimates are used to build a new and separate image, row by row, as the filter operates on successive row triplets from the noisy image.

This filtering operation will achieve effective noise suppression in the row dimension of the image; however, upon completion of the row operations, noise components will continue to exist in the column dimension. Consequently, a new set of three-channel impulse response functions are then derived for the columns, based on the initial two-dimensional ACF which was estimated from the unfiltered image. This is achieved by setting $\tau_r=0$ in Eq. (2.10) and Eq. (2.11), in order to derive the one-dimensional ACF information for the columns; similarly, setting $\tau_r=\pm\beta$ and $\pm 2\beta$ in these equations yields the appropriate CCF information. The filtering operation is then applied to the columns in the same manner as for the rows.

The three-channel configuration of the operator, in combination with the fact that the rows and columns are filtered independently, will give rise to some potential sources of inaccuracy. These need to be taken into consideration if the filter is to perform its task properly. Such specialized attributes of the vector filtering technique will now be discussed.

2.7.2 Minimizing Phase Distortions in the Row and Column Estimates

The fact that the three filters have not been constrained to produce a distortionless response, requires some consideration as to how phase distortions in the output may be cancelled. Given a general situation, in which some filter is known to produce a phase-distorted version of its input, the sequence being operated on is typically filtered first in the forward direction; then, the output sequence from this operation is reversed and passed through the filter again. Hence, the data sequence is filtered in both directions, so that any phase distortion introduced by the forward filtering pass is reversed and cancelled during the backward pass. This technique, which has been employed in [31], results in zero phase distortion. Since it is possible that the three Wiener filters will each introduce phase distortions into the output signal, it would be desirable to apply this forward and backwards approach when filtering the image. However, a three-channel configuration presents complications. To understand this, consider a situation in which three row processes, $x_{r,g}$, x_r , and $x_{r,b}$, occur such that in terms of relative phase, $x_{r,g}$ leads x_r and $x_{r,b}$ trails x_r ; let these three rows now act as inputs to the Channels 1, 2 and 3 respectively. Assume also, that this relationship is typical for predictable components existing in all rows of the image. Then, after the filters have been derived, h_{21} will incorporate a phase *delay* which is necessary in order that the Channel 1 estimate of the Channel 2 signal component, may be brought into phase with the estimate which actually occurs from the Channel 2 filter. Similarly, h_{23} will incorporate a phase *advance* which is needed in order to bring the Channel 3 estimate of the Channel 2 process into phase with the Channel 2 estimate. Now, in addition to these *desired and necessary* phase adjustments, there will also be undesired phase distortions produced by the generally non-linear phase response within all three filters. Recalling that the three outputs are summed in order to produce the Channel 2 estimate, it may appear that prior to such summation, unwanted phase distortions could be eliminated by reversing each output sequence and then passing it through its respective filter in the backwards direction. While it is true that such distortions would be

cancelled, this operation would also cancel the Channel 1 phase delay and the Channel 3 phase advance, which must be retained in order that the three output estimates be in phase for the summing operation. Therefore, if forward and reverse filtering are performed in this manner, then the final summation process will involve three out-of-phase signals, which will considerably distort the estimated signal component of row i .

As an alternative, it might also appear that immediate summation of the three outputs, followed by reverse filtering of this sum by h_{22} , would solve the distortion problem. However, the form of Eq. (2.70) has implied that the three transfer functions are not constrained to be identical. This suggests that each of these transfer functions complement each other during the addition operation. Hence, although the summation of their three outputs is an approximation to the desired signal, there exists no guarantee that each of the individual outputs is a complete facsimile of the process being predicted. Therefore, reverse filtering with the Channel 2 filter only, may induce distortions of a different nature.

Given these considerations, it is now possible to discuss a feasible approach to reversing phase distortions in a three-channel filtering application. In this procedure, the entire image is filtered row-wise to produce a set of forward-filtered estimates of the row signal process. From the above discussion, it is known that the resulting image will also incorporate unwanted phase distortions induced by the nonlinear phase response of the filters. By retaining the same three-channel configuration of filter impulse responses, and then flipping the row-filtered image from left to right, it is seen that the data sequence in each row is now reversed with respect to the filter inputs. However, as a result of this flip, the forward-filtered signal estimate, $\hat{g}_{i,j}$, now trails process estimate g_i in phase, and process estimate $\hat{g}_{i,j}$ leads estimate g_i . This is exactly opposite to that which the filter anticipates. Therefore, in order to accommodate the filter, the image is then flipped from top to bottom; careful consideration will verify that this procedure produces a phase relationship between rows, which obeys the input assumptions of the filter. Reversal of phase

distortions is then possible, by filtering all row triplets occurring within this vertically and horizontally flipped, forward-filtered image of row process estimates. Following this, the column filtering operations are performed in identical fashion.

2.7.3 Selection of CCF and ACF Information for Vector Filtering in the Columns

Since filtering is performed in the rows first, it is important to anticipate any influences which this may have upon the performance of the three-channel filter for the columns. In particular, the remnant noise components which are inevitably passed by the three-channel row operation may significantly affect the column operations which follow. To understand this, consider the image which has been produced by filtering the rows in only *one* direction, in the presence of Case II correlation data. From this image, consider any three row estimates, say \hat{g}_i , $\hat{g}_{i,\beta}$, and $\hat{g}_{i,2\beta}$, and for this particular example, assume $\beta=c=1$ and $c=1$. It is already known that each estimate has been obtained from a respective row triplet of the noisy image, and that the rows within each triplet have been separated by a distance of β which is greater than the extent of noise correlation. However, Eq. (2.54) has shown that two of the noisy rows used in the estimate of \hat{g}_i have also been used to estimate $\hat{g}_{i,\beta}$, and one of the rows used in estimating both \hat{g}_i and $\hat{g}_{i,\beta}$ has also been used in estimating $\hat{g}_{i,2\beta}$.

The three-channel row filtering operation relies on the summation of out-of-phase, uncorrelated noise components, in order to suppress noise existing in the passband. While this passband noise is suppressed by the method, it is certainly not eliminated, and some remnants will continue to exist in the estimates, \hat{g}_i . Furthermore, the overlap of the x_i between row triplets which are used in the filtering operation, guarantees that all three row estimates must contain a certain degree of common information pertaining to the remnant noise; this is the ultimate result of the relationships which are described in Eq. (2.54). It therefore follows that the remnant noise components in \hat{g}_i must now be correlated with those remaining in both $\hat{g}_{i,\beta}$ and $\hat{g}_{i,2\beta}$. This means

that after filtering in one direction along the rows, the noise in the column dimension of the row-filtered image will be correlated up to $c = 2\beta + J$ within the column versions of Eq. (2.12) and Eq. (2.13). Recall, that prior to filtering, it was only correlated to $c = \beta - J$; hence, the extent of noise correlation in the columns has been increased due to the row filtering. Further to this, assume also that $\alpha = \beta$ for the row filtering operation, performed only in the forward direction, and that a new two-dimensional ACF is then computed in support of column filter derivation, *after* row filtering has been done. For this example, it is easy to see that the column derivation will require a prediction gap of $\alpha > 2\beta + J$, in order to separate the noise components from the signal process components which exist in the column correlation data. If the correlation functions for the columns are also exponentially-damped, then it is obvious that this increased prediction gap will mean that the column estimates are biased in comparison to the row estimates; this will distort the original relationships which existed between the rows and columns. As an additional consideration, it is easy to conclude that the extent of noise correlation in the columns will further increase, if the rows are also reverse-filtered prior to computing column correlation data.

However, if the column filters are derived from correlation data obtained *prior* to row filtering, then it is possible to maintain a prediction gap which is equivalent to that for the rows, and the filters will still pass only those noise frequencies which are common to the signal process. In this situation, the passbands of the column filters will be unaltered by the increased correlation of the noise. It should also be noted, that the row filtering operation must further correlate the remnant noise components along the row dimension as well. For filtering in the columns, this means that the extent of cross-column coherence between remnant noise components will be greater than it had originally been between rows. Further to this, when the signal is bandpass, the same value of β must be used in the columns as was used for the rows. This implies that the passband noise suppression advantage offered by a three-channel operator may not be as significant for operations in the column dimension.

2.8 Summary

Based on the mathematical considerations presented in the preceding Sections, it is possible to conclude that a vector filtering technique which suppresses broad-band correlated noise is indeed achievable. There are, however, compromises associated with the technique under certain circumstances. This is due to the fact that if the two-dimensional ACF is exponentially-damped, then only some components of the stochastic process are predictable; consequently, the original process can never be recovered in its entirety. However, in situations of very low SNR, a recovery which favours some frequency components over others, may be preferable to the noisy version. Having now established a mathematical basis for the vector filtering technique, the remaining Chapters will examine results which have been obtained from simulated data, as well as from stochastic processes existing in noisy SAR images.

CHAPTER THREE

RESULTS FROM NUMERICAL SIMULATIONS INVOLVING CASE I CORRELATION DATA

3.1 Introduction

To examine the effectiveness of the vector filtering technique under controlled conditions, and as a means of verifying some of the mathematical observations made previously, several investigations were conducted using simulated data. These have been made possible through development of computer algorithms which incorporate the mathematical relationships defined in Chapter Two. Such algorithms were constructed from subroutines available in the MATLAB software package [31] & [32], and are discussed in Appendix II. The simulated images which were analyzed, consisted of signal-plus-noise composites incorporating 1024×1024 pixels. Results of test filtering operations have been presented in the form of recovered images, and one-dimensional FFT analysis of the image row and column components. These have also been supplemented by the development of power transfer functions, which indicate how the power within row and column components has been redistributed as a result of the filtering operation. The present Chapter will deal with analysis of stationary processes having one-dimensional row and column correlation functions which satisfy the Case I criteria discussed in Section 2.4.3; subsequent Chapters will provide an analysis of filter performance for Case II data.

Spectral analysis was achieved via a (1024×1024) -point FFT, which yielded a two-dimensional complex-valued spectrum for the process contained within each image. Each element within this matrix spectrum was then multiplied by its complex conjugate in order to produce a two-dimensional power spectrum. In any typical mathematical problem involving the joint

occurrence of two variables, the marginal values associated with a variable in one dimension may be obtained by integrating along the dimension of the other. Consequently, in order to obtain a 1024-point one-dimensional power spectrum for the row component, the two-dimensional power spectrum was summed along the column component. Following this, the frequency powers within the row spectrum were normalized by one of the two procedures described below, the choice of which depended upon the intended manner of presentation. This entire procedure was then followed in an identical fashion when deriving power spectra for the column components. Another important point which should be made, is that the frequency axis for all spectral plots to be presented in this thesis, has been labelled with decimal multiples of π . Therefore, while all FFT's have been computed for digital frequencies $-\pi < f \leq \pi$, the corresponding x-axis frequency range is labelled as $-1 < f \leq 1$.

The normalization of power spectra will be performed for all FFT analysis to be undertaken in this report. The reason for this practise stems from the discussion regarding Eq. (2.40); there, it was observed that the filter frequency response must always have a magnitude of less than unity, in the presence of noise. While this equation refers specifically to the scalar version of the filter, such characteristics also extend to the vector version. Therefore, a gain factor of less than unity implies that even if all signal frequencies have been recovered in the filtered image, each frequency value must have a power level which is less than that of its respective component in the original image. This means that direct comparisons of spectra, based on absolute magnitudes of power, are not reliable.

Therefore, where spectral plots have been presented for purposes of visual comparison, each will have been scaled by the inverse of its respective maximum power. This restricts the power of any frequency point within the normalized spectrum, to a maximum value of unity. The purpose of such presentation is to provide qualitative evidence of overall change in spectral shape or suppression of noise, hence, direct comparisons based on magnitude are not emphasized.

Complementary to this, direct numerical comparisons between filtered and unfiltered row or column power spectra, have been facilitated by computation of a power transfer function. In order to achieve this, it was necessary to normalize the spectra via an alternate procedure, defined by the following relationship found in [33]:

$$P_N(f) = \frac{P(f)}{\sum_{\{f|1-f \leq 1\}} P(f)} \quad (3.1)$$

Here, $P_N(f)$ denotes the normalized power at the specified frequency f . When comparing row spectra, say, between an unfiltered and a filtered image, this normalization procedure is used to scale the spectra such that the *total sum* of power within each spectrum assumes a value of unity. Since these two spectrums now contain the same total power, a numerical power transfer function will force an emphasis upon the manner in which power has been redistributed during the filtering operation which maps the former spectrum into the latter. In fact, any filter which reduces power in the noise frequencies and redistributes it in order to boost signal power, must yield an improved SNR within the image.

The capacity of an operator to perform in this manner, can be assessed by means of a \log_{10} -scaled power transfer function, defined as:

$$T_p(f) = 10 \log_{10} \left\{ \frac{P_{N\text{OUT}}(f)}{P_{N\text{IN}}(f)} \right\} \quad (3.2)$$

where $P_{N\text{IN}}(f)$ represents the normalized power spectra, via Eq. (3.1), of either the row or column component which served as input to the filtering operation; $P_{N\text{OUT}}(f)$ represents the normalized power spectra, also via Eq. (3.1), for the respective component of the output image which resulted. Since both the input spectra and the output spectra incorporate an identical amount of energy, it follows that if $T_p(f)$ is *not* identically zero for all f , then it *must* incorporate some combination of *both* positive and negative values. Consequently, frequencies which experienced

a loss of power during filtering will yield a negative value for $T_r(\theta)$, whereas those which experienced power gain at output will produce a positive value; obviously, frequencies experiencing no change will produce a value of zero.

3.2 Characteristics of Simulated Data Sets

To facilitate these investigations, two image processes comprised of 1024×1024 pixels each, were generated from the following two-dimensional sinusoidal components:

$$\begin{aligned}
 s1 &= \cos\left(\frac{2\pi}{40}i + \frac{2\pi}{30}j\right) \\
 s2 &= \cos\left(\frac{2\pi}{90}i + \frac{2\pi}{100}j\right) \\
 s3 &= \cos\left(\frac{2\pi}{15}i + \frac{2\pi}{10}j\right)
 \end{aligned} \tag{3.3}$$

where $i=1,2,\dots,1024$, and $j=1,2,\dots,1024$. One such process was a zero-mean wavefield which consisted only of $s1$ from Eq. (3.3). The other was a three-component, zero-mean wavefield comprised of all three sinusoids; in this case however, the 1024×1024 image component $s3$ was flipped left-to-right, prior to superposition onto the 1024×1024 composite formed by addition of components $s1$ and $s2$. From the form of the signal components, defined by Eq. (3.3), it should be apparent that the resulting wavefields will produce Case I correlation data, when a two-dimensional ACF is estimated from the simulated images. In addition to this, a 1024×1024 correlated, zero-mean noise field was generated and added to both the one-component wavefield and the three-component composite. This noise field incorporated a spatial correlation extent which would be equivalent to a value of $c=l$ in Eq. (2.11). It was produced by initially generating a 1025×1025 uncorrelated noise field, $u_n(i,j)$ say, from zero-mean normally-distributed random

numbers. Each (i,j) 'th point within correlated noise field $n(i,j)$, was then created via the following operation:

$$n(i,j) = n_{nc}(i,j) + n_{nc}(i+1,j) + n_{nc}(i,j+1) + n_{nc}(i+1,j+1) \quad (3.4)$$

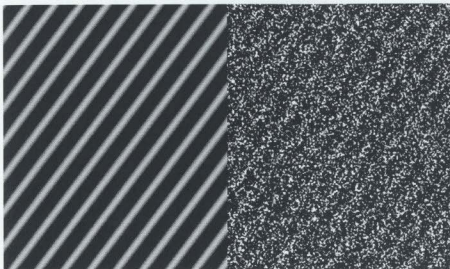
Prior to superposition onto each of the two image processes, the power level of the correlated noise was scaled such that, within each signal-plus-noise process, the resulting SNR was -12 dB.

These combinations are presented in Figure 3.1, where the left half of Figure 3.1(a) shows the one-component noise-free wavefield, while the right half consists of the corresponding wavefield-plus-noise combination. Similarly, the left portion of Figure 3.1(b) displays the three-component noise-free process, with the signal-plus-noise composite shown on the right. Note here, that the grey-scale mapping used to produce the images in Figure 3.1, performs half-wave rectification. That is, all negative-valued amplitudes of the zero-mean processes are clipped at zero; this form of presentation will be used for all images which are displayed in this report.

The manner in which the noise and signal components of these processes interact within the correlation information is shown in Figure 3.2, which displays the one-dimensional ACF characteristics of the row and column components from each image. The contribution from the noise portion of the process presents itself as a prominent, tapered spike, which clearly shows that the noise is also correlated at non-zero lags $\tau = \pm l$. However, it is seen that the noise has no influence upon the autocorrelation information for values of $|\tau| > l$.

Figure 3.3 presents the results of a 1024-point normalized FFT analysis, performed on the row and column components of the noise-free wavefields. Complementary to this, Figure 3.4 shows the results from an identical analysis performed on each of the signal-plus-noise processes. Here, it is seen that the noise component produces a spectrum which is obviously tapered, a characteristic which is typical of broad-band noise processes; note also, that tapering windows have *not* been used in the computation of these spectra. Figures 3.3 and 3.4 will serve as a

(a) One-Component Wavefield with Noise



(b) Three-Component Wavefield with Noise

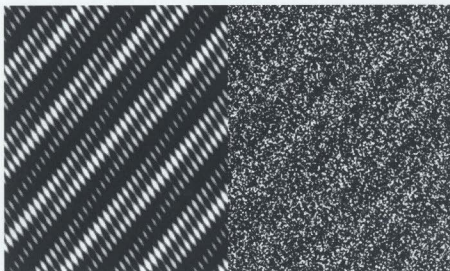


Figure 3.1: Simulated noise-free wavefields, and wavefield-plus-noise composites with -12dB SNR.

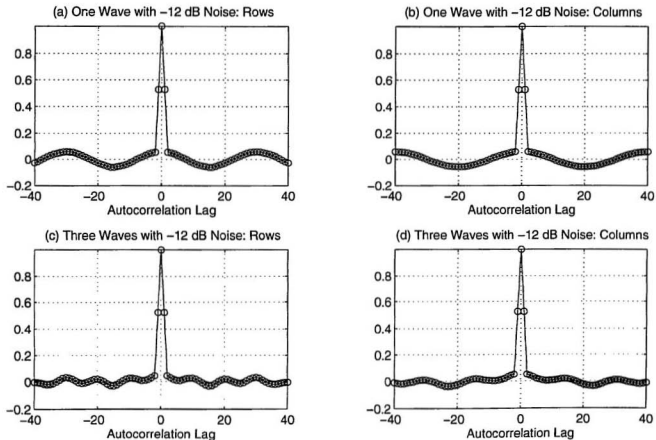


Figure 3.2: One-dimensional autocorrelation functions, for row and column components of the signal-plus-noise processes shown in Figure 3.1.

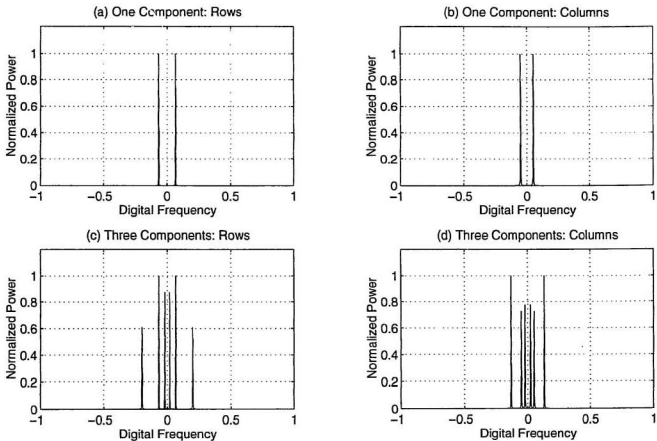


Figure 3.3: 1024-point FFT's, showing relative magnitudes of normalized power within row and column components of the noise-free wavefields in Figure 3.1.

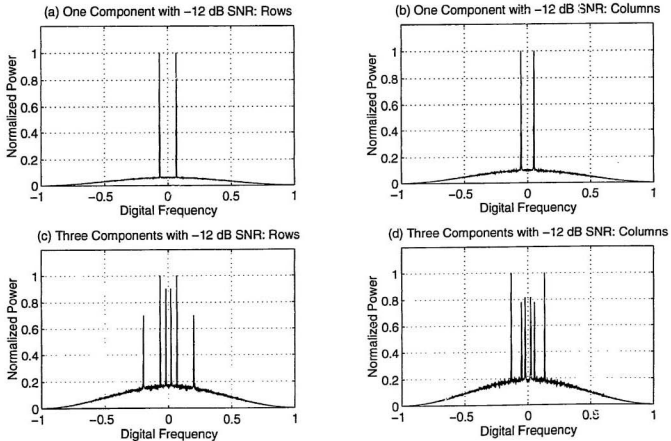


Figure 3.4: 1024-point FFT's, showing relative magnitudes of normalized power within row and column components of the signal plus-noise composite processes in Figure 3.1.

convenient reference, when evaluating the signal-recovery ability of the three-channel Wiener filter in Sections 3.3 and 3.4.

3.3 Determination of Optimum Operational Parameters for Filtering Technique

3.3.1 Overview

This Section will provide numerical verification of some operational attributes, that were previously identified as imparting superior performance to the filtering technique which has been proposed. Such attributes will be investigated through filtering operations performed on the three-component signal-plus-noise process. The tests which will be discussed, were performed in order to substantiate the following assertions which emerged from the discussions within Chapter Two:

- (1) the noise-suppression advantage offered by the three-channel operator, when compared to the single-channel version.
- (2) the noise-suppression advantage of the three-channel operator when derived with $\alpha > c$, as compared with the same operator for $\theta < \alpha \leq c$.
- (3) the noise-suppression advantage of the three-channel operator when derived in conjunction with $\beta > c$, as compared with the same operator for $\theta < \beta \leq c$.
- (4) the noise-suppression advantage of deriving row and column vector operators by using correlation data from the unfiltered image, when compared to deriving the column operator using data from the row-filtered image.

In preparation for these investigations, a standard reference image was recovered from the noisy three-component wavefield. This was obtained by using row and column operators which were derived based on the optimal filtering strategies recommended by the discussions of Chapter Two. Specifically, this involved deriving a three-channel vector operator which used row

and column correlation data from the unfiltered image, and which incorporated parametric values of $\beta > c$ and $\alpha > c$; this will subsequently be referred to as the standard-attribute operator.

The investigation process consisted of generating a test image, which was then compared with the standard reference obtained via the standard-attribute operator. When generating each test image, only the filter attribute under investigation was changed; the remaining operational attributes were identical to those used to establish the reference image. Therefore, when assessing the superiority which a three-channel operator could have over a one-channel version, only the number of channels was adjusted. Similarly, when assessing the influence of adjustments to β or α , or the effect of using column correlation data obtained from the row-filtered image, only one of these attributes was changed in order that its respective test image could be generated. Note also, that although correlation data have been displayed in a normalized format, only non-normalized data were used in filter derivation. Furthermore, correlation data for the filtering operations were obtained based upon averages taken over the entire image, as discussed in Chapter Two. In all cases, filtering was performed first in the row dimension; this was then followed by equivalent operations on the columns.

For all four tests, an operator length of $\xi=20$ has been used; it will eventually be seen that this is a considerably smaller value than was used for other filtering operations, to be described in the next Section and in subsequent Chapters. This comparatively shorter length was selected because it imposes a condition of marginal performance for the operator; hence, with small ξ , the filters will pass a detectable amount of noise. However, for large ξ , overall noise suppression would be so severe, regardless of parametric adjustments, that relative differences between images will not be detected visually. Therefore, a value of $\xi=20$ makes it possible to visually assess changes in noise suppression efficiency which are imposed by adjustments to the filter parameters. Evaluations will be made possible via the presentation of recovered images and normalized FFT analysis, including power transfer functions. Within the context of Eq. (3.2), note

that the power transfer function derivation will treat the spectrum of the test image as $P_{NIN}(f)$, whereas the power spectrum of the reference image will be assigned to $P_{NOUT}(f)$.

Furthermore, for both the standard image and those test comparisons which have been generated, it will be seen that a filter order of $\xi=20$ does not permit complete recovery of the three-component wavefield. This is partly due to the fact that one cycle of the longest wavelength in the column dimension incorporates 90 pixel elements, while one cycle in the row dimension spans 100 pixels. Therefore, in comparison to the longest wavelength on which it operates, the filter is too short and contains insufficient information for making accurate predictions at the SNR which exists in the image. However, since this deficiency is common to both the reference image and the test images, relative comparisons are certainly permissible. Also, since it is known that the filters are functioning only nominally in recovering the wavefield, trends which are observed for the wavefield frequencies will not be of interest during these comparisons. Consequently, this Section will focus only on test results as they affect the noise portion of the spectrum. The results of comparisons between the reference and test images will now be discussed.

3.3.2 Noise-Suppression Advantage of a Three-Channel Filter Over the One-Channel Version

Figure 3.5(a) shows the reference wavefield which was recovered using the standard filtering parameters discussed previously. By comparison, the test image which was recovered via a one-channel operator, and which is shown in Figure 3.5(b), indicates that the three-channel operator yields a superior result. In fact, it is easily seen that the structure produced by the three-channel operator, albeit incomplete, does bear a much stronger resemblance to the original wavefield of Figure 3.1(b), than does the structure which results from the single-channel filter.

Figure 3.6 presents an FFT analysis of the information contained in these recovered images. The visual differences between Figures 3.5(a) and 3.5(b) are explained, when the

(a) Wavefield Recovered Using 3-Channel Filter



(b) Wavefield Recovered Using 1-Channel Filter

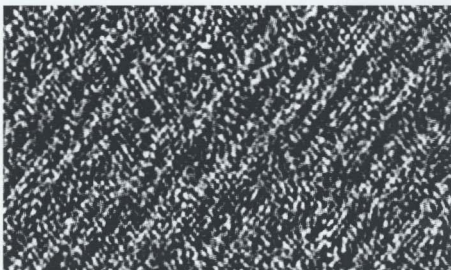


Figure 3.5: Reference wavefield recovered with a standard-attribute operator, $\xi=20$, is shown in (a). This result is definitely superior to the test image obtained with a single-channel operator, shown in (b).

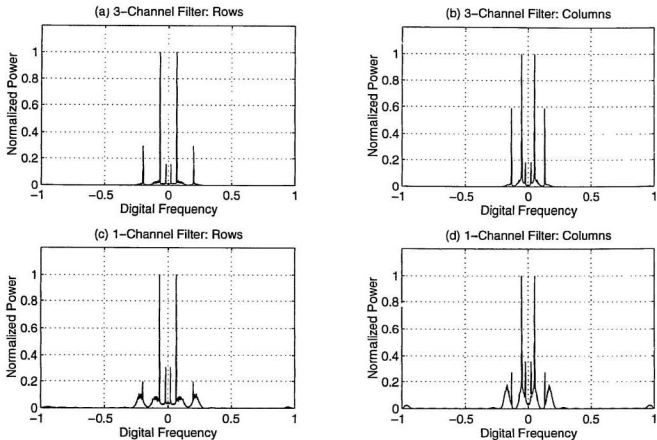


Figure 3.6: 1024-point FFT's, showing relative magnitudes of normalized power within row and column components of recovered wavefields in Figure 3.5.

frequency-domain representations of the standard image are compared to the spectra derived from the test image. Whilst Figures 3.6(a) and 3.6(b) indicate that the three-channel operator does pass some noise, Figures 3.6(c) and 3.6(d) show that the overall relative power of noise passed by the single-channel operator is much higher. This is also exemplified by the presence of some row and column noise components near the Nyquist frequency, which are barely observable in the output from the three-channel operator.

Figure 3.7 displays the \log_{10} -scaled power transfer function defined by Eq. 3.2. For both the row and column components, it is seen that the values of $T_r(f)$ are predominantly negative. Therefore, the overall noise level for the three-channel output is much lower than for the one-channel output. This occurs because addition of three out-of-phase noise components, at any value of f , achieves a further degree of noise suppression than does the single-channel output. The fact that the three-channel output is superior to the one-channel result, can be quantitatively established by averaging $T_r(f)$ over all of the 1024 points shown in Figure 3.7. Granted, the signal components will also contribute to this average, however, since there are very few signal frequencies, it is expected that this will not significantly bias the result. Given this caveat, the averaging operation reveals a mean noise-suppression advantage of -5.98 dB, when the three-channel operation is used in the row dimension. For the columns, the three-channel filter achieves an average noise-suppression advantage of -7.87 dB. From these observations, it is easy to conclude that the three-channel filtering operator does indeed provide superior noise suppression when compared to the one-channel operator.

3.3.3 Influence of α in Determining Noise-Suppression Efficiency

To assess the influence which the value of α will have on the filtering procedure, a test image was generated based on row and column operators derived with a value of $\alpha = I$; this also corresponds to the case for which $\alpha = c$. Figure 3.8(b) shows the result of this operation as it

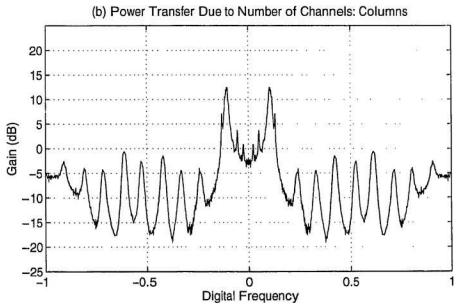
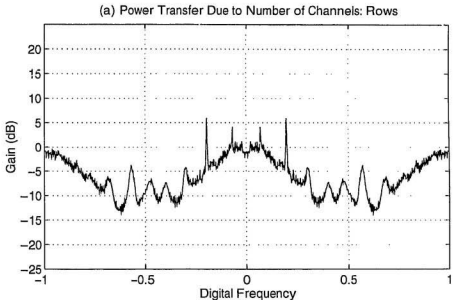


Figure 3.7: Results obtained for $T_r(f)$, based on 1024-point FFT's from the rows and columns of images in Figure 3.5.

(a) Recovered with Alpha=2



(b) Recovered with Alpha=1

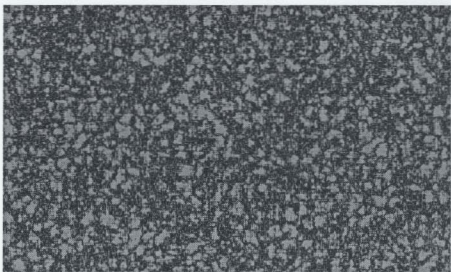


Figure 3.8: Reference wavefield recovered with a standard-attribute operator, $\xi=20$, is shown in (a). This result is undeniably superior to the test image obtained with $\alpha=1$, shown in (b).

compares to the reference image in Figure 3.8(a). Clearly, the test image contains no discernible information whatsoever, and verifies the absolute necessity of selecting $\alpha > c$.

A frequency-domain analysis of these images is presented in Figure 3.9. From Figures 3.9(c) and 3.9(d), it is clear that the test filtering operation has forced a substantial shift in power towards those frequencies existing at the upper end of the spectrum. Some insight into this phenomenon may be acquired with reference to the scalar frequency-domain transfer function of Eq. (2.40). To begin, consider that when an α -value of l is selected, this has the effect of leaving exactly one lag value of the noise correlation function, at $\tau=l$, within the windowed portion of the ACF defined by the set in Eq. (2.15). Based on discussions in Chapter Two, it has been implied that the DFT representation of this ordered set produces the frequency points which appear in the numerator of Eq. (2.40). Clearly, since the first ACF lag (corresponding to $\tau=0$) has been eliminated, the DFT representation of this windowed, ordered set, will consist of a series of Case I spectral lines representing the wavefield components of Figure 3.1(b), embedded in a *flat* spectrum of white noise. However, observe that within the denominator of Eq. (2.40), the noise spectrum is still coloured, and hence, it tapers to very small values at its high-frequency end. This means that for the higher frequency components in Eq. (2.40), a large value in the numerator will be subjected to division by a very small value in the denominator. The result of this relationship, will be to form a passband in the high-frequency region of the spectrum. Consequently, when operating on the image, the filter attenuates all other components, including the spectra associated with the desired signal.

The results for $T_r(f)$ have been presented in Figure 3.10. There it is seen that, for both the row and column components, noise frequencies which are outside of the frequency range spanned by the signal components, are subjected to severe attenuation when mapping from $\alpha=1$ to $\alpha=2$. Hence, the net result is one of attenuation, with an average value of -9.07 dB for $T_r(f)$ in the row dimension, and -12.47 dB in the column dimension.

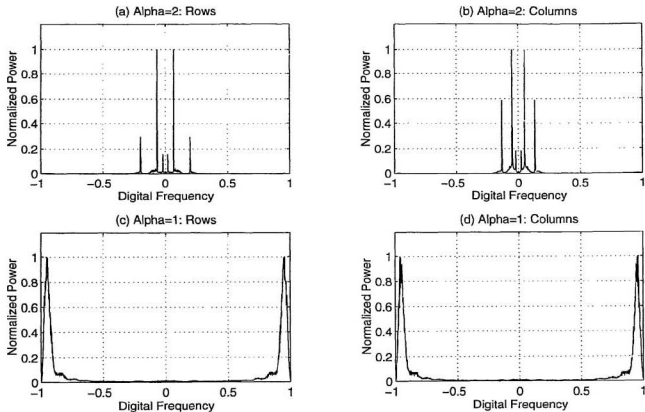


Figure 3.9: 1024-point FFT's, showing relative magnitudes of normalized power within row and column components of the recovered wavefields shown in Figure 3.8.

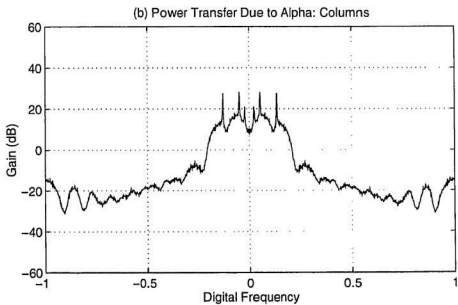
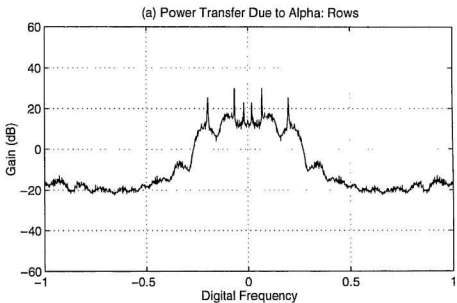


Figure 3.10: Results obtained for $T_r\phi$, based on 1024-point FFT's from the rows and columns of images in Figure 3.8.

3.3.4 Influence of β in Determining Noise-Suppression Efficiency

In order to assess the influence of β upon filter performance, a test image was recovered by selecting a value of $\beta=1$ when deriving the transfer functions; this corresponds to the case for which $\beta=c$ in Eq. (2.74). Based upon earlier discussions in Chapter Two, it is expected that this choice for β will result in a diminution of the noise suppression capability of the three-channel operator. A comparison of results is given in Figure 3.11, which shows the reference image in Figure 3.11(a) and the test image in Figure 3.11(b). Close inspection of the two images does reveal differences, with the standard image, for which $\beta=2 > c=1$, showing a pattern which appears to have fewer variations than does the result which is presented in the test image. Comparatively-speaking, irregularities within the test image are certainly detectable, and leave the impression that this structure resembles the original noise-free wavefield with less commonality than does the reference image.

The frequency domain representations of the row and column components from Figures 3.11(a) and 3.11(b), are shown in Figure 3.12. Once again, close comparison of the normalized noise levels for $\beta=2$, to those obtained for $\beta=1$, indicates that the relative noise power associated with the latter is slightly greater; this observation holds for both the row and column components. Further verification is provided in Figure 3.13, which presents the \log_{10} -scaled power transfer function defined by Eq. (3.2). Here it is seen that $T_r(f)$ is predominantly negative, and again, it is also possible to see evidence of superior noise-suppression within the stopband when mapping from $\beta=1$ to $\beta=2$. This is because, with $\beta=1$, the noise frequencies will still retain a certain degree of phase coherence; consequently, when the three filter outputs are added, destructive interference does not occur to the same extent as it does with $\beta=2$. In fact, when filtering with $\beta=2 > c=1$, a further average noise power attenuation of -2.59 dB is achieved within the row spectra, and an average attenuation of -2.74 dB is achieved in the column spectra. These values, in conjunction

(a) Wavefield Recovered Using Beta=2



(b) Wavefield Recovered Using Beta=1



Figure 3.11: Reference wavefield recovered with a standard-attribute operator, $\xi=20$, is shown in (a). This result is noticeably superior to the test image obtained with $\beta=1$, shown in (b).

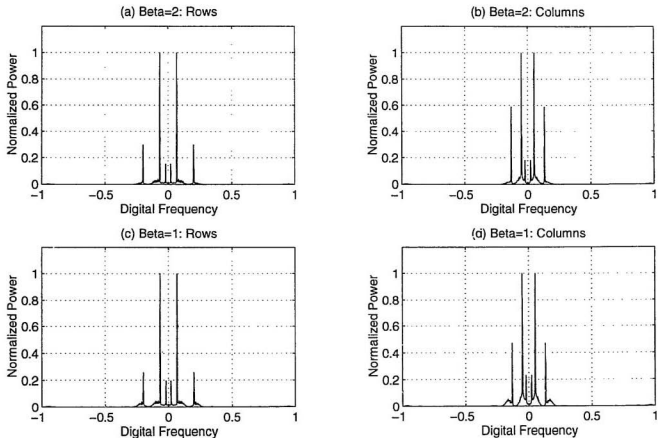


Figure 3.12: 1024-point FFT's, showing relative magnitudes of normalized power within row and column components of the recovered wavefields shown in Figure 3.11.

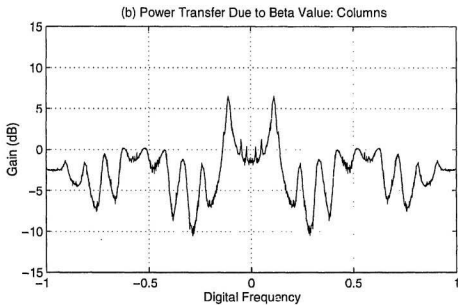
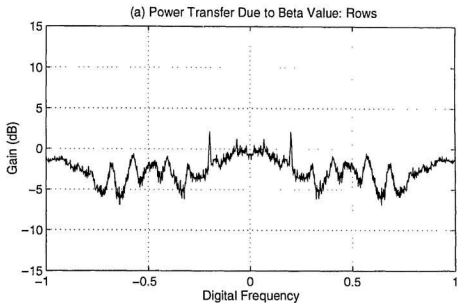


Figure 3.13: Results obtained for $T_r(f)$, based on 1024-point FFT's from the rows and columns of images in Figure 3.11.

with the diagrammatic results, lead to the conclusion that a parametric value of $\beta=2 > c=1$ provides overall superior noise suppression in both the row and column dimensions.

3.3.5 Optimum Method for Selecting Correlation Data When Deriving Column Operators

The optimum procedure for obtaining correlation data was investigated by recovering a test image, based on a column operator which had been derived with intermediate correlation data taken from the row-filtered image. This result was then compared to the standard image, recovered using a column operator derived with correlation data from the original, unfiltered image; in both cases of course, the row operator was based on correlation data obtained from the unfiltered image. The results of this investigation are presented in Figure 3.14, which compares the standard image of Figure 3.14(a) to the test image in Figure 3.14(b). In this case the differences are obvious, and show that use of row-filtered correlation estimates in the column operator, produces a filtered structure which bears virtually no resemblance to the noise-free wavefield of Figure 3.1(b).

Figure 3.15 compares the row and column spectra resulting from these operations. In Figures 3.15(c) and 3.15(d), it is seen that the spectrum of the test image incorporates a noise background which has a much broader bandwidth than the spectra from the reference image, shown in Figures 3.15(a) and 3.15(b). This broader bandwidth is a result of an increase in the spatial extent of correlation within the noise process, due to mechanisms discussed in Section 2.7.3. The results for $T_r(f)$ are presented in Figure 3.16. Here too, the \log_{10} value of the power transfer function yields predominantly negative results, indicating that the standard image has considerably less noise power. The 1024-point average of $T_r(f)$ in the rows is -10.32 dB, compared with a 1024-point mean of -15.54 dB in the columns. These observations confirm that the relative noise power in the standard image is much lower than for the test image, and

(a) Results with Both Operators Based on 2-D ACF of Noisy Image



(b) Results with Column Operator Based on 2-D ACF of Row-Filtered Image



Figure 3.14: Reference wavefield recovered with a standard-attribute operator, $\xi=20$, is shown in (a). This result is clearly superior to the test image, shown in (b), obtained after deriving the column filter from the row-filtered image.

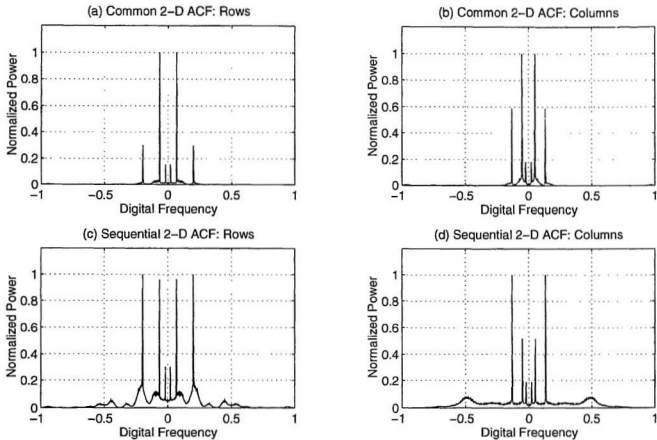


Figure 3.15: 1024-point FFT's, showing relative magnitudes of normalized power within row and column components of the recovered wavefields shown in Figure 3.14.

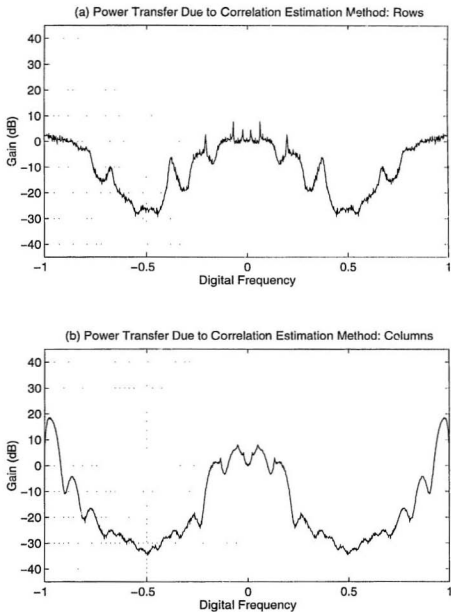


Figure 3.16: Results obtained for $T_r(f)$, based on 1024-point FFT's from the rows and columns of images in Figure 3.14.

substantiates earlier assertions that both row and column operators must be derived by utilization of correlation data from the unfiltered image.

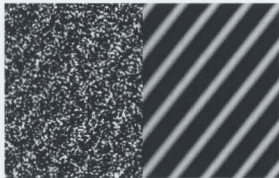
3.4 Evaluation of Filtering Technique for Large ξ

3.4.1 Filtering Operation on Simulated Data Sets

The objective of this Section is to assess the capability of the three-channel filtering technique, when using operator lengths which are longer than at least one period of the lowest frequency component within the desired signal. This is a much more pragmatic approach, since the use of longer filter lengths generally permits the derivation of tighter passbands, with steeper roll-off than was achievable in the previous Section. Passbands which conform more closely in shape to the spectrum of the desired signal, will facilitate a more accurate recovery; hence, the accuracy of results will increase with larger ξ , for any fixed SNR.

Performance of the three-channel filter when operating on the one-component wavefield-plus-noise composite, was assessed by utilization of standard-attribute row and column operators having a length of $\xi=60$. Magnitude response characteristics of these filters have been presented in Appendix III. Since the longest component within this simulated process had a period of 40 pixel units, the filter length was considerably longer than the period of the lowest-frequency component within the image signal process. The results of this operation have been summarized in Figure 3.17. Inspection of the recovered wavefield, shown in Figure 3.17(b), reveals a structure which is virtually identical to its original noise-free counterpart, shown in the right portion of Figure 3.17(a). In fact, the only discernable differences are due to slight undulations in tonal values of the image, along the crests of the recovered wavefield. The normalized power spectra of the recovered row and column components, shown in Figures 3.17(c) and 3.17(d), suggest a complete absence of detectable noise frequencies. From these observations it is easy to form an

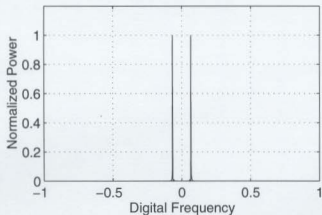
(a) Wavefield with -12 dB SNR



(b) Recovered Wavefield



(c) FFT on Rows



(d) FFT on Columns

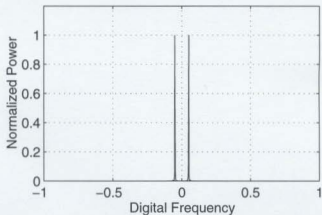


Figure 3.17: Results obtained with three-channel filter, for $\xi=60$. The normalized power spectra in (c) and (d) are 1024-point FFT's, obtained from the recovered wavefield in (b). The original noise-free wavefield, and wavefield-plus-noise composite, are seen in (a).

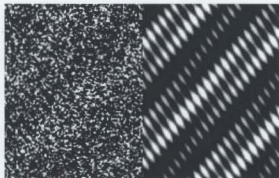
overall conclusion, that the structure within Figure 3.17(b) represents a nearly-complete recovery of the original noise-free wavefield.

In similar fashion, the three-component wavefield-plus-noise composite was processed using standard-attribute operators with a value of $\xi=150$. Here too, because the longest wave period in the image consisted of 100 pixels, this choice for ξ ensured that the filter accommodated all relationships occurring within at least one full cycle of the lowest frequency component from the wavefield. The magnitude response characteristics of these filters are also shown in Appendix III; consistent with the discussion of Section 2.6.3, reference to these Figures will confirm that the passband characteristics of a three-filter set are not constrained to be identical.

Results from this second investigation have been summarized in Figure 3.18. There it is seen that the recovered wavefield, shown in Figure 3.18(b), exhibits no observable differences in structure when compared to its original noise-free counterpart, shown in the right portion of Figure 3.18(a). Once again, the conclusion is that the structure of Figure 3.18(b) represents a nearly-complete recovery of the original noise-free wavefield. The normalized power spectra for row and column components of the recovered wavefield, are shown in Figures 3.18(c) and 3.18(d). Here too, scrutiny of the FFT's will verify the absence of detectable noise components.

Figure 3.19 displays the \log_{10} -scaled power transfer functions, $T_r(f)$, which map the spectral powers of each unfiltered noisy image into the power spectrum of its respective filtered version. Figures 3.19(a) and 3.19(b) show the transfer of power, for the row and column components respectively, of the single wavefield. Figures 3.19(c) and 3.19(d) highlight the transfer of power within the row and column components of the three-component wavefield. For both wavefields, it is clear that severe attenuation of noise has occurred as a consequence of the filtering operation. The curious curvature which is seen in the power transfer spectrum, is produced by the tapered shape of the unfiltered noise spectrum, shown in Figure 3.4. The fact that $T_r(f)$ approaches zero from the negative direction as $|f|$ becomes large, indicates that the

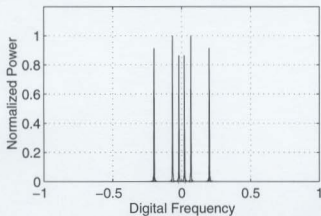
(a) Wavefield with -12 dB SNR



(b) Recovered Wavefield



(c) FFT on Rows



(d) FFT on Columns

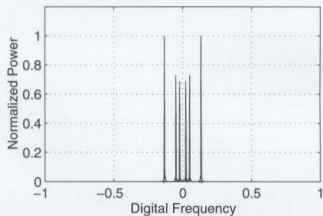


Figure 3.18: Results obtained with three-channel filter, for $\xi=150$. The normalized power spectra in (c) and (d) are 1024-point FFT's, obtained from the recovered wavefield in (b). The original noise-free wavefield, and wavefield-plus-noise composite, are seen in (a).

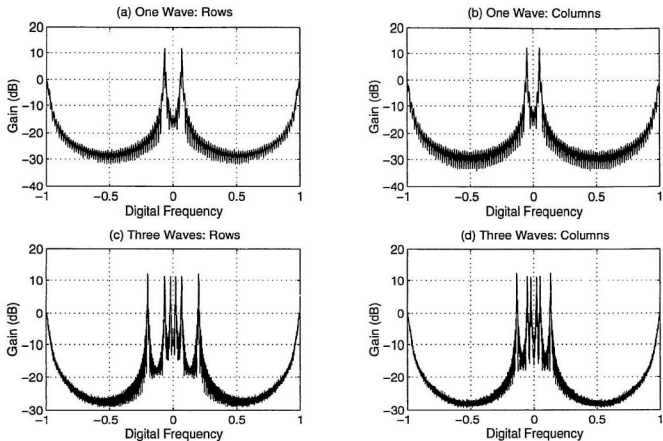


Figure 3.19: Results for $T_r(\ell)$, based on 1024-point FFT's which were obtained from noise-contaminated and filtered versions of the simulated wavefields.

frequencies near Nyquist experience little change in power during filtering. However, since these noise frequencies are of very low power anyway, this has no significant impact upon the filtering capability.

Furthermore, during the discussion pertaining to Eq. (2.40), it was predicted that this tapering would also produce slightly different gain factors amongst those frequencies which comprise the signal component of the spectrum. Close inspection of Figures 3.19(c) and 3.19(d) will reveal a pattern which is consistent with this assertion. With respect to the power transfer in the rows of the three-component image, it is seen that the highest frequency component experiences slightly greater gain than the two lower frequency components. For the columns, it is seen that the gain factors of the three wavefield frequencies appear to increase in proportion to the value of f . This suggests that the tapered noise spectrum could introduce noticeable distortions, for cases in which the desired signal contains high-frequency components which are close to $\pm f$ ($\pm \pi$). However, when the desired frequencies are near the lower portion of the spectrum, the influences upon the output image are visually undetectable, as revealed by the recovered image in Figure 3.18(b). In either case, this phenomenon is a direct consequence of the mathematical relationships which characterize Wiener filter applications in the presence of coloured noise.

Based upon the findings of this Section, it is now possible to conclude that the three-channel filtering technique, utilizing standard-attribute operators, does facilitate a reasonably accurate recovery of a noise-contaminated wavefield, provided that the value chosen for ξ is sufficiently large. Hence, the applicability of vector Wiener filtering to the suppression of coloured noise has now been proven for simulated data. However, consistent with the relationships predicted by Eq. (2.40), it has also been shown that when dealing with correlated noise, the recovered image may incorporate some distortions regarding the relative power levels of its constituent signal frequencies.

3.4.2 Influence of α and β Parameters Upon Filter Performance

In Chapter Two it was observed that for Case I correlation data, filter performance would not be affected by changes in either α or β , provided that these parameters assumed values such that $\alpha > c$ and $\beta > c$. Unfortunately, this inference was established from inspection of the scalar operator only; due to the complexity of the vector version, it was not possible to make similar inferences based on inspection of an analytical form. However, it is expected that this characteristic also extends to the vector version. Therefore, in order to provide evidence in support of this, the frequency response characteristics and filtering performance of the three-channel filter have been examined numerically for selected combinations of α and β values. This analysis is based on correlation data which were estimated from the three-component wavefield-plus-noise composite, shown in Figure 3.1(b).

The investigation was conducted using a standard-attribute operator with $\xi=150$. During one series of tests, a constant value of $\beta=2$ was maintained, while filters were derived for all values of $2 \leq \alpha \leq 50$. Figures 3.20(a), 3.20(b), and 3.20(c) summarize the frequency response trends exhibited by h_{21} , h_{22} , and h_{23} respectively, during these operations. In a second series of tests, the relationship of $\beta=\alpha$ was maintained, while α was increased within the range of $2 \leq \alpha \leq 50$. Figures 3.20(d), 3.20(e), and 3.20(f), summarize the frequency response results which were observed for h_{21} , h_{22} , and h_{23} respectively, during the second series.

To ensure clarity of presentation, the surfaces in Figure 3.20 show the frequency response for the lower half of the positive digital spectrum only, that is, for $0 \leq f \leq 0.5$. Since this bandwidth encompasses all frequencies occurring within the desired signal, very little information has been lost by omitting the upper half of the spectrum. These results are based on 64-point FFT's of the one-sided spectrum; hence, only the first 32 points of each frequency response magnitude are shown. In addition, note that results have been presented for the row component of the image only. Since, in this example, the rows and columns were generated by the same

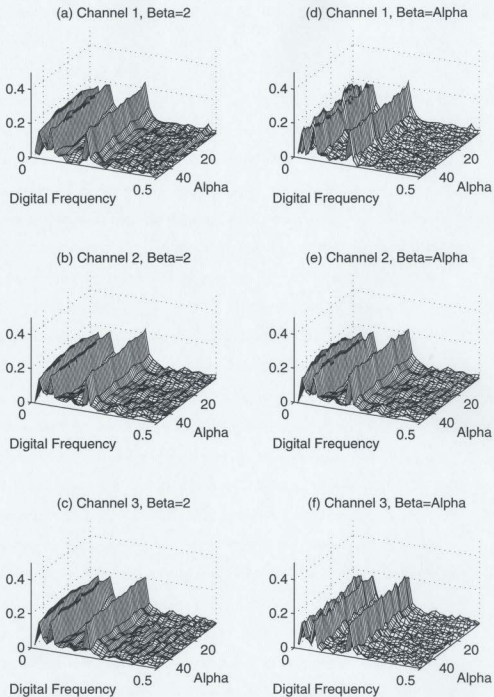


Figure 3.20: Magnitude response of the vector Wiener filter, as a function of adjustments to correlation shape parameters α and β .

procedure, it is clear that any patterns emerging from the analysis would also hold for the columns.

From inspection of Figures 3.20(a), 3.20(b), and 3.20(c), it is apparent that for constant β and varying α , the peak frequency responses do not change appreciably. While there are certainly fluctuations, the overall impression is that the peak frequencies, which correspond to the wavefield components, are consistently dominant in relation to the background frequencies. In particular, note that there exists no value of α for which the frequency response of the signal component decays to magnitude levels at or about the level of the background frequencies. This strongly suggests that filter output, for any given α , would not differ significantly from the output associated with any other value of this parameter, assuming $\alpha > c$.

Based upon Figures 3.20(d), 3.20(e), and 3.20(f), it is also apparent that peak frequency responses do not exhibit any overall trend of decay, and consistently dominate the spectrum for all chosen values of $\beta=\alpha$. Here too, it is possible to conclude that filter performance is not affected significantly when β and α are changed by equivalent magnitudes. However, it is interesting to note that the Channel 1 filter response for $\beta=\alpha$, is somewhat more erratic than its counterpart for $\beta=2$; a similar observation can also be made regarding the Channel 3 response and, to a much lesser extent, the Channel 2 response as well. A possible explanation, is that this phenomenon occurs because the estimated correlation functions will retain some perturbations due to noise. Such perturbations must inevitably introduce some variability into the surfaces of Figure 3.20, because the correlation information which is used in filter derivation will change with each new value taken by either α or β .

In fact, when β is adjusted along with α , each new value of β introduces an entirely new set of CCF data to the derivation process. Furthermore, a change in the value of α means that a slightly different section of the ACF is windowed for each derivation. These changes introduce a relatively high degree of variability. However, when β is held constant, the same correlation

functions are used for all α ; hence, the only variations occurring, are due to the windowing of a slightly different section of the same CCF's and ACF as α assumes each new value. Since α changes by increments of 1, this means that the correlation information used in each new derivation, differs only by nine scalar values from the data which was used with the previous value of α ; this can be verified by studying the RHS of Eq. (2.68). It is easy to conclude therefore, that this must introduce less variability than would otherwise occur when the entire set of cross-correlation data is replaced for each derivation. Furthermore, these correlation functions have been based on biased numerical estimates, discussed in [24] & [31]. This is a numerical procedure which deliberately tapers the function as $|\tau|$ increases, in order to reduce estimation errors. Consequently, these estimated correlation functions are not exactly periodic for $\alpha > c$; this implies that they may yield spectral characteristics which depart slightly from the rigorous definitions established for Casf=1 data. For these reasons, it should be expected that the surfaces in Figure 3.20 might not correspond exactly to the established theory.

Having verified that peak frequency responses do not vary significantly with changes in α and β , supplementary numerical evidence can also be provided, to show that the filter output will not be compromised by selected adjustments to these parameters. In support of this, the three-component wavefield-plus-noise composite was subjected to four additional standard-attribute filtering operations, using a vector operator of length $\xi=150$ for selected combinations of α and β . Figures 3.21(a), 3.21(b), and 3.21(c) present the images which were recovered using a constant value of $\beta=2$, for selected α -values of $\alpha=2$, $\alpha=14$, and $\alpha=26$ respectively. Of course, the image for $\alpha=\beta=2$ is the same one which was generated for Figure 3.18; it has been presented in Figure 3.21 for purposes of comparison. Study of these wavefields will not reveal any noticeable differences, either when comparing each one to another, or when comparing any one to the original wavefield in Figure 3.1(b). In similar fashion, Figures 3.22(a), 3.22(b), and 3.22(c) show the wavefields which were recovered with $\alpha=\beta=2$, $\alpha=\beta=14$, and $\alpha=\beta=26$ respectively. Again,

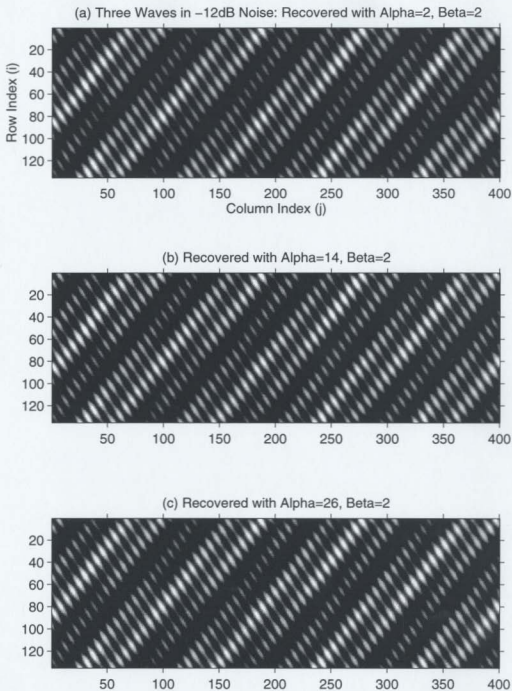


Figure 3.21: Wavefields recovered using standard-attribute operator, $\xi=150$, for selected values of correlation shape parameter α , with constant value of shape parameter $\beta=2$.

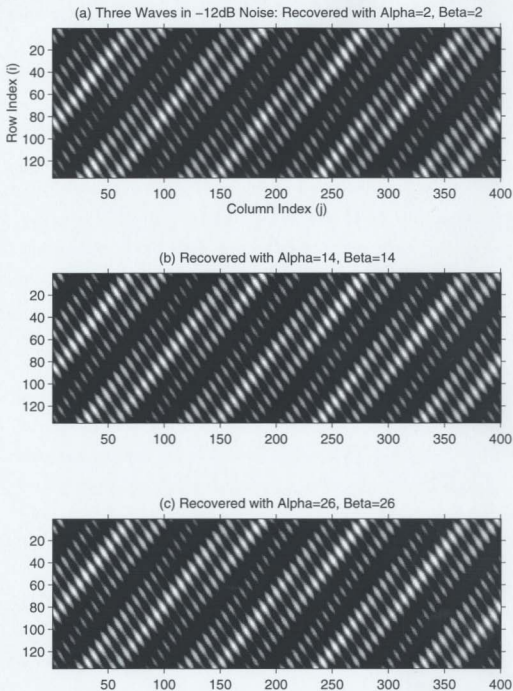


Figure 3.22: Wavefields recovered using standard-attribute operator, $\xi=150$, for selected values of correlation shape parameter α , with shape parameter $\beta=\alpha$.

these wavefields show no apparent differences, either when compared amongst themselves, or when they are individually compared to Figure 3.1(b); this provides further verification that filter output is unaffected.

Therefore, numerical evidence has been provided, which attests to the insensitivity of the vector operator regarding changes in the parameters α and β , with $\alpha > c$ and $\beta > c$, for Case I correlation data. Although the results presented in Figures 3.20, 3.21 and 3.22 may initially be perceived as unremarkable, they do provide a valuable reference against which subsequent investigations may be compared. In Chapter Five it will be seen that a similar analysis, using Case II correlation data, will yield results which are in dramatic contrast to the findings presented in this Section.

3.5 Summary

In this Chapter, numerical evidence has been provided in order to support several conclusions which were made from the analytical results presented in Chapter Two. In particular, it has been verified that optimum signal recovery requires utilization of a three-channel vector Wiener filter, for which $\alpha > c$ and $\beta > c$, with both the row and column versions of this operator being derived using a two-dimensional ACF estimated from the noisy image. This filter has been referred to as the standard-attribute operator. In addition, it has also been numerically verified that, for Case I correlation data, the filtering operation is not significantly affected by changes in α or β , provided that these parameters are chosen such that $\alpha > c$ and $\beta > c$. Consequently, a vector filtering procedure for the recovery of stationary processes having Case I correlation characteristics, has now been established and numerically verified in the presence of broad-band coherent noise.

CHAPTER FOUR

APPLICATION OF FILTERING TECHNIQUE TO OCEAN WAVE SCENES WITHIN SAR IMAGERY

4.1 Introduction

Building upon the preceding theoretical and numerical results, this Chapter examines the performance of the filtering technique when operating to recover a stationary process which will be shown to exhibit Case II correlation characteristics. The data set to be used in this analysis, consists of two ocean wave scenes which were imaged by airborne synthetic aperture radar (SAR). These incorporate 1224×1224 pixels each, and were obtained over Canadian East Coast waters by the Canada Centre for Remote Sensing (CCRS), on the fourteenth and eighteenth of November, 1991. The objective of this Chapter is to demonstrate that the vector operator can produce a filtered version of these images, which represents a reasonable facsimile of the noise-perturbed wavefield found in the unfiltered versions. Unlike the simulations of the previous Chapter, there exists no absolute information regarding the characteristics of the noise-free version. Hence, recovery capability must be established by comparison of smoothed wavefield geometries with their noise-perturbed counterparts, supplemented by examination of row and column spectra, and power transfer function characteristics.

4.2 Image Characteristics

The methods by which SAR data are gathered and transformed into imagery, are mathematically intricate. While detailed discussions of such procedures may be found in [34], [35] & [36], it is not necessary to provide further elaboration here; this is because the scope of this

project is limited to recovery of the process which exists within the image. While there is certainly a relationship between the actual ocean wave scene and the wavefield which appears in the image, the transfer function which maps the former into the latter is non-trivial, as discussed in [37]. Hence, no attempt will be made to establish any relationship between the filtered image wave scene, and the actual wavefield which was imaged by the radar. From the discussions of preceding Chapters, it will be clear that the filtering operations are not dependent upon this relationship in any way.

It is important to observe though, that the characteristics of data gathered by airborne SAR, will impose some departures from the mathematical assumptions which were discussed in Chapters One and Two. In particular, the SAR images used in these tests have not been corrected for range distortions which result from the radar imaging process. In order to appreciate the implications of this statement, consider that for a typical airborne SAR, the centre axis of the radar beam projects obliquely onto the ocean surface. The actual depression angle of this centre axis relative to the flight plane of the aircraft is determined by the configuration of the radar, which may vary from one installation to another. In general however, the antenna beam axis and the aircraft velocity vector intersect orthogonally, to form the orthogonal basis vectors of a virtual plane which intersects the ocean surface at some distance from the aircraft; this plane is referred to as the slant plane. The slant plane dimension which parallels the antenna beam axis is known as the slant range dimension, while the dimension which parallels the aircraft velocity vector is referred to as the azimuth dimension. The basic geometry of a SAR imaging process is illustrated in Figure 4.1; note here that the azimuth dimension is normal to the page plane.

As illustrated by Figure 4.1, the radar imaging process involves mapping the backscattered energy into pixels, denoted by p'_j , which form a matrix of elements within the slant plane. Each j 'th element is assigned a digital grey level which is proportional to the energy returned from the corresponding j 'th patch of ocean, denoted by p_j , existing in the surface plane.

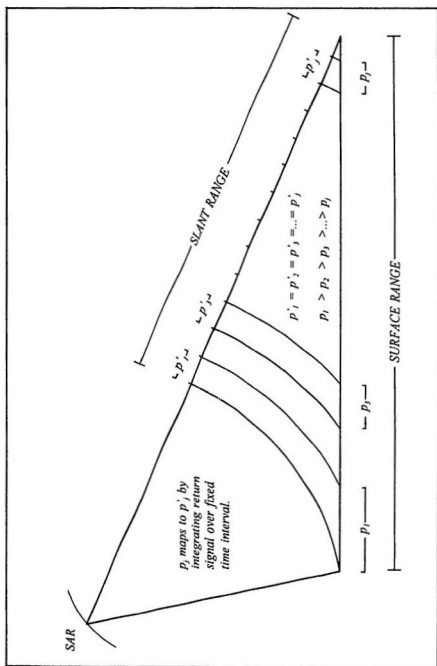


Figure 4.1: Geometry of SAR imaging process.

Within any i 'th row (range line) of the slant plane matrix, each pixel position along that row corresponds to a range distance from the antenna. This distance is established by the time which elapses between the transmission and reception of a microwave pulse. The resulting slant plane matrix is then constructed row by row in the column dimension, as the aircraft flies along the azimuth vector. Since the slant plane matrix is mapped to a digital image, this implies that the procedure by which the image rows are generated is different from that by which the columns are formed. Each pixel occurring in the slant plane will be of a constant physical size. In this particular case, the dimensions were $4.0\text{ m} \times 3.9\text{ m}$ in range and azimuth respectively, for the Nov. 14 image; pixel specifications were not available for the Nov. 18 image.

However, as shown by Figure 4.1, the geometrical relationship between each slant plane pixel and the patch of ocean surface which it represents, is actually non-Euclidean. In fact, the range dimension of each discrete ocean patch, p_r , decreases with increasing range distance from the radar, despite the fact that the slant range pixel dimension, p'_r , remains constant. This means that the information content of each pixel decreases along the range dimension, but remains constant along the azimuth dimension. Therefore, if any given row of the slant plane image is envisioned as a digital sample of a one-dimensional waveform on the ocean surface, then these areal contractions are equivalent to an ever-changing sample rate, which increases non-linearly along the range dimension. An additional consideration, is that microwave energy in the near range reaches the ocean surface at a steeper angle than energy in the far range; this will result in a changing SNR across the range dimension. Overall, these factors imply that there will be some alterations in the statistical properties of slant range data, as a function of range position. The two images which were made available by CCRS, and which have been analyzed in this Chapter, are in slant range format. However, these images are actually subscenes which were extracted from the far range region of the slant plane, where it is known that range-dependent variations are minimized. Nevertheless, it is certain that these imaged processes cannot be ideally stationary in

the range dimension. In addition to this, since the Nov. 18 image was gathered at an altitude of approximately 3000 m, while the Nov. 14 image was obtained at approximately 1800 m, the former covers a much larger patch of ocean than the latter; hence, the wavefields are not directly comparable.

Of further relevance is the fact that, while in their original slant plane formats, the image pixels consisted entirely of non-negative intensities. Consequently, the two-dimensional processes within these images exhibited non-zero means. As well, because of aircraft motion, the images also contained some intensity variations which were not due to backscatter properties of the ocean surface. Here too there exist violations of the previous assumptions, which specify that the two-dimensional image processes will have an expected value of zero. Therefore, in order to transform the imaged process to a zero-mean process, and to remove the unwanted effects of aircraft motion, a two-dimensional, third-order polynomial trend surface was computed from the data in each image. When each model trend was then subtracted from its respective image, an approximate zero-mean process resulted, and spurious intensities due to motion were reduced. Basic statistics, computed from each image after such detrending, are summarized in Figure 4.2; the lower trace in each plot represents the mean value of pixels averaged along the respective row or column component of the image, while the upper trace represents positive standard deviation. Both the column index and the row index positions, which are shown on the x -axis, have their origins in the upper left-hand corner of the image.

From Figure 4.2(a), it is seen that the row means of the detrended Nov. 14 image exhibit both positive and negative minor fluctuations, which are very near to zero; within these fluctuations, there exists no large-scale trend. Similarly, the positive standard deviation of pixels is constant at about 16, for all rows of the image. However, Figure 4.2(b) shows that for the column dimension of this image, the mean pixel values incorporate a long-period undulation of low amplitude. As well, there is a slight increase in the positive standard deviation of the column

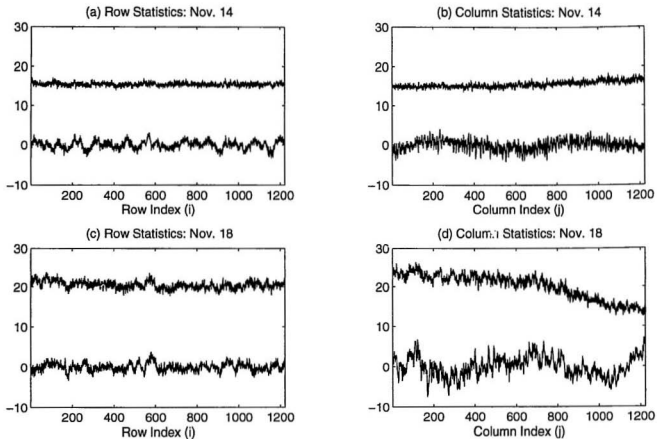


Figure 4.2: Means (bottom trace) and positive standard deviations (top trace), for the row and column components of Nov. 14 and Nov. 18 signal-plus-noise processes.

pixels, from about 15 for columns in the left portion of the image, to about 17 for columns in the right portion. Since the left and right portions of the image correspond to the near range and far range regions of the SAR imaging process, such an increase is consistent with the expected departures from stationarity which were discussed previously. From Figure 4.2(c), it is seen that the row means for the detrended Nov. 18 image, behave very much like those for the Nov. 14 case; that is, they exhibit minor fluctuations about zero, with no discernible trend. The positive standard deviation remains very close to 20 for all rows, with a slight increase apparent in the left portion of the image. However, Figure 4.2(d) reveals that within the columns of the Nov. 18 image, there exists significant trends for both the means and standard deviations, which are far more severe than the cases just discussed. In particular, the column means exhibit noticeably greater departures from zero, while the positive standard deviation decreases from a value of approximately 24 in the near range, to a value of approximately 14 in the far range. This implies that there will be definite departures from the WSS assumption within the Nov. 18 image.

Therefore, it is clear overall, that the detrended SAR images will continue to retain some departures from those mathematical assumptions which were strictly adhered to by the simulated images in Chapter Three. These departures have been imposed by a combination of the radar imaging geometry, and a limited effectiveness of the detrending algorithm; however, such factors must be tolerated, because they are unavoidable. For instance, with respect to image format, only slant range data were available from the CCRS offices. With regard to detrending, it is true that a polynomial of higher order might result in less variability about the mean; still, there cannot be any guarantee that it will not remove useful information as well. Therefore, detrending via a third-order algorithm is the highest order of preprocessing which can be attempted with confidence. The fact that such observed departures from assumption do exist, suggests that these imaged processes, especially the Nov. 18 image, will permit a robust

assessment of the filtering technique. This is because the filters will be operating in situations which are less than ideal, with respect to the mathematical structures inherent to the image data.

4.3 Correlation Characteristics of Imaged Processes

4.3.1 Estimation of Two-Dimensional and One-Dimensional Correlation Functions

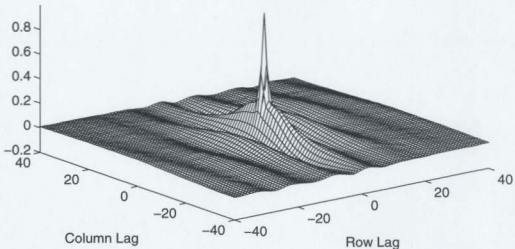
4.3.1.1 Numerical Estimates of the Two-Dimensional ACF

Following the detrending operation, the next stage in preparation for filtering of the SAR images, was the estimation of a two-dimensional autocorrelation function from each image. This is the numerical equivalent of $R_{xx}(\tau_c, \tau_R)$ in Eq. (2.5), and the objective of this operation was to identify the signal and noise relationships which were present within the images. Consequently, in order to reduce computational complexity, the two-dimensional ACF's were estimated from a 1024×1024 subscene occurring within each 1224×1224 image. A portion of each resulting correlation surface is shown in Figures 4.3 and 4.4, for the Nov. 14 and Nov. 18 images respectively.

Figure 4.3(a) shows a small portion of the two-dimensional ACF from the Nov. 14 image; this surface has been normalized so that its maximum value, $R_{xx}(0,0)$, is equal to unity. From inspection of the correlation surface, it is immediately clear that the image has a significant broad-band noise component, which is represented by a prominent tapered spike located at the centre of the ACF. Complementary to this, Figure 4.3(b) shows a contour map for a larger subregion of the correlation surface, and for normalized correlation values in the range $0 \leq R_{xx}(\tau_c, \tau_R) \leq 0.1$ only. With the contour values restricted to this range, only patterns relating to the signal components are observable.

Each lag unit in the correlation surface and map, corresponds to a pixel unit in the image; consequently, periodic patterns exhibited by the correlation data, reflect wavefield periods occurring in the imaged process. Study of the Nov. 14 map, in Figure 4.3(b), will reveal that the

(a) Autocorrelation Function: Nov. 14 Wavefield



(b) Contour Map of ACF Coefficient Range 0 to 0.1

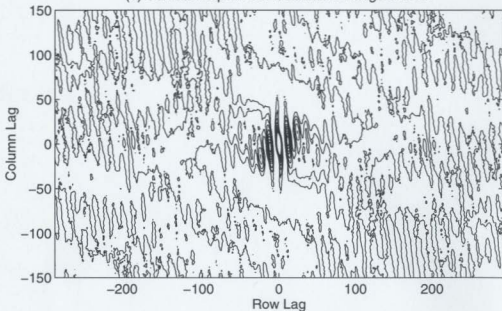
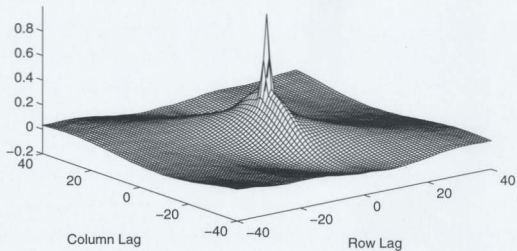


Figure 4.3: Normalized autocorrelation data, obtained from 1024×1024 subscene of Nov. 14 image.

(a) Autocorrelation Function: Nov. 18 Wavefield



(b) Contour Map of ACF Coefficient Range 0 to 0.1

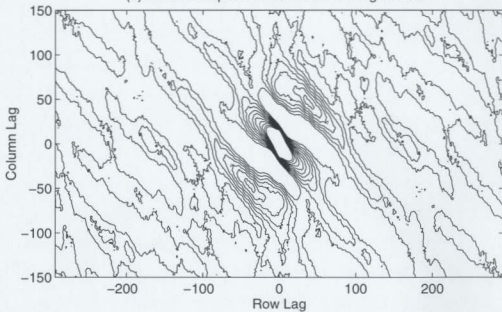


Figure 4.4: Normalized autocorrelation data, obtained from 1024×1024 subsense of Nov. 18 image.

correlation function contains a low-frequency component, which has a period of approximately 100 correlation lags in the column dimension, and approximately 200 lags in the row dimension. This wavefield component has a major axis which is oriented at approximately 30° counter-clockwise (CCW) from vertical; it is seen in the centre of the map, to either side of the axis along which $\tau_r=0$. As well, Figure 4.3(b) indicates the presence of a higher frequency component, which has a period of approximately 100 lags in the column dimension, but only approximately 15 lags in the row dimension. This wavefield, which has its major axis oriented at approximately 10° CCW from vertical, may be seen in all regions of the map. Finally, near the upper left and lower right borders of the map, there is some evidence to indicate the possible presence of a wavefield which is oriented at close to 90° CCW from vertical. This possible wavefield also has an approximate period of 100 lags in the column dimension, but has a period which exceeds the number of pixels in the row dimension; hence, the wavefield has a frequency which is very close to DC within the rows. The fact that this wavefield is detectable only at large distances from the centre of the map, indicates that it is of relatively low power in comparison to the other wavefields. Study of the patterns in Figure 4.3(b), suggests that it emerges only after the correlation power of these wavefields has decayed to a certain level.

Figure 4.4(a) shows a normalized portion of the correlation surface which was extracted from the Nov. 18 image. Here too, there exists a significant noise component, represented by a prominent tapered spike at the centre of the correlation surface. However, the contour map for $0 \leq R_{xx}(\tau_c, \tau_r) \leq 0.1$, shown in Figure 4.4(b), suggests that this ACF contains one main wavefield component which is dominant overall, oriented at approximately 45° CCW from vertical. This is a wavefield which has a period of approximately 80 lags in the column dimension, and 80 lags in the row dimension. Figure 4.4(b) does suggest the possible presence of one other component, oriented at about 140° CCW from vertical, however it is only present near the centre of the map, indicating that its correlation power decays very rapidly. As a

reflection of this possible wavefield, the contour pattern contains three regions within which the contours are very closely spaced. In a three-space context, very close contours are indicative of a rapidly increasing slope; hence, these contours indicate the presence of three "mounds" in the central region of the map. Each mound has a major axis orientation of approximately -45° CCW from vertical, which is consistent with the orientation of most other features in the map. However, when the mounds are enveloped as a group, it is apparent that the major axis of the envelope is oriented at about 140° CCW from vertical. This would suggest that a low-power wavefield crosses the image at this orientation.

4.3.1.2 Numerical Estimates of One-Dimensional Correlation Functions

One-dimensional autocorrelation functions, estimated from the rows and columns of the Nov. 14 image, are shown in Figures 4.5(a) and 4.5(b) respectively. For both the row and column dimensions, the shape of the ACF is consistent with severe damping of one or more apparently sinusoidal waveforms. In fact, most of the power is contained within approximately the first ± 50 autocorrelation lags, and it is in this interval that the exponential decay is most observable, with power levels assuming nominally near-zero values for subsequent lags outside of this range. In conjunction with the prominent noise spike, this suggests that the Case II analytical model from Eq. (2.12) would be a good approximation to these numerical estimates.

Similarly, Figures 4.5(c) and 4.5(d) present the one-dimensional autocorrelation functions obtained from the rows and columns of the Nov. 18 image. These estimates also yield evidence of exponentially-damped sinusoidal components, along with a significant broad-band noise component; however, it is apparent that the damping factors are not as significant as those which are implied by the Nov. 14 ACF's. This conclusion is drawn from the fact that the Nov. 18 row and column ACF's continue to exhibit noticeable power levels, well beyond the lag values at which significant power ceased to be observed in the Nov. 14 ACF's. Therefore, for the Nov.

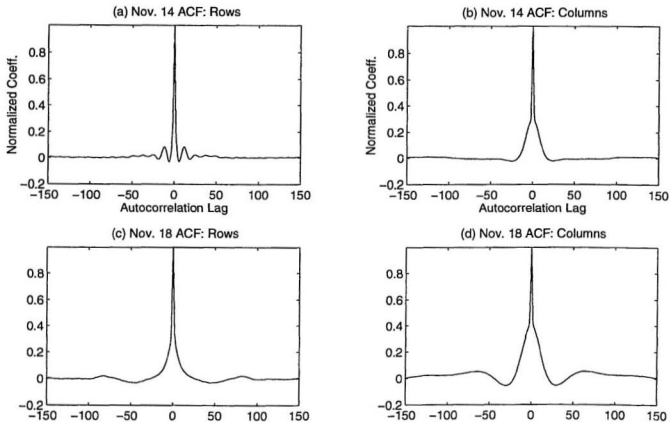


Figure 4.5: Normalized one-dimensional autocorrelation functions, for the row and column components of the Nov. 14 and Nov. 18 signal-plus-noise processes.

18 image also, it is possible to conclude that the exponentially-damped Case II model proposed in Chapter Two, is a good analytical approximation.

The structure of one-dimensional row and column cross-correlation functions can also be inferred from the correlation surfaces presented in Figures 4.3(a) and 4.4(a). This is achieved by fixing the column lag, τ_c , at some constant value of $\tau_c = \pm\beta \neq 0$, and then extracting the function which has its domain over all values of τ_r . The result will be a numerical estimate of the regional CCF for the specified distance, β , between rows. Similarly, fixing the row lag, τ_r , at a specified value of $\tau_r = \pm\beta \neq 0$, and extracting the function having its domain over all values of τ_c , gives the regional CCF for the distance, β , between columns.

Figure 4.6 presents the row and column CCF's which have been extracted via the above procedure, from the Nov. 14 image. Figures 4.6(a), 4.6(b), and 4.6(c) present the numerical estimates of row CCF's represented as $R_{rr}(1, \tau_r)$, $R_{rr}(2, \tau_r)$, and $R_{rr}(3, \tau_r)$ respectively. By similar convention, Figures 4.6(d), 4.6(e) and 4.6(f) show the numerical estimates for column CCF's represented as $R_{cc}(\tau_c, 1)$, $R_{cc}(\tau_c, 2)$, $R_{cc}(\tau_c, 3)$ respectively. Figures 4.7(a) through 4.7(f) show the numerical equivalents to these functions, obtained from the correlation surface for the Nov. 18 image. Study of the CCF's contained within both sets of Figures, in conjunction with the one-dimensional ACF's of Figure 4.5, leads to an interesting observation regarding interaction of signal and noise components within the correlation functions. For the *column* dimension of both images, the noise contribution to the one-dimensional correlation functions is distinctive, in the sense that the noise component can be visually inferred from an obvious change in the shape of the signal-plus-noise correlation function. This shape change presents itself as a spike, which emerges from the rounded undulation of the plotted correlation geometry. However, in the *row* dimension, no such change is apparent; hence, for the rows, it is not possible to use the shape of the correlation function as a means by which to infer the extent of noise correlation. Upon initial consideration, this would seem to hold ominous ramifications for determining the value of c in

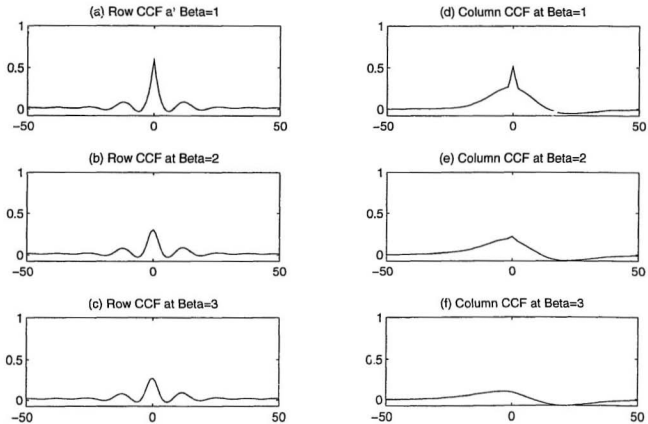


Figure 4.6: Normalized one-dimensional row and column CCF's for Nov. 14 image, extracted from the two-dimensional ACF of Figure 4.3.

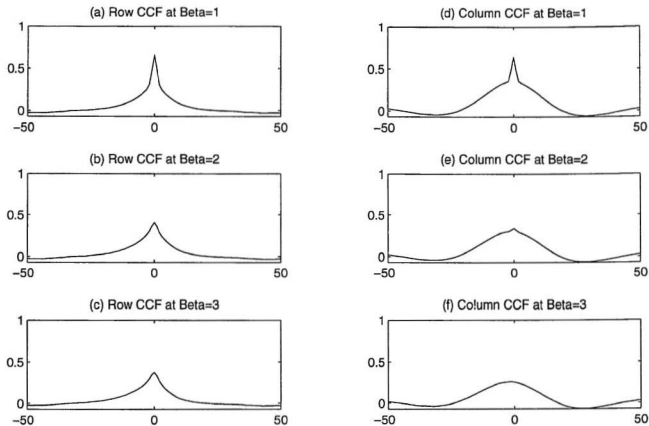


Figure 4.7: Normalized one-dimensional row and column CCF's for Nov. 18 image, extracted from the two-dimensional ACF of Figure 4.4.

the row dimension, which is a prerequisite to establishing the values of α and β when deriving filters for these images. Fortunately, there is an indirect procedure by which the value of c may be estimated; this will now be discussed.

4.3.2 Estimating c , the Spatial Extent of Noise Correlation

Based upon observations made in conjunction with Figures 4.5, 4.6, and 4.7, it is apparent that the extent of noise correlation, within and between rows, cannot be directly estimated. Therefore, in order to develop a reliable method of inference, begin by referring to the sectioned column correlation functions which are shown in Figure 4.8 for both images. Here, the one-dimensional ACF, $R_{ii}(\tau_c, 0)$, is denoted by 'o', with CCF's $R_{ii}(\tau_c, 1)$, $R_{ii}(\tau_c, 2)$, and $R_{ii}(\tau_c, 3)$ identified by 'x', '*', and '+' respectively. To establish the extent of noise autocorrelation in the column dimension at row lag $\tau_r=0$ for both images, observe firstly that points $R_{ii}(0, 0)$ and $R_{ii}(\pm 1, 0)$ are clearly components of the noise spike. However, with additional reference to points $R_{ii}(\pm 2, 0)$, it is apparent that these also form part of the noise component within the column ACF's. This is based on the observation that in both Figures 4.8(a) and 4.8(b), the ACF coefficients at $R_{ii}(\pm 3, 0)$ appear to represent a point of inflection. In fact, as τ_c approaches the value of ± 3 from the direction of ± 8 , the slope of the ACF continues to decrease. However, during the transition from $\tau_c=\pm 3$ to $\tau_c=\pm 2$, it is clear that this trend terminates and the slope begins to increase once more. These points of inflection have been indicated by the symbols \sphericalangle and \sphericalangle' in Figure 4.8. Based upon this observation, it is possible to infer that the noise has significant autocorrelation at column lags 0, ± 1 , and ± 2 . However, it is extremely important to note that the column autocorrelation coefficients at $R_{ii}(\pm 1, 0)$ and $R_{ii}(\pm 2, 0)$, are also the zero-lag points within the row cross-correlation functions at row spacings of $\beta=1$ and $\beta=2$. Hence, it has now been established that the noise is self-correlated for the first two non-zero lags in the columns, and

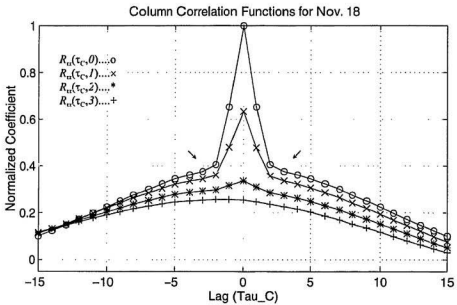
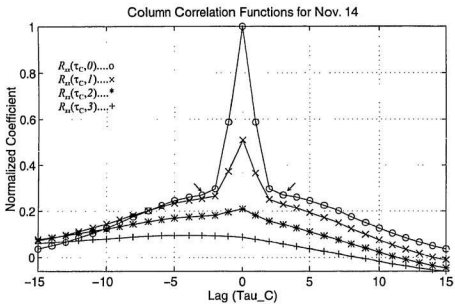


Figure 4.8: Normalized ACF and CCF sections, from column components of Nov. 14 and Nov. 18 images.

cross-correlated at the *zeroth* CCF lag between rows which are separated by distances of $\beta=1$ and $\beta=2$.

Refer next, to the column cross-correlation functions of both images, at the coefficient values of $R_{cc}(0,1)$, $R_{cc}(0,2)$ and $R_{cc}(0,3)$, which are the zero-lag points in Figures 4.8(a) and 4.8(b). When comparing these at column lag $\tau_c=0$, it is seen that the noise spike is present at $R_{cc}(0,1)$ and $R_{cc}(0,2)$, but appears to be absent at $R_{cc}(0,3)$. This indicates that the zero-lag ($\tau_c=0$) magnitude of the noise cross-correlation functions in the columns, is also significantly non-zero at cross-channel spacings $\beta=1$ and $\beta=2$. However, by argument similar to above, the column *cross-correlation* coefficients, $R_{cc}(0,\pm 1)$ and $R_{cc}(0,\pm 2)$ at $\tau_c=0$, are also the *autocorrelation* coefficients for row correlation lags $\tau_r=\pm 1$ and $\tau_r=\pm 2$. This implies that the extent of non-zero noise autocorrelation power in the rows also includes ACF lags $\tau_r=\pm 1$ and $\tau_r=\pm 2$. Thus, it has been demonstrated that the noise is self-correlated for the first two non-zero correlation lags in the rows, and has a significant zeroth-lag cross-correlation between columns which are separated by distances of $\beta=1$ and $\beta=2$.

Therefore, for both the Nov. 14 and Nov. 18 images, it has been established that the noise component of the one-dimensional ACF, in both rows and columns, is significantly non-zero for autocorrelation lags $\tau=0$, $\tau=\pm 1$, and $\tau=\pm 2$. Similarly, for the row and column cross-correlation functions of both images, it has been established that the noise component is non-zero at CCF lag $\tau=0$ for $\beta=1$ and $\beta=2$. Furthermore, careful inspection of Figures 4.8(a) and 4.8(b) will yield evidence to indicate that the noise is correlated for *most* combinations of $-2 \leq \tau_c \leq 2$ and $-2 \leq \tau_r \leq 2$. This can be established with the aid of Eq. (2.7), however, the statements made in the preceding paragraphs are sufficient to define to value of c . As well, there exists no evidence whatsoever to indicate the possible existence of noise correlation at jointly non-zero correlation lags $|\tau_c| > 2$ and $|\tau_r| > 2$. This establishes an estimate of $c=2$ for the spatial extent of correlation within the noise process. Therefore, the extent of row and column noise autocorrelation

has demonstrated that the vector filter must be derived with a prediction gap of $\alpha > 2$, for both images. In conjunction with this, the existence of significant noise cross-correlation at the observed lags requires that the vector filters should also be derived with $\beta > 2$.

4.4 Results from Vector Filtering Operations

4.4.1 Overview

Within this Section, the effectiveness of the vector filtering technique has been tested by filtering each of the detrended Nov. 14 and Nov. 18 SAR images. Correlation functions extracted from these images indicate that they satisfy the Case II criterion. Based upon the findings of the previous Sections, the parametric values of the standard-attribute operators were chosen to be $\alpha=3$, $\beta=3$, and $\xi=200$. For the most part, this filter length is approximately equivalent to, or in excess of, one full period of the imaged waveforms which were revealed by the correlation surfaces of the previous Section. A possible concern is with respect to the row component of the 30° wavefield which occurs in the Nov. 14 image. From Figure 4.3(b), it has been observed that the period of this component was approximately 200 pixels; therefore, as an initial consideration, it might seem appropriate to use an operator of slightly greater length. In fact, if the row ACF were not exponentially-damped, then this would be highly desirable. However, reference to Figure 4.5(a) shows that even at 150 autocorrelation lags, the damping is so severe that there exists very little power in the autocorrelation function. Naturally, this also holds for the cross-correlation functions, but the smaller x-axis range in Figure 4.6 does not make this apparent. With the choice of $\xi=200$ momentarily notwithstanding, this implies that extending the value of ξ beyond 150 might actually be superfluous, because accuracy of the filtering procedure will probably not improve significantly. Therefore, the choice of $\xi=200$ ensures that the maximum possible extent of *useful* correlation information has been incorporated within the vector operator.

Furthermore, the specific orientation of the approximately 90° wavefield within the Nov. 14 image is also of some concern in this regard. Since the stated orientation of 90° is only an approximation, it is quite likely that the major axis of this wavefield may not be exactly orthogonal to the column dimension. If this is so, then the rows will incorporate a very low frequency component, one full cycle of which may not actually exist within the image. This indicates the practical limitations of trying to incorporate one full cycle within the filter transfer function, when operating on bandpass processes. In such situations, image rotation algorithms do not offer a possible solution, because with this type of process there may be numerous wavefields of different orientations; furthermore, rotation algorithms may significantly alter the correlation properties of the noise.

The frequency response magnitude characteristics of each three-channel operator have been presented in Appendix III. Note that when deriving these operators, one-dimensional correlation functions were estimated directly from each 1224×1224 image; the correlation data derived from the 1024×1024 subscenes described in Section 4.3 were not used. Inspection of the diagrams in Appendix III will once more verify that the frequency response magnitudes are not constrained to be identical. In fact, for these operators, the differences between channels are much more pronounced than was observed for filters derived with Case I correlation data. This is due to the shape-altering influences which the α and β parameters exert in the presence of Case II correlation data. Results obtained from the filtering operations will now be discussed.

4.4.2 Comparison of Unfiltered and Filtered Image Processes for Nov. 14

The unfiltered signal-plus-noise process for the Nov. 14 image is shown in Figure 4.9(a); the presence of a noise process is evident, and interferes with any attempt to visually assess the structure of the underlying wavefield. Despite this however, it is possible to observe a wavefield component which has its major axis oriented at 10° CCW from vertical. This

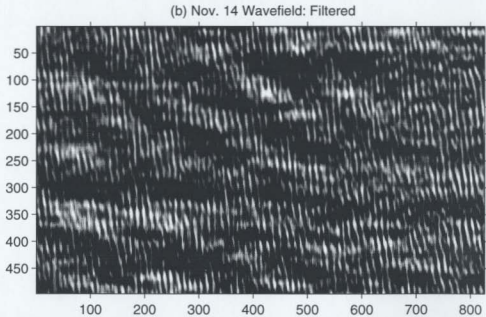
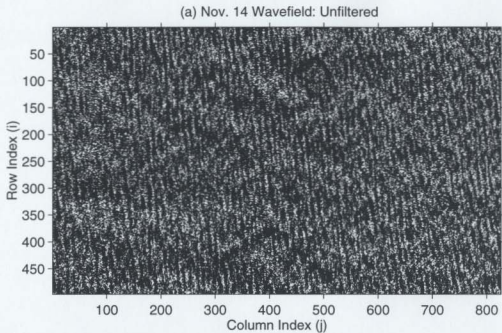


Figure 4.9: Noise-contaminated SAR image is shown in (a), for Nov. 14 wavefield. The recovered wavefield, based on standard-attribute operator with $\alpha=\beta=3$, $\xi=200$, is shown in (b).

component was previously identified in conjunction with the two-dimensional ACF discussed in Section 4.3.1. However, from that ACF data it is also known that there exists other wavefields, one of which has its major-axis orientation at approximately 30° CCW from vertical. At best, this wavefield can only be described as being barely observable in Figure 4.9(a). In fact, it is only slightly noticeable in the upper central region of the image, and then only to a trained eye. Had its presence not been revealed by the two-dimensional ACF, this wavefield probably would go unnoticed during a visual inspection of the unfiltered image. A third possible wavefield, oriented at 90° CCW from vertical as suggested by the ACF in Figure 4.3, cannot be detected.

Results of the vector filtering operation involving the Nov. 14 image, are displayed in Figure 4.9(b). From this image, it is seen that the speckling effect of the correlated noise in Figure 4.9(a) has been eliminated, at least to such an extent that it cannot be detected visually. As a direct consequence, the 10° wavefield is now more clearly observable. As well, the 30° wavefield also appears with an enhanced visibility which is far superior to its presentation in Figure 4.9(a). This enhancement is actually due to the exponentially-damped nature of the ACF; because the filter is performing a three-step prediction, the damping of the ACF has probably altered the power relationships within the output spectra. Hence, the filtering operation imparts a disproportionate amount of power to this wavefield, when compared to the relationships which existed previously. Furthermore, the wavefield which has a 90° CCW orientation, previously indicated by the ACF in Figure 4.3, can now be partially detected. This feature is best observed in the extreme left and right regions of the image, especially in the lower half portion; its emergence is also likely due to the shift of power towards lower frequency components, as a result of the filtering operation.

A close visual assessment of the enhancement provided by filtering can be made with reference to Figures 4.10(a) and 4.10(b), which present enlarged subscenes from the lower right regions of the images in Figure 4.9. At this scale, of course, sufficient information for making

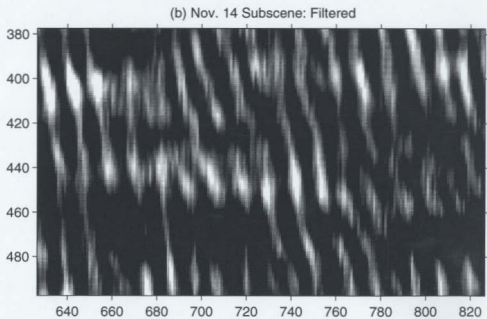
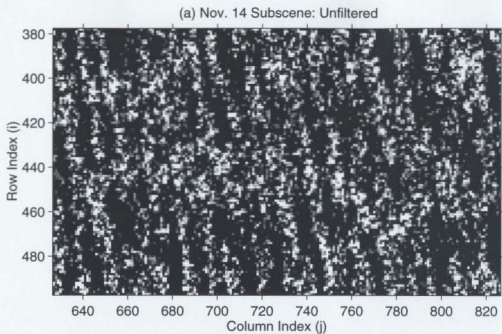


Figure 4.10: Enlarged subscenes from the unfiltered and filtered images in Figure 4.9.

comparisons can only be provided for the wavefield which is oriented at 10° CCW from vertical. As seen in Figure 4.10(a), the elongated pattern produced by the unfiltered wave crests is noticeable overall, but the individual waves are not easily discerned; this is due to perturbations of their geometry, which have been imposed by the noise. However, from Figure 4.10(b), it is seen that the wave crests become clearly visible after the filtering operation has been performed. Furthermore, very careful comparisons will yield positional and geometrical correspondences, between each filtered wave feature in Figure 4.10(b) and its related noise-perturbed feature in Figure 4.10(a). Based on a purely visual assessment, it is possible to conclude that the filtering operation yields convincing results.

Frequency-domain representations of the unfiltered and filtered images for Nov. 14, are shown in Figure 4.11. In particular, Figures 4.11(a) and 4.11(b) show the signal-plus-noise spectra from the row and column components of the unfiltered image. In both cases, there exists clear evidence of a tapered noise spectrum, consistent with earlier observations that the noise is significantly correlated at non-zero lags. For the row component, it is apparent that there exists two dominant frequency bands, one at about $f=\pm 0.2$, and another which occurs in the region around $f=0$. These two frequency bands within the row component correspond to the image wavefields which are oriented at 10° and 30° respectively. It should also be noted that the apparent peak at $f=0$ is actually two peaks, representing the positive and negative components of a frequency which is very close to DC; here, the spacing is so small that it cannot be resolved by the plotting device. This feature is possibly due to the 90° wavefield discussed previously; because of its orientation in the image, its row component would have a frequency which is very close to DC. For the column component, shown in Figure 4.11(b), it is seen that there exists only one band of frequencies for which there is noticeably greater power. This occurs in the approximate range of $-0.1 \leq f \leq 0.1$, and it is not surprising, since the two-dimensional ACF of Figure 4.3 indicates that all wavefields are of very low frequency in the column dimension. As a further comment,

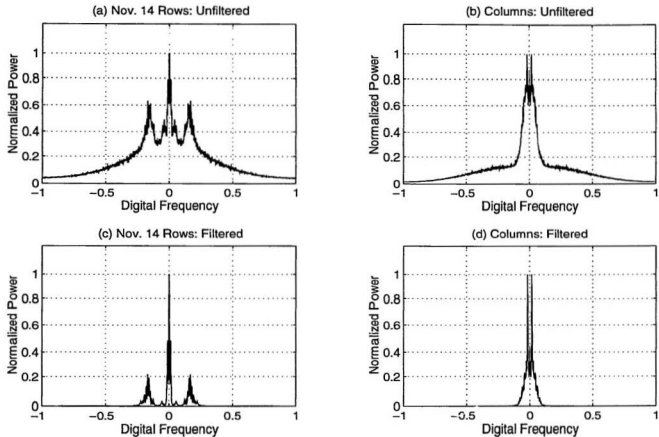


Figure 4.11: 1024-point FFT's, for the row and column components of the unfiltered and filtered images shown in Figure 4.9.

note that since the ACF of these processes is exponentially-damped in both the row and column dimensions, it is to be expected that the desired signal actually has a spectral content which spans all digital frequencies $-1 < f \leq 1$. However, outside of the bands just identified, the signal contribution to the spectrum is insignificant in comparison to the power contributed by noise, and will never be recovered.

Figures 4.11(c) and 4.11(d) display the row and column spectra which were recovered by filtering the noisy image. The bandwidths which emerge from this operation are a result of the filter having adapted to the signal component of the image, for those values of α and β which were chosen. These bandwidths then, are considered to be the effective bandwidths of the signal process; in actual fact, they have been defined by that particular realization of Wold's decomposition which is associated with the chosen filter parameters. From Figure 4.11(c), it is seen that the recovered signal in the rows, has spectral peaks corresponding to those which were identified in Figure 4.11(a); however, there is certainly detectable power for all frequencies within the range of $-0.2 \leq f \leq 0.2$, thus establishing the effective bandwidth as spanning this range. From Figure 4.11(c), it might initially seem that the low powers which occur in the trough at about $f = \pm 0.1$, could possibly be remnant noise; however, based on the correlation plots of Figure 4.8, it is almost certain that the forward prediction and cross-channel gaps are sufficient for elimination of the noise component. Therefore, it must be concluded that the frequency powers occurring in these troughs also belong to the bandpass process. For the output spectra from the columns, seen in Figure 4.11(d), it is easy to conclude that the effective bandwidth is approximately $-0.1 \leq f \leq 0.1$, a range which corresponds to the spread already inferred from the noisy image. These observations are verified by the row and column power transfer functions which are shown in Figures 4.12(a) and 4.12(b). With reference to the definition of $T_r(f)$ via Eq. (3.2), the noisy image spectrum corresponds to $P_{NIN}(f)$, whereas the filtered output spectra correspond to $P_{NFIN}(f)$. In these Figures, it is seen that all of the positive gain factors coincide with frequencies occurring

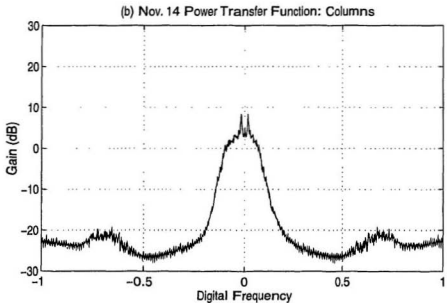
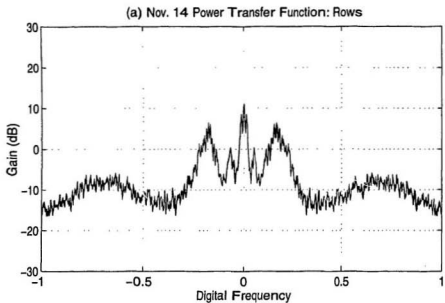


Figure 4.12: Power transfer functions, mapping unfiltered row and column spectra to their respective filtered spectra, for Nov. 14 image.

within the ranges just defined. In particular, it is seen that the noise frequencies which occur outside of these effective bandwidths experience attenuation factors in the range of -8 dB to -28 dB.

A very important observation which can be made when comparing the unfiltered normalized spectra to their filtered counterparts, is that the power relationships within the effective bandwidths are changed as a result of the filtering. For instance, comparison of Figure 4.11(c) with Figure 4.11(a) will reveal that the higher frequency component within the rows, at about $f=\pm 0.2$, has experienced a loss of power relative to the components which occur near $f=0$. Similarly, comparison of Figures 4.11(d) and 4.11(b) shows that almost all frequencies in the bandwidth of $-0.1 \leq f \leq 0.1$ have experienced a loss of power, except for two frequency points which have emerged to dominate the spectrum after filtering. In fact, for both the row and column filtered spectra, it is the lower-frequency components which have gained a relative power advantage within the signal bandwidth. The power transfer functions of Figure 4.12 confirm that there has been a redistribution of power. In these diagrams it is clear that the positive gain factors are not constant across the signal bandwidths; in fact, the gain factors are generally largest for frequencies near DC. This verifies that some spectral components within the desired signal must have experienced a power increase relative to the power of other frequencies within the effective bandwidth. Further to this, it is seen that within the effective bandwidth of the rows, some frequencies have actually experienced attenuations close to -10 dB. Such observations explain why the 30° wavefield, as well as the 90° wavefield, have become more visually dominant in the filtered image than they had previously been in the unfiltered version.

4.4.3 Comparison of Unfiltered and Filtered Image Processes for Nov. 18

The unfiltered signal-plus-noise process for the Nov. 18 image is shown in Figure 4.13(a). Here too, the presence of noise is obvious and interferes with any attempt to either

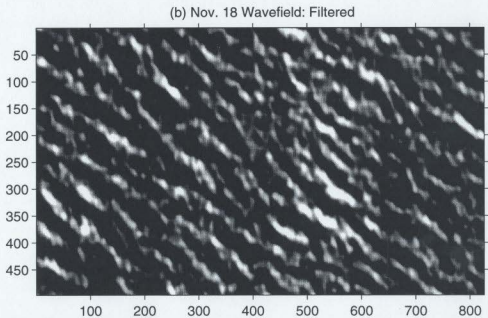
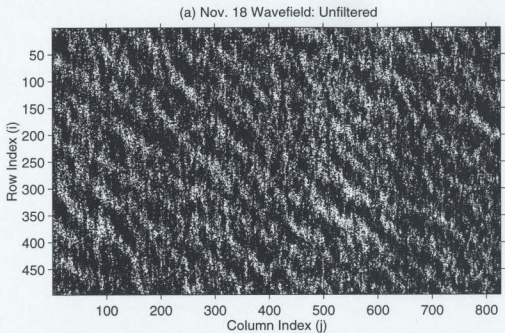


Figure 4.13: Noise-contaminated SAR image is shown in (a), for the Nov. 18 wavefield. The recovered wavefield, based on standard-attribute operator with $\alpha=\beta=3$, $\xi=200$, is shown in (b).

visually or numerically characterize the wavefield structure. In this image there apparently exists a single dominant wavefield oriented at 45° CCW from vertical, as predicted by the patterns observed in the two-dimensional ACF of Figure 4.4(b). A second possible wavefield oriented at approximately 140° CCW from vertical, which was suggested by the correlation information in Figure 4.4(b), cannot be observed. A recovered image obtained via the vector filtering operation is presented in Figure 4.13(b); as with the previous filtering results, this image also suggests a complete absence of visually detectable noise components.

Inspection of enlarged subscenes shown in Figures 4.14(a) and 4.14(b), indicate that there is a strong positional correspondence between the filtered structures and their unfiltered counterparts. Furthermore, while the filtered structures are certainly more crisply defined, there also exists a definite geometric correspondence to their diffuse, noise-perturbed versions, which are seen in the unfiltered image. This provides strong empirical evidence, to indicate that the filtering technique has recovered a reasonably accurate facsimile of the wavefield while successfully annulling the distortions due to correlated noise. As a further comment, note also that the filtered image in Figure 4.13(b) yields no visual evidence to indicate the presence of any wavefield oriented at 140° CCW from vertical.

Frequency-domain characteristics of the row and column components from the Nov. 18 image, are shown in Figure 4.15. Inspection of the unfiltered spectra in Figures 4.15(a) and 4.15(b) suggests that the noise power is lower in relation to the signal power, than was the case for the Nov. 14 image. From the filtered spectra, in Figures 4.15(c) and 4.15(d), it is seen that the effective bandwidth of the signal process within both the row and column components of the image is approximately $-0.1 \leq f \leq 0.1$. This equality in bandwidths between row and column dimensions, is consistent with the fact that the dominant wavefield is oriented at an angle of approximately 45° CCW from vertical. These same approximate bandwidths can also be observed in the unfiltered spectra. However, when making comparisons between the spectra, it is clear that

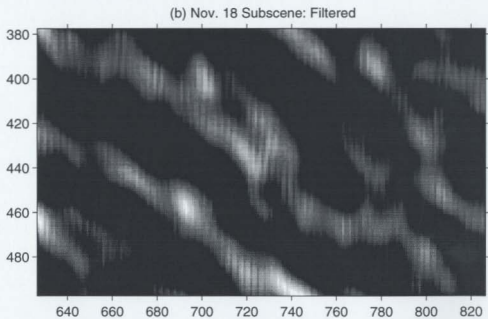
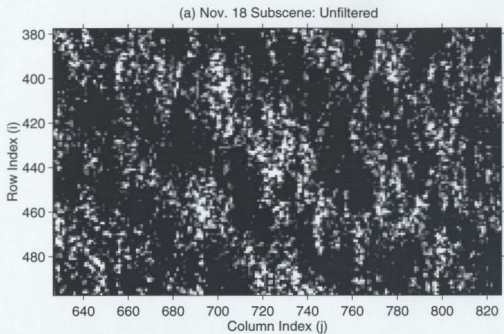


Figure 4.14: Enlarged subscenes from the unfiltered and filtered images in Figure 4.13.

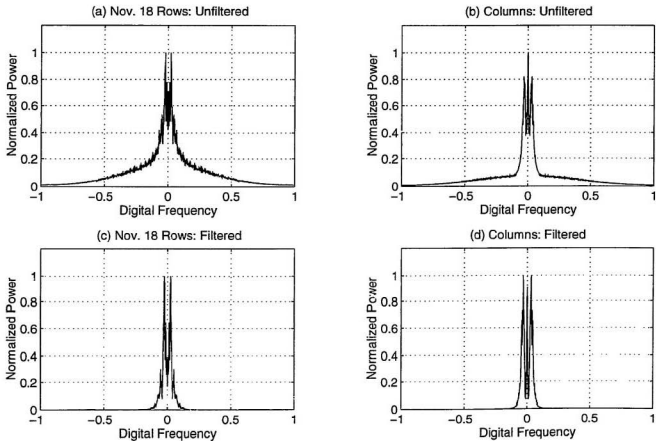


Figure 4.15: 1024-point FFT's, for the row and column components of the unfiltered and filtered images shown in Figure 4.13.

the filtering operation has resulted in a redistribution of power within the effective bandwidths. A notable example occurs within the column component, shown in Figure 4.15(b), where the unfiltered spectrum reveals the presence of a notch at frequencies near $f=0$; in the filtered spectrum, however, seen in Figure 4.15(d), it is clear that this notch has deepened considerably. These observations may also be confirmed by reference to the power transfer functions which are shown in Figure 4.16. Here, it is seen that the positive gain factors are not equal within the effective bandwidths of the signal, and in fact, the notch which deepens in the bandwidth of the column component, actually corresponds to a negative gain within the power transfer function; this is similar to the effect observed for the row transfer function of the Nov. 14 image. These non-uniform gain factors confirm that the signal is distorted during the filtering operation. However, the power transfer function also reveals that the noise components which lie outside of the effective bandwidth experience attenuation factors having magnitudes within the range of -10 dB to -25 dB.

4.5 Summary

In this Chapter, the vector filtering technique has been applied to two images, each of which contained a bandpass stochastic process contaminated by correlated noise. This underlying process was characterized by Case II correlation functions which exhibited noticeable damping. By inspection of the one-dimensional row and column ACF's, it was possible to establish that the noise was correlated to a spatial extent which is equivalent to $c=2$ in Eq. (2.11). This required that the vector Wiener filter be derived with parametric values of $\alpha=3$ and $\beta=3$. Inspection of two-dimensional autocorrelation surfaces, indicated that an operator length of $\xi=200$ would incorporate sufficient information for recovery of these noise-perturbed wavefields.

Filtering operations performed on the two images indicate that it is indeed possible to recover a noise-suppressed wavefield. Within this wavefield, the smoothed wave features will

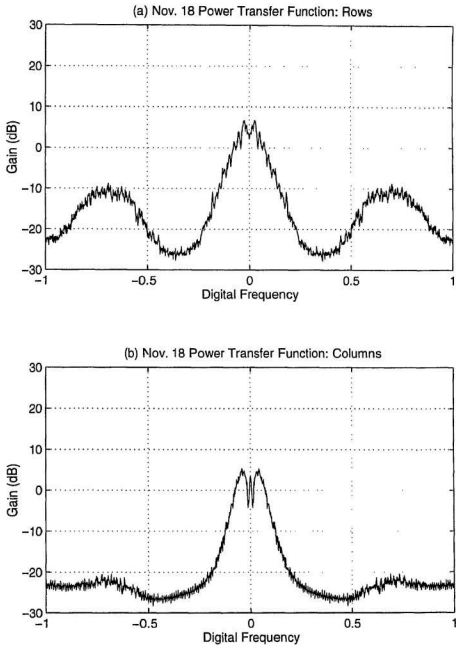


Figure 4.16: Power transfer functions, mapping unfiltered row and column spectra to their respective filtered spectra, for Nov. 18 image.

retain an observable geometric correspondence, when compared to their diffuse, noise-perturbed counterparts in the unfiltered images. However, examination of power spectra and power transfer functions, indicates that some signal frequencies within the recovered images have experienced a significant gain in comparison to other spectral components within the desired signal. This phenomenon arises due to the exponentially-damped nature of the correlation data, and has been predicted by the analytical representations discussed in Chapter Two. The next Chapter will present a detailed investigation as to how this problem might become further intensified, in filtering situations for which larger values of α and β may be required.

CHAPTER FIVE

INFLUENCE OF WOLD'S DECOMPOSITION UPON VECTOR FILTER FOR CASE II CORRELATION DATA

5.1 Introduction

During the mathematical discussions in Chapter Two, it was shown that for Case II correlation data, the scalar Wiener filter would produce a different realization of Wold's decomposition, for each unique combination of values assigned to the forward prediction and cross-channel prediction parameters, α and β . Hence, for two different combinations of α and β , the corresponding scalar Wiener filters would produce different recovered wavefields after operating on the same noise-contaminated image. This Chapter will provide empirical evidence that Wold's decomposition has a similar effect upon the three-channel version of the vector Wiener filter as well. Such influences were suggested at the beginning of Section 2.6.2, but analytical proofs were beyond the scope of this project. As a further comment, from the mathematical formulations of Chapter Two, and with particular reference to Eq. (2.21), it can be seen that the filter length, ξ , will also be influential in determining the representation accuracy of the recovered wavefield. However, this fact will not be investigated here because it is an already well-known attribute of linear prediction theory.

In addition, this Chapter will present further evidence to confirm that the exponentially-damped Case II models of Chapter Two, are representative of the correlation and spectral characteristics for processes within the Nov. 14 and Nov. 18 images. Such verification will be a necessary step, towards evaluating and explaining the influence which Wold's decomposition exerts upon filter performance in the three-channel case. This study will focus on the use of α and

β parameters which are of much greater magnitudes than those which were used in Chapter Four. Such an investigation has practical significance for potential filtering situations in which the extent of spatial correlation exceeds $c=2$, this having been the value established for operations in the previous Chapter.

5.2 Cross-Coherence Functions Obtained from Nov. 14 and Nov. 18 Images

The cross-spectral magnitude coherence function, $\gamma_{xy}^2(f|\theta,\beta)$, was previously defined via Eq. (2.22) in Section 2.4.3.2. There, it was asserted that for Case II correlation data, the cross-spectral magnitude coherence would change as a function of β , when computed from the one-sided power spectrum at $\alpha=0$. This fact provides a good measure against which to verify the presence of Case II data within the SAR images discussed in Chapter Four. Pursuant to this, numerical estimates of the coherence function were obtained from the unfiltered Nov. 14 and Nov. 18 images, for $1 \leq \beta \leq 50$ and $\alpha=0$. Implicit to $\gamma_{xy}^2(f|\theta,\beta)$, via Eq. (2.20) and Eq. (2.22), is the value for ξ , which was chosen to be 256 in this case. The choice of $\xi=256$ involves an integral power of 2, 2^8 in fact, which greatly improves the computational efficiency of the FFT algorithms required for numerical estimation of $\gamma_{xy}^2(f|\theta,\beta)$. A detailed discussion of the estimation procedure may be found in [31]. Essentially, with each pair of 1224-point rows, $\gamma_{xy}^2(f|\theta,\beta)$ was computed for several segment pairs, each of 256 points per segment, and each of which overlapped with the previous segment pair by 210 points. At each value of β , this procedure was performed for all row pairs occurring in the image, after which the resulting ensemble was averaged to produce the estimate of $\gamma_{xy}^2(f|\theta,\beta)$. The numerically-averaged results for fifty positive values of β are shown in Figure 5.1. These surfaces display the regional average of $\gamma_{xy}^2(f|\theta,\beta)$, which has been computed over all row pairs separated by each specified distance of β . In order to enhance the clarity of presentation, these surfaces show results only for $0 \leq f \leq 0.5$; for both images, the effective

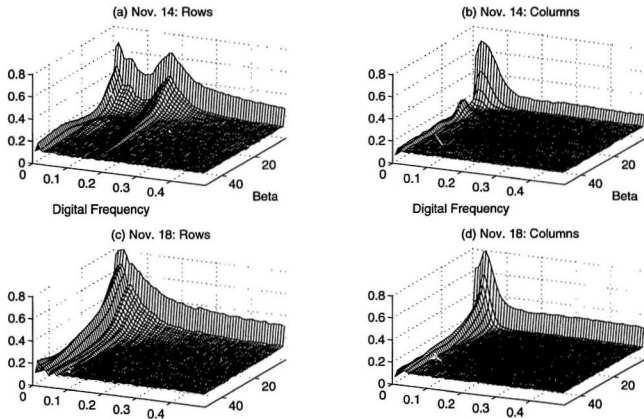


Figure 5.1: Numerical estimates of $\gamma_v^2(f|\theta, \beta)$, $1 \leq \beta \leq 50$, obtained from the Nov. 14 and Nov. 18 SAR images.

bandwidths of the row and column bandpass processes occur within this range, hence, very little information has been lost by omitting the upper half of the spectrum.

Upon inspection of these surfaces, it is clear that they all share a common attribute in the form of a "curtain" of spectral correlation at $\beta=1$. At this value of β , the correlation coefficient for each frequency point is much higher than the coefficient at each corresponding point for $2 \leq \beta \leq 5\theta$. This is due to the additive noise component, which is known to be correlated across rows which are separated by a distance of $\beta=1$. However, overall higher coefficients for $\beta=2$ are not apparent, despite the fact that results of the previous Chapter showed the noise to be correlated across rows which are separated by this distance as well. This discrepancy is likely due to the fact that the surfaces were estimated using much shorter data lengths, a necessity for periodogram averaging of spectra. Because of this, the cross-coherence surfaces of Figure 5.1 will be insensitive to the much weaker noise correlation known to exist at $\beta=2$.

A second attribute which is common to all four surfaces, is that for the bandpass signal component, the correlation power at larger values of β is much lower than at smaller values of this parameter. In fact, with respect to the bandpass component at about $f = 0.2$ in Figure 5.1(a), it is seen that for $\beta > 4\theta$, the correlation power is not significantly greater than the coherence estimate for noise frequencies at $\beta > 1$. Such a loss in signal correlation power would be consistent with the exponential decay of cross-spectral power within a Case II process, for increasing β , as predicted by $G_{\nu}(f|0,\beta)$ in Eq. (2.20). This is further evidence that the spectral model for Case II correlation data, as defined by Eq. (2.20), aptly represents the spectral processes which are found in these images.

There is also a third significant attribute which is observed to be present in Figure 5.1(b) and, to a lesser extent, in Figure 5.1(a). With specific reference to the bandpass component of Figure 5.1(b), for $0 \leq f \leq 0.1$, it is seen that the correlation power decreases rapidly while β is in the approximate range of $1 \leq \beta \leq 6$, however it increases once more, in a cyclical pattern, for

$6 < \beta \leq 15$; there also appears to be another very weak cycle in the approximate range of $15 < \beta \leq 30$. This pattern would also be consistent with the exponential decay of a cyclical $G_w(f|\theta, \beta)$ in the numerator of $\gamma_{xy}^2(f|\theta, \beta)$, as β continued to increase. For any fixed value of f and increasing β , such a pattern would occur due to the cyclic nature of the complex resultant which arises from the addition of n non-zero spectral terms in Eq. (2.20). In fact, such a pattern was specifically predicted during the discussion which pertained to that equation. A similar pattern, of much lower correlation power, can be observed from Figure 5.1(a), within the region bounded by $0 \leq f \leq 0.1$ and $1 \leq \beta \leq 50$. Consequently, based on these observations, as well as the discussion of the preceding paragraphs, and taking into account the apparently damped shape of the correlation functions in Chapter Four, it is now possible to reach a significant conclusion which was only alluded to in the previous Chapter. Specifically, for both the Nov. 14 and Nov. 18 unfiltered images, correlation data obtained from the time domain, as well as from the frequency domain, exhibit characteristics which are predicted by the analytical models defining Case II correlation conditions. In fact, no evidence whatsoever has been observed which would support any assertions to the contrary.

Given that Case II correlation conditions exist for the images which were processed in Chapter Four, it is now important to recall certain statements which were made in Chapter Two, regarding the role of Wold's decomposition in the filtering process. There, it was stated that the scalar Wiener filter would yield different realizations of Wold's decomposition, each distinct, and each corresponding to a specific combination of values for α and β , if Case II correlation data were used in the filter derivation. While this characteristic was not demonstrated analytically for the vector version, it follows that since the principles of vector Wiener filtering are an extension of the scalar case, then similar behaviour can be expected for the three-channel filter. This now prompts recognition that the recovered images shown in Chapter Four, represent but one of a range of possible realizations of Wold's decomposition. Hence, the wavefields shown in Figures

4.9, 4.10, 4.13, and 4.14 are not unique representations of the bandpass components occurring within the original images.

Furthermore, it also follows that since the lower limits of α and β are determined by the upper limit of c , then the actual extent of noise correlation will predetermine which realizations are recoverable from Case II data. Given this, it would now seem that the most accurate representations will be recovered when the spatial extent of noise correlation is small. This is because for small values of α and β , the differing rates of exponential decay between the n sinusoidal components of the CCF, will not be as influential as they would for larger values of α and β . Moreover, small parametric values will impose only minor relative displacements between z -plane positions of the n complex phasors which comprise Eq. (2.20). These two factors imply that the frequency response of the filter will not depart severely from the frequency characteristics of the bandpass process within the noisy image, when α and β are small. This assertion is supported by the fact that close positional and geometrical correspondences were observed between features occurring in the unfiltered and filtered images presented in Chapter Four. Conversely, for large α and β , exponential attenuation will be so severe that some frequency components may be virtually eliminated. As well, the severity of relative phasor displacements in the z -plane will increase and decrease cyclically within $G_v(f|\alpha,\beta)$, as either one of these parameters increases without bound. These influences will severely alter the frequency response characteristics of the filter, thereby distorting the wavefield which occurs in the output image. Therefore, it is quite reasonable to expect a decrease in filtering accuracy, for Case II situations in which the extent of noise correlation forces the choice of large parametric values. To investigate the validity of these observations, the frequency magnitude response of the three-channel filter will now be examined over a range of values for α and β .

5.3 Magnitude Response Variations Induced by Changing α and β

To provide verification that vector filter characteristics will rely heavily upon variations in α and β for Case II correlation data, a series of numerical investigations were conducted. These involved the derivation of three-channel transfer functions, for chosen ranges of the shape parameters; all derivations involved standard-attribute operators having a value of $\xi=200$. One set of derivations involved a fixed value of $\beta=3$, while α was incrementally adjusted between each individual derivation, within the range of $3 \leq \alpha \leq 50$. A second set of three-channel transfer functions were derived by setting $\beta=\alpha$ for all derivations, and jointly incrementing these values within the range of $3 \leq (\alpha=\beta) \leq 50$. This procedure was implemented for row and column correlation data obtained from both of the unfiltered Nov. 14 and Nov. 18 images. An extensive data set was produced, which need not be examined in detail, since the prime objective is merely to demonstrate that variability in filter response does occur as a function of the shape parameters. Consequently, only the results from column filters for the Nov. 14 image have been displayed in Figures 5.2 and 5.3; similar results for the row filters of this image, as well as the row and column filters of the Nov. 18 image, may be found in Appendix IV. Furthermore, each surface within Figures 5.2 and 5.3 has been normalized such that its maximum response assumes a magnitude of unity. Therefore, magnitude response comparisons between surfaces are not meaningful; however, the surfaces in Appendix IV have not been subjected to any such normalization.

Figures 5.2(a), 5.2(b) and 5.2(c) show the respective frequency response surfaces of transfer functions h_{21} , h_{22} , and h_{23} , for $\beta=3$ and varying α . Similarly, Figures 5.3(a), 5.3(b), and 5.3(c) show the responses of these transfer functions for jointly varying values of $\beta=\alpha$. Inspection of these surfaces, will yield unequivocal evidence that the filter responses do vary significantly with changes in the shape parameters. This confirms that the recovered images presented in Chapter Four are not unique representations of the bandpass processes occurring in the noisy

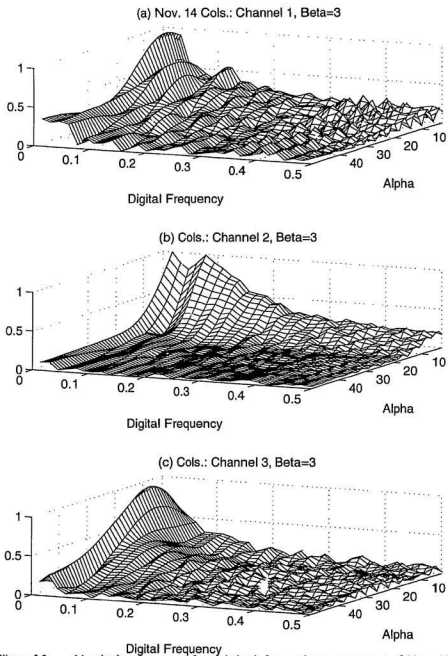


Figure 5.2: Magnitude response surfaces derived from column component of Nov. 14 image, for fixed β and varying α . Note the cyclic patterns parallel to the α -axis.

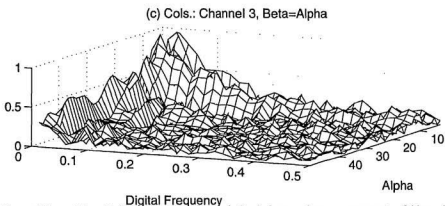
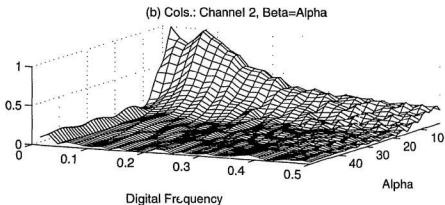
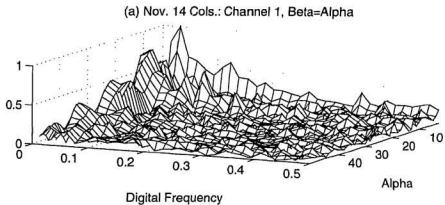


Figure 5.3: Magnitude response surfaces derived from column component of Nov. 14 image, for jointly varying $\beta = \alpha$.

images. As well, Figures 5.2(a) and 5.2(c) show a clearly cyclical pattern in the cross-channel response of each frequency point, for increasing α . If one considers the scalar Wiener filter analogy of Eq. (2.40), it is apparent that such a pattern could only occur if $G_v(f|\alpha, \beta)$ were derived from Case II correlation data. This pattern is also evident, to a slightly lesser degree, in the response for h_{22} shown in Figure 5.2(b). For the response surfaces corresponding to jointly varying $\beta=\alpha$, a similar pattern is also evident in the response for h_{22} shown in Figure 5.3(b); however, for h_{21} and h_{23} in this case, shown in Figures 5.3(a) and 5.3(c), there is only very slight evidence of such a pattern, restricted to frequency points of $\theta \leq f \leq 0.1$.

As a general comment, which pertains to all response surfaces shown in Appendix IV, the occurrence of cyclical frequency response is less prevalent for jointly varying $\beta=\alpha$ than for fixed β with varying α . This may be partly due to the variability which occurs with the introduction of new CCF data as β varies, a fact which was discussed in conjunction with similar response surfaces for Case I correlation data in Section 3.4.2. However, for Case II, a more compelling explanation logically follows from the form of Eq. (2.20), which indicates that changing β in conjunction with changing α will destroy the periodicity which occurs with advancing α . This is because the exponential terms involving $\omega_k \beta$ will also introduce new phase relationships with each change in β . Hence, with Case II data, there is an analytical basis for explaining the loss of periodicity in the cross-channel frequency response for jointly varying $\beta=\alpha$. Further to this, the fact that cyclic behaviour can still be observed for h_{22} in Figure 5.3(b), suggests that the within-channel transfer function for this three-channel set behaves somewhat like its scalar counterpart in Eq. (2.40). If, for instance, the form of Eq. (2.40) is considered within the role of the three-channel scalar array proposed in Eq. (2.45), it is realized that this version of h_{22} would only incorporate $G_v(f|\alpha, \theta)$ in the numerator of its frequency-domain representation. However, within this array, the frequency-domain representations of h_{21} and h_{23} would incorporate only $G_v(f|\alpha, -\beta)$ and $G_v(f|\alpha, \beta)$ respectively. Since β would be equal to zero and constant over all

α for the version of h_{22} , represented by Eq. (2.40), it is easy to see that a jointly varying $\beta=\alpha$ would only influence the response of h_{21} and h_{23} ; hence, the cyclic response of h_{22} would remain unaltered. The patterns observed in Figures 5.3(a), 5.3(b), and 5.3(c) are consistent with the existence of a similar relationship between the transfer functions of the three-channel vector filter.

However, this is not to imply that the three-channel vector version is equivalent to the scalar arrangement of Eq. (2.45); for instance, the vector version incorporates correlation information between rows $i-\beta$ and $i+\beta$, whereas the scalar functions of Eq. (2.45) definitely do not. As well, the surfaces in Appendix IV indicate that the Channel 2 response generally does exhibit some change with $\beta=\alpha$, when compared to its response for fixed β . Hence, changing β does influence the Channel 2 filter; overall however, the changes within h_{22} are *minimal* in comparison to the changes which occur within h_{21} and h_{23} . Based on these observations, it is possible to conclude that while autocorrelation and cross-correlation data contribute to the frequency response of all three filters, autocorrelation data is most influential in shaping the response of h_{22} ; conversely, it would appear that cross-correlation data is dominant in determining the frequency characteristics of h_{21} and h_{23} .

The surfaces in Figure 5.2 reveal another interesting pattern, which also requires some explanation. By inspection, it is clear that the frequency of cycles which occur due to advancing α , at any given f , increases with the value of f . Hence, for f close to 0.1 say, the magnitude response exhibits only a small number of cycles for $3 \leq \alpha \leq 50$. However, as f approaches 0.5, the number of cycles increases noticeably. This suggests that the number of cycles which α introduces to the magnitude response, is somehow proportional to the value of f . To understand the source of this phenomenon, consider a modified and approximate version of the *scalar* transfer function, now represented as $H_{21}(\alpha|f)$, which has as its domain, the values occurring along the α -axis of the surfaces in Figure 5.2; such a function will be defined as :

$$H_{xy}(\alpha|f) = \frac{G_{xy}(\alpha|f)}{G_{xx}(f) + N_{xx}(f)} \quad (5.1)$$

$$= \left\{ \frac{1}{G_{xx}(f) + N_{xx}(f)} \right\} \times \left\{ \sum_{k=1}^n e^{-j[2\omega_{kk} \cdot f - \omega_{kk}]} \frac{\sinh\{d_{kR}\xi/2\}}{\sinh\{(d_{kR} + j\omega_{kk} - jf)/2\}} \right\}$$

This representation excludes several terms which are present in Eq. (2.20). However, by momentarily assuming that these terms are uninfluential, it is possible to understand the changing frequency of the α -induced cycles in Figure 5.2. To begin, consider the case where n is large in Eq. (5.1), such that for *each* value of f in the DFT, the correlation function incorporates a corresponding sinusoidal component of frequency ω_{kk} . Consider next, an arbitrary frequency point, f_o , say, at which Eq. (5.1) will be evaluated over all α . Although it will not be formally shown, it can be numerically verified that as $\omega_{kk} \rightarrow f_o$, from either the right or left, the *magnitude* of the quotient of *sinh* functions increases in a highly non-linear fashion and peaks quite suddenly when $\omega_{kk} = f_o$. This has significant ramifications for the behaviour of $H_{xy}(\alpha|f=f_o)$ when the summation is carried out within Eq. (5.1). In particular, consider the n cyclic series which are generated at f_o as α increases without bound. From the form of Eq. (5.1), it is known that each k 'th series will have a unique frequency of ω_{kk} , $k=1,2,\dots,n$. Point-wise summation of these n series, each of a different cyclic frequency, defines the frequency response *series* of $H_{xy}(\alpha|f=f_o)$ at specified frequency f_o , over a specified domain of α , in this case $3 \leq \alpha \leq 50$. However, due to the behaviour of the quotient of *sinh* functions in Eq. (5.1), the most powerful cyclic series within in this point-wise summation will be the series for which $\omega_{kk}=f_o$. Therefore, the dominant frequency of α -induced cycles at DFT point f_o , is in fact, f_o . Based on this discussion, it now follows in general that for any frequency point, f , cyclic variations in $H_{xy}(\alpha|f)$ must occur with a dominant frequency which in fact is equivalent to f . This helps to explain the changing frequency of cyclic patterns observed in Figure 5.2; however, in these surfaces, the influence of exponential damping factors will also play a role.

An overall comment which can be made regarding the frequency response surfaces in Appendix IV, is that existence of cyclic behaviour, while present in most, is generally much less pronounced for row transfer functions, regardless of whether β is fixed or varying. Another general conclusion, is that as α increases, the decay in magnitude response is much more severe for column transfer functions than for row transfer functions. These observed differences are consistent with statements made in Section 4.2, wherein it was revealed that the process by which image rows were constructed was different from that by which the columns were formed.

Based on information presented in this Section, it is now conclusive that with Case II correlation data, the frequency response of the vector filter is dependent upon the values which are chosen for α and β . Therefore, each choice of α and β does yield a different realization of Wold's decomposition; visual evidence in support of this will now be examined.

5.4 Assessment of Recovered Images for Impact Due to Changes in α and β

To further emphasize the findings of the previous Section, a set of recovered wavefields was generated by filtering the Nov. 14 and Nov. 18 images, using a standard-attribute operator with $\xi=200$. Complementary to the recovered images of the previous Chapter, four additional process realizations were obtained from each noisy image by deriving filters based on four unique combinations of values for parameters α and β . An FFT analysis, for $-0.25 \leq f \leq 0.25$, performed on the rows and columns of each of these images, has been presented in Appendix V; FFT results from the filtered images in Chapter Four have also been included.

Results obtained from the Nov. 14 image, for parametric combinations $(\alpha, \beta) = (15, 3)$ and $(\alpha, \beta) = (27, 3)$, are shown in Figures 5.4(b) and 5.4(c) respectively; for comparison purposes, Figure 5.4(a) presents the recovered wavefield which was previously obtained in Chapter Four, with $(\alpha, \beta) = (3, 3)$. Based on these wavefields, it is clear that the 10^p wavefield component of the Nov. 14 image experiences significant attenuation as α increases in magnitude, for a constant β .

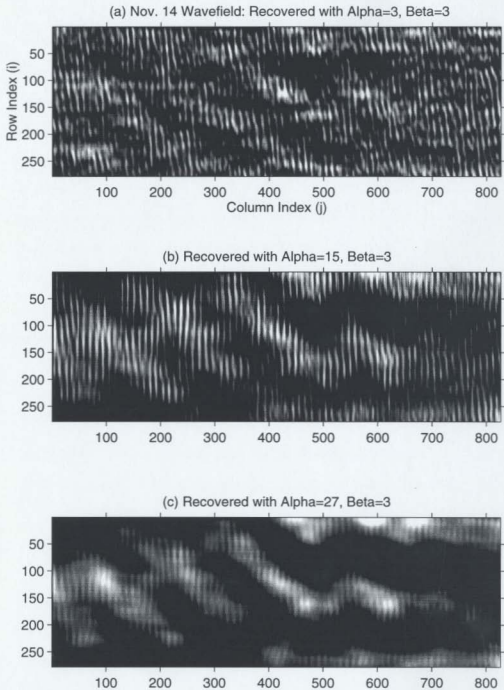


Figure 5.4: Realizations of Nov. 14 bandpass process for $\beta=3$, at three distinct values of α .

For $(\alpha, \beta)=(15, 3)$, shown in Figure 5.4(b), this higher-frequency wavefield is still highly visible, however, it is also clear that the lower frequency wavefield at 30° orientation has become more dominant in comparison to Figure 5.4(a). Furthermore, the actual shape of features which comprise the 10° wavefield component is now much more regular than for the case in which $(\alpha, \beta)=(3, 3)$. This suggests that the significant bandwidth associated with this 10° component has narrowed due to the increase in α ; a fact which can be verified by reference to the FFT analysis in Appendix V. In Figure 5.4(c), with $(\alpha, \beta)=(27, 3)$, it is seen that the 30° wavefield has been even further enhanced, with only a slight trace of the 10° wavefield remaining. In addition to this, the right portion of the image apparently displays a portion of the wavefield which is oriented at 90° CCW from vertical. As suggested by the discussion pertaining to the two-dimensional ACF in Figure 4.3(a), this wavefield has emerged only after the other wavefield components have experienced a significant attenuation of power, which resulted from the filtering operation.

Figure 5.5 presents a second set of process realizations, obtained from the Nov. 14 image by using parametric values of $(\alpha, \beta)=(15, 15)$ and $(\alpha, \beta)=(27, 27)$. These are shown in Figures 5.5(b) and 5.5(c) respectively, with the reference process due to $(\alpha, \beta)=(3, 3)$, shown in Figure 5.5(a). For both Figures 5.5(b) and 5.5(c), the 30° wavefield is totally dominant and the 10° wavefield is virtually absent. These results are in contrast to the results in Figure 5.4, where the 30° wavefield was less well-defined overall. The mechanism by which the 30° wavefield undergoes significant enhancement during recovery of Figures 5.5(b) and 5.5(c), can be inferred by examining the spectral magnitude cross-coherence functions shown in Figure 5.1. With particular reference to Figure 5.1(a), it is seen that as β increases, the cross-row spectral correlation power decays much more rapidly for the higher frequency bandpass component than for the lower frequency bandpass component. This relationship means that for a vector filter derived with $(\alpha, \beta)=(15, 15)$ or $(27, 27)$, the filtered outputs from the cross-channel row transfer functions will be biased in power towards the very low end of the spectrum. To understand the

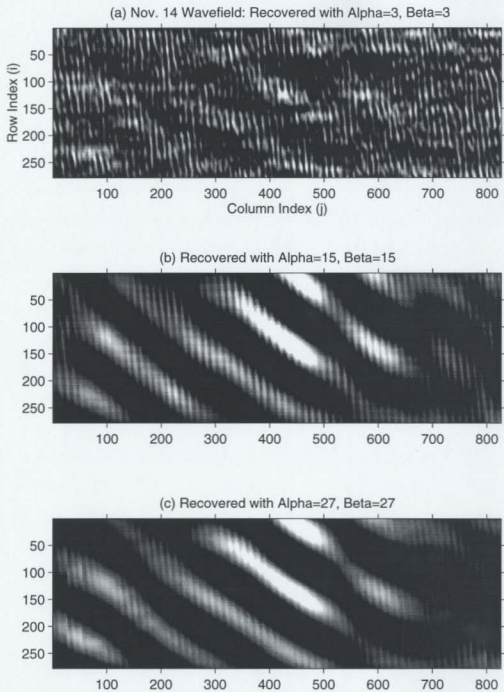


Figure 5.5: Realizations of Nov. 14 bandpass process for $\beta=\alpha$, at three distinct values of α .

impact of this, suppose that the time-domain output from h_{22} for these values of β , actually incorporates power relationships comparable to those which comprise Figure 5.4(b), say; this implies that a significant contribution from the higher-frequency 10° wavefield still exists. Then, after summations involving the h_{22} output and the cross-channel contributions from h_{21} and h_{23} , the lower-frequency component within the combined output must experience a significantly greater gain in power, relative to the higher-frequency component. This will occur because of the low-frequency bias which large β introduces to the cross-channel contribution, and explains how the row dimension of the 30° wavefield experiences enhancement in Figures 5.5(b) and 5.5(c). A similar process possibly occurs in the columns as well; in fact, reference to the column-cross coherence function for Nov. 14, shown in Figure 5.1(b), shows that the bandwidth of significant coherence does indeed narrow with increasing β . However, there is insufficient resolution for determining which frequency points of Figure 5.1(b) correspond to the 30° wavefield, and which ones relate to the 10° wavefield. Hence, it is difficult to confirm the presence of a low frequency bias in the cross-channel transfer functions for the columns. Note also, that in Figures 5.5(b) and 5.5(c), all traces of the 90° wavefield have disappeared; here too, in the absence of greater resolution for the numerical estimates of $\gamma_{cc}^2(f|0,\beta)$, it is not possible to provide a rigorous explanation.

Figure 5.6 shows one set of process realizations obtained from the Nov. 18 image, with results for $(\alpha,\beta)=(15,3)$ and $(\alpha,\beta)=(27,3)$ shown in 5.6(b) and 5.6(c) respectively; the wavefield which was recovered in Chapter Four for Nov. 18, with $(\alpha,\beta)=(3,3)$, is shown in Figure 5.6(a) as a reference. In these images also, there exists obvious differences between the three filtered estimates of the Nov. 18 bandpass process, indicating that each filter set corresponds to a different realization of Wold's decomposition. Furthermore, an interesting phenomenon is observed in Figure 5.6(b), which warrants further investigation. Upon inspection, it will be observed that this image incorporates a higher-frequency component which is oriented at 90° CCW from vertical;

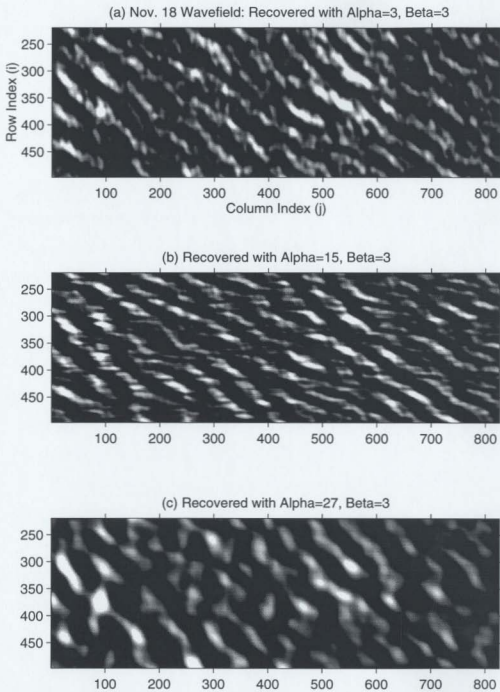


Figure 5.6: Realizations of Nov. 18 bandpass process for $\beta=3$, at three distinct values of α .

this means that the wavefield exists in the column dimension of the image only. Comparison of Figure 5.6(b) with Figure 5.6(a) will reveal that this wavefield is not present for $(\alpha, \beta) = (3, 3)$, and has been introduced by changing the filter parameters to $(\alpha, \beta) = (15, 3)$. An examination of the FFT analysis in Appendix V, will verify that the introduction of an higher frequency component has indeed occurred exclusively within the columns. In fact, this analysis shows that for the row component, changing from $(\alpha, \beta) = (3, 3)$ to $(\alpha, \beta) = (15, 3)$ has actually imparted an *attenuation* to the higher frequency points of the spectrum. Supplementary to this, Figure 5.7 presents an FFT analysis of the column components from Figures 5.6(a) and 5.6(b), along with the power transfer function which maps the column power of the former into that of the latter. These spectra are based on 1024-point FFT's, with $-1 < f \leq 1$, of which a subsection corresponding to $-0.25 \leq f \leq 0.25$ has been presented here; the spectral normalization procedures are those which were discussed in Chapter Three. When comparing the spectrum for $(\alpha, \beta) = (3, 3)$ to that associated with $(\alpha, \beta) = (15, 3)$, it is clear that digital frequencies for $0.05 \leq |f| \leq 0.25$ have increased in power as a result of changing α from a value of 3 to a value of 15. In fact, the power transfer function in Figure 5.6(c) shows that for $|f|$ in this range, the power spectra experience relative gains which are all positive; in some cases, these factors are as high as 15 dB.

By referring once more to the scalar Wiener filter of Eq. (2.40) as an analogy for the vector filter, it is possible to understand the phenomenon which has been observed in the columns of Figure 5.6(b). By substitution of Eq. (2.20) into Eq. (2.40), it is seen that variations in the magnitude of frequency response, due to α and β at fixed f , is determined by the numerator spectra, $G_{xy}(f|\alpha, \beta)$. Recall next, those attributes which characterize the behaviour of $G_{xy}(f|\alpha, \beta)$ for Case II correlation data, as discussed in Section 2.4.3.2. Specifically, for increasing α at any fixed f , the magnitude of $G_{xy}(f|\alpha, \beta)$ will in part be determined by the degree of destructive or constructive interference which results from summation of the n complex terms comprising the spectrum. Given this statement, consider also that the frequency response surfaces of Figures 5.2

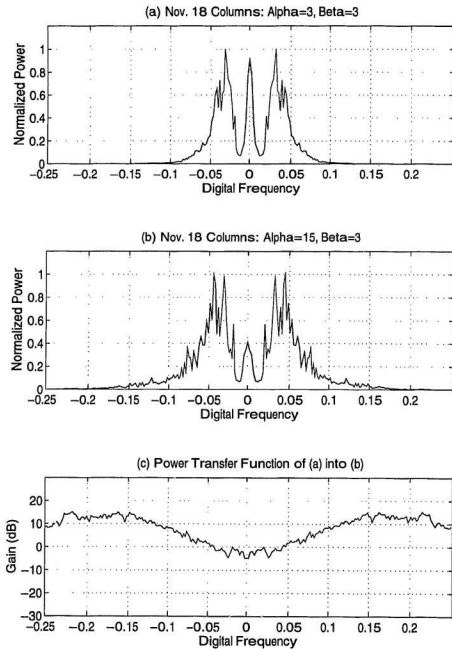


Figure 5.7: Normalized power spectra from column components of recovered wavefield realizations for Nov. 18, are shown in (a) and (b). The power transfer function which maps (a) into (b), is shown in (c).

and 5.3 do demonstrate cyclic behaviour as α advances, consistent with patterns predicted by $G_{\alpha}(f|\alpha,\beta)$. Based upon this, it is now reasonable to conclude that by advancing α from 3 to 15 when deriving the column filters, an increased degree of *constructive* interference occurs between the n complex terms of Eq. (2.20), for those frequency points which lie in the approximate range of $0.05 \leq |f| \leq 0.25$. While this explanation certainly cannot be directly verified, it is nonetheless consistent with the relative changes observed to occur between Figures 5.6(a) and 5.6(b).

Figure 5.8 displays the second set of process realizations obtained from the Nov. 18 image, for $(\alpha,\beta)=(15,15)$ and $(\alpha,\beta)=(27,27)$. As with all previous comparisons, it is clear that Figures 5.8(a), 5.8(b) and 5.8(c) each present different realizations of what is known to be the same bandpass process. Furthermore, from Figure 5.8(b), it is clear that the high frequency column component seen in Figure 5.6(b), no longer exists; yet, the only difference between the filters which produced these images, is that β was increased from a value of 3 to a value of 15 for Figure 5.8(b). When the cross-channel transfer functions are cast in the analogy of the scalar Wiener filter of Eq. (2.40), this disappearance can also be interpreted as a consequence of changes in $G_{\alpha}(f|\alpha,\beta)$. From the analytical form of $G_{\alpha}(f|\alpha,\beta)$ in Eq. (2.20), it is seen that with α fixed at say, 15, increasing β from 3 to 15 would once again alter the relationship between the n complex phasors which define the frequency response at any f . It is therefore reasonable to postulate that for f in the range of $0.05 \leq |f| \leq 0.25$, this new arrangement leads to a *comparatively* destructive addition of the n complex terms.

Other evidence of the effects which Wold's decomposition can exert upon the vector filter may be found in Figure 5.8(c), which was recovered with $(\alpha,\beta)=(27,27)$. In both the extreme right and the extreme left regions of this image, there exists a filtering artifact which presents itself as a strip running from top to bottom. The boundaries of these strips are demarcated by a discontinuity in the pattern of the recovered wavefield. To understand the reason for this phenomenon, recall that for the vast majority of rows within the image, the transfer functions h_{2j} ,

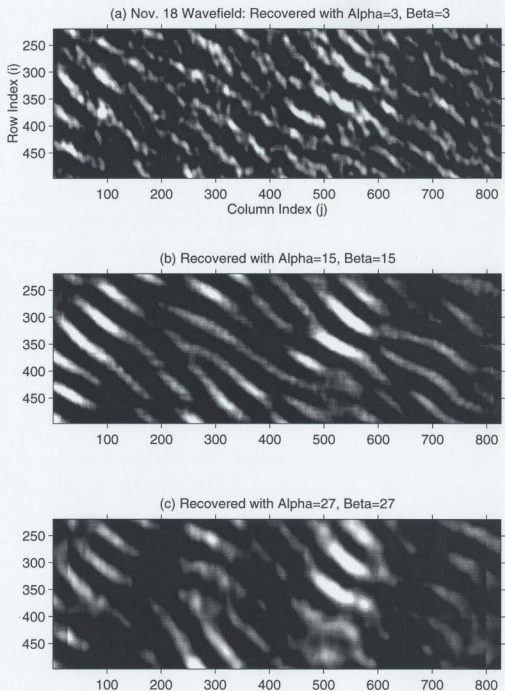


Figure 5.8: Realizations of Nov. 18 bandpass process for $\beta=\alpha$, at three distinct values of α .

h_{22} and h_{23} are used. These transfer functions map the inputs from Channels 1, 2 and 3 into the output estimate for Channel 2. However, as discussed in Section 2.6.1, the three-channel configuration of the operator implies that a Channel 2 estimate cannot be obtained for image rows $i=1, \dots, \beta$ or $i=N_R-\beta+1, \dots, N_R$. Consequently, for these row sets, it is necessary to use output estimates for Channel 1 and Channel 3 respectively. This requires the use of transfer functions h_{11} , h_{12} , and h_{13} for the Channel 1 output estimate, and transfer functions h_{31} , h_{32} , and h_{33} for the Channel 3 output estimate. Clearly, for the Channel 2 output, involving cross-channel transfer functions h_{21} and h_{23} , the cross-channel inputs come from rows which are only $\pm\beta$ steps away in the column dimension. However, for both the Channel 1 and Channel 3 output estimates, one of the cross-channel inputs must come from rows which are 2β and -2β steps away, respectively. From the coherence functions in Figure 5.1, it is clear that these differences in β will mean that the cross-channel relationships associated with $\{h_{11}, h_{12}, h_{13}\}$ and $\{h_{31}, h_{32}, h_{33}\}$ are different from those associated with $\{h_{21}, h_{22}, h_{23}\}$. This implies that with Case II correlation data, the output which the first two sets of transfer functions will produce, in response to the same input, will differ from that which is generated by the third set. Hence, the Channel 2 output estimate constitutes a realization of Wold's decomposition which is different from the realization produced by the Channels 1 and 3 output estimates. Of course, these same relationships also hold for the column transfer functions, and in fact, the artifacts occurring in Figure 5.8(c) were produced by the column filtering operation.

Figure 5.8(c) also contains another feature which warrants some mention. Although careful scrutiny may be required, within this image it is possible to assimilate a pattern which resembles four wavelike undulations, each of which has a major-axis orientation at about 140° CCW from vertical. This may well be the 140° wavefield which was suggested to be present by the correlation map in Figure 4.4(b), but for which there has been no visual evidence heretofore.

5.5 Summary

In this Chapter, results have been presented which confirm that for Case II correlation data, the role of Wold's decomposition is significant in affecting the output from the vector filtering operation. Convincing numerical evidence has indicated that the values selected for filter parameters α and β , will directly determine the particular realization of Wold's decomposition which emerges from the filtering operation. Any alteration of these parameters will propagate a detectable and often significant change in filter output. This presents a dramatic contrast to the results of Chapter Three, wherein it was demonstrated that for Case I correlation data, the filter output was unaffected by changes in α and β . The phenomenon for Case II correlation data can be rationalized through an analytical conceptualization of complex phasor interactions and exponential damping factors; these have been based on the spectral relationships which are thought to exist within the one-dimensional row and column processes of the image. Without exception, empirical evidence based on numerical analysis of the image data, has been consistent with the results predicted by these analytical forms.

This means that when Case II spectra are subjected to filtering, it will not be possible to produce a unique wavefield pattern which is common to all combinations of α and β . However, realizations of Wold's decomposition which are achieved with small α and β , are more representative of the original bandpass process than are realizations obtained with large α and β . Since the values for these parameters are chosen such that $\alpha > c$ and $\beta > c$, the implication is that the spatial extent of noise correlation, represented by c , predetermines the extent to which the recovered bandpass process can be representative of its original counterpart from the noisy image. Consequently, while it is possible to obtain a noise-suppressed version of the noise-perturbed bandpass process, numerical results indicate that this process can never be recovered in its entirety.

Furthermore, note that the investigations involving fixed β with varying α , as well as those for jointly-varying $\beta=\alpha$, do have a practical ramification. To see this, first consider that if

c is large, then it has been clearly shown that selecting $\alpha = \beta > c$ will result in recovery of only a portion of the bandpass process. However, unlike the case for α , which *must* be greater than c , it is possible to recover a filtered version for which $\theta < \beta \leq c$; a fact which is apparent from the results shown in Chapter Three. While this filter configuration would not incorporate optimal noise suppression, it does offer a compromise. This is because a greater portion of the bandpass process can be recovered if optimum noise suppression is waived, and β is chosen to be some value less than c , while α remains greater than c . With this arrangement, the three-channel filter is still superior to the one-channel version, because the cross-row coherence within the noise process does decrease with increasing β , when $\theta < \beta \leq c$. Hence, it is foreseeable that a compromise could be established between what is a desirable degree of noise decorrelation, and what is an acceptable loss of information regarding the bandpass process, for $\theta < \beta \leq c$.

CHAPTER SIX

CONCLUSIONS

6.1 Overview

The objective of this project has been to develop a filtering technique which will enable the recovery of a wide-sense stationary (WSS) desired signal process, from a two-dimensional image contaminated by broad-band WSS noise. Pursuant to this, it has been the working hypothesis that a linear filtering operator, applied sequentially in one dimension to the rows of the image, and then to the columns, would be effective in achieving this goal. The linear operator which was utilized during this investigation, was a three-channel version of the vector Wiener filter. Implementation of this operator requires that the image data satisfy three prerequisites:

- (1) The signal and noise processes must be additive, and mutually stochastically independent.
- (2) Both processes must be wide-sense stationary, at least within the region which is defined by the borders of the image.
- (3) The spatial extent of correlation, c , within the noise process, must be far less than the extent of correlation within the signal process.

Where these conditions hold, linear prediction theory states that it is possible to derive a Wiener filter, which operates on the past values of a coherent data sequence in order to predict its future values. If such a function is designed to predict a value which lies α steps ahead in the

sequence, where $\alpha > c$, then the predicted sequence will be virtually free of any variations which are *uncorrelated* beyond any interval *smaller* than α . Since the correlated extent of noise is assumed to be smaller than the prediction gap, α , then the noise-induced variations will be suppressed.

In a three-channel configuration of the vector Wiener filter, each of three transfer functions operates on its respective input taken from three image rows which are separated by some distance β . These input rows are located at image row positions $i-\beta$, i , and $i+\beta$ respectively; after the filter operates on a given row triplet, the index i is incremented by one and the operation is repeated. The result of a simultaneous operation on these three rows, will be an estimate of the desired signal process which exists in row i . Such estimates are achieved by point-wise summation of output series from the cross-channel prediction filters, h_{21} and h_{23} , and from a forward prediction filter, h_{22} . Filter transfer functions h_{21} and h_{23} operate on row $i-\beta$ and row $i+\beta$ respectively, while h_{22} operates on row i . The summed output estimate which results is then used to build a new row-filtered image, row by row, as the row index i is incremented within the noisy image. After producing estimates of the desired signal from all rows in the noisy image matrix, the resulting row-filtered facsimile is transposed to permit identical operations on the columns. This is required because after row filtering is complete, some remnant noise will continue to exist in the column dimension of the image.

Within this work, it has been postulated that a three-channel version of the filter will provide a noise suppression advantage over the single-channel version. This is based on the principle that if three inputs are taken from rows which are separated by a distance of $\beta > c$, then, as a consequence of magnitude and phase relationships between rows, the power in the output row will be biased in favour of those frequencies which are coherent across the rows. Uncorrelated frequencies, such as the noise component, are then suppressed when the three filter outputs are

summed. It has been mathematically shown that this strategy offers further noise attenuation, which is supplementary to suppression achieved from the forward prediction gap, α .

The filter which is used for the row operations is derived independently of the operator which is used for column filtering. However, this does not imply that the row process is independent of the column process; to be sure, there exists an intricate relationship between the two, as is revealed in the patterns which are exhibited by a two-dimensional autocorrelation function of the image process. Yet, by proper manipulation, the two-dimensional ACF will yield sets of one-dimensional correlation functions, which separately represent the row or column components of the two-dimensional signal-plus-noise process. This provides justification for deriving either the row or column filters from one-dimensional autocorrelation and cross-correlation functions, which are obtained by averaging such functions over all rows or all columns existing in the image. Such a strategy is consistent with the assumption that the signal-plus-noise process which exists in any given row, constitutes a single realization of a parent stochastic process which involves the additive superposition of stochastic signal and broad-band noise components. Hence, each row of the image is perceived as having been generated by the same stochastic process, which is described by the two-dimensional ACF.

With regard to each three-row set occurring in the image, there exists nine correlation functions which describe the cross-row and within-row relationships, for the row triplet which is centred on index i . Estimation of these functions at each i over the entire image, generates an ensemble of functions for *each* autocorrelation and cross-correlation relationship within the three-row set. Since each row triplet is generated by the same stochastic process, then each realization of a given autocorrelation or cross-correlation function, *represents a single observation of a function which is, itself, a random variable*. Therefore, upon taking the average of each ensemble, the expectation of each autocorrelation or cross-correlation function is obtained. The ensemble-averaged correlation functions are then considered to be representative of the statistically-expected

relationships within the *row* component of the parent signal-plus-noise stochastic process. By a judicious choice of values for the parameters α and β , these ensemble-averaged correlation functions can be used to derive a three-channel vector filter which adapts to the row component of the signal process; such a filter is then capable of attenuating the row component of the noise process during the filtering operation. This same technique is also practised in conjunction with the column filtering operation. However, it has been further postulated, that although the column filter will be intended to operate on the columns of the *row-filtered* image, it must nonetheless be derived with ensemble averages obtained from the columns of the *unfiltered* image.

The effectiveness of this filtering operation was initially examined via operations on two simulated data sets consisting of discrete, two-dimensional sinusoidal components which had been contaminated by broad-band, spatially-coherent noise. This was then followed by operations on two images of ocean wave scenes, which had been obtained via airborne synthetic aperture radar (SAR); both of these images were also corrupted by broad-band spatially-correlated noise. The major difference between the correlation characteristics of these processes, was that at correlation lags having magnitude greater than c , correlation functions associated with the simulated data sets were periodic. Furthermore, except for a phase shift, their cross-row correlation functions were unaltered by increasing the value of β . During this project, such characteristics were categorized as being representative of Case I correlation data. For the radar images, however, the correlation functions were aperiodic; this was due to the influence of exponential damping factors, which produced a non-linear attenuation of amplitude as the magnitude of correlation lags increased. Due to the presence of these damping factors, the shape of cross-row correlation functions was also altered as the separation distance, β , was varied within the row triplets. Correlation functions which exhibited these characteristics have been classified as belonging to Case II correlation data. It has been shown via analytical equations, that the differences between these classes of correlation functions, lead to spectral representations which are mathematically

more intricate for Case II than for Case I. As a consequence of this, the desired signal component of the image will respond to the filtering operation in a much more complex fashion for Case II data than for Case I. Having documented these preliminary considerations, it is now possible to address the significant findings which emerged during the course of this investigation.

6.2 Significant Findings

During the execution of this project, a range of factors were investigated in order to determine their influence upon the proposed filtering technique. In part, such activities were facilitated through the derivation of mathematical models. These were required in order to anticipate behaviour of the filtering technique for certain situations, as well as to determine which operator configurations would yield optimum results. Without exception, attributes of the filtering operation which were predicted through these analytical forms, were also confirmed by numerical operations performed on simulated data sets and the ocean wave scenes which were obtained via airborne SAR. The significant findings which emerged from this sequence of postulation and verification are as follows:

- (1) It has been demonstrated that the three-channel Wiener filter is capable of suppressing broad-band coherent noise, in images which contain desired signal processes defined by Case I or Case II correlation data. Hence, the primary objective of the project has been achieved.
- (2) For applications involving bandpass processes, which are characterized by Case II correlation data, the exponentially-damped nature of the correlation functions will cause the filter to be highly sensitive to adjustments in its parameters, α and β . Convincing evidence has been presented to show that with Case II correlation data,

each combination of values for α and β will lead to a different structure within the recovered wavefield. Consequently, the bandpass process which exists in the noisy image cannot be uniquely represented by a filtered version. However, there is evidence to suggest that wavefields which are recovered with small values of α and β , will correspond more completely to the original bandpass process than will wavefields obtained with large values of these parameters. This fact contrasts with the Case I correlation data, for which it has been demonstrated that the recovered wavefields are identical over a range of values assigned to α and β . As well, the investigations which were conducted with simulated data indicated that, for all other factors being constant, greater filtering accuracy is achieved with a larger operator length, represented as ξ . This fact has not been specifically dwelt upon during the course of this project, because it is a well-known attribute of linear prediction theory.

- (3) Correlation characteristics within the SAR images closely correspond to the analytical models which have been derived in Chapter Two. Specifically, numerical estimates of the correlation functions, verify that the two-dimensional autocorrelation function of the noise process may be represented as a sum of two-dimensional delta functions. These summed delta functions have non-zero response for $-2 \leq \tau_c, \tau_R \leq 2$, where τ_c and τ_R represent the correlation lags in the column and row dimensions of the image, respectively; this establishes the spatial extent of noise correlation at $c=2$. Furthermore, there exists evidence to indicate that the numerically-estimated, two-dimensional autocorrelation function for the signal component of each image, also closely approximates its analytical representation from Chapter Two. In particular, the shape characteristics of the one-dimensional, numerically-estimated correlation functions and cross-channel spectral coherence functions, are seen to change as a function of β , and

exhibit behaviour consistent with exponential damping. Such characteristics are congruent with those of the mathematical models which were developed for Case II correlation data. Furthermore, the numerically-estimated cross-channel spectral coherence functions have also been observed to exhibit cyclic behaviour as a function of changing β . Complementary to this, frequency-response characteristics of the numerically-derived vector filter have been shown to vary cyclically as a function of increasing α . These cyclic behaviours can be readily explained by analytical spectral representations of the correlation models developed for Case II. Hence, there is extremely good agreement between the behaviour predicted by these mathematical models, and the behaviour exhibited by their numerical equivalents which were estimated from the SAR images. In general, such patterns are seen to occur for both the row and column dimensions of the images, yet, there are visible differences when comparing the row and column results. This is consistent with the fact that the SAR processor employs a technique for constructing the rows, which differs from the method by which the columns are formed.

- (4) Analytical and numerical evidence has been presented, to confirm that the three-channel Wiener filter offers noise-suppression capabilities which are superior in comparison to results achieved via a single-channel version. The absolute necessity of choosing a value for α which is greater than c , has also been demonstrated. Complementary to this, while it is certainly possible to recover a wavefield using row and column filters for which $\theta < \beta \leq c$, analytical and numerical evidence indicates that optimum noise suppression is only achieved by selecting $\beta > c$ in conjunction with $\alpha > c$.

- (5) It has also been numerically verified that both the row filters and the column filters, must be derived from correlation data which have been estimated from the original, noisy, unfiltered image. In particular, correlation data obtained from the columns of the row-filtered image will incorporate an increased extent of noise correlation, which has been induced by the row filtering procedure. Use of column operators derived from the row-filtered data, will introduce additional noise artifacts when the columns are filtered; as a consequence of which, the recovered image will yield very little useful information. However, column operators which are based on correlation data estimated from the unfiltered image, will cancel artifacts introduced from the row-filtering operation, thereby eliminating visual traces of noise.

6.3 Practical Applications of Filtering Technique

One of the most likely applications for the vector Wiener filtering technique, will be the suppression of noise within imaged wave scenes, in order that more accurate spectral estimates of the desired signal component may be extracted. The advantage of performing a Discrete Fourier Transform on a noise-suppressed image was discussed in Chapter Two. This application would be important for the extraction of directional wave spectra over a large region, thereby yielding information which would be useful in understanding how wavefield dynamics are affected by the movement of storm systems. With this type of application however, it is known that some information loss will occur within the filtered image, due to the structure of bandpass correlation functions and the necessity of performing gapped forward prediction to suppress noise.

Conversely, the information loss associated with forward prediction may actually constitute an advantage in another potential application of the filtering technique. This application involves the extraction of wave features which are of such low power that they appear only as subtle variations in the original image. One such example is the 30° wavefield shown in Figures

5.5(b) and 5.5(c). This wavefield is barely detectable within the original image, as shown in Figure 4.9(a), yet, by an appropriate adjustment of the filtering parameters, it has become highly visible within a filtered version of the image. Therefore, the vector Wiener filtering technique might see useful applications in satellite oceanography, for the study of long-period waves which would otherwise remain obscured by the presence of higher-frequency wind-generated waves.

6.4 General Conclusions and Recommendations

Based on the numerical and analytical results obtained, it is clear that the vector filtering technique is capable of recovering stationary processes which are contaminated by broadband coherent noise. However, in the case of bandpass stationary processes, the exponentially-damped nature of the correlation functions imposes limitations upon the representativeness of the wavefield which is recovered. Those wavefield realizations which are obtained with small α and β correspond more closely, but never exactly, to the original bandpass process; conversely, realizations obtained for large α and β will incorporate only a portion of the original process. When the filter is derived, it is of paramount importance that the value for α must be greater than the value which is known for c , else no useful information will be recovered; furthermore, optimum noise suppression can only be achieved if the value for β also exceeds c . These considerations imply that the extent of noise correlation predetermines the degree of completeness for wavefields which can be recovered. Consequently, for bandpass processes, the greater the value of c , the less complete will be the wavefield representations which are achievable. Therefore, at best, only nearly-complete representations can be recovered, and then only with small values of α and β . Depending on the application, this may restrict usefulness of the technique to situations in which the spatial extent of noise correlation is small.

Given this, further research could be directed towards eliminating, at least, the influence which α will have upon the filter derivation. This might improve signal recovery

capability for noise-suppression applications. One possible solution is to use rank reduction methods [27] to extract the noise component within $R_{t,t}$ in Eq. (2.31), or within its three-channel version in Eq. (2.66). A cursory investigation undertaken near the end of this project, suggested that by setting $\alpha=0$ on the RHS of Eq. (2.30), and by retaining only the noise component of $R_{t,t}$ on the LHS, it might be possible to obtain a suitable one-channel filter. However, numerical stability problems were encountered during the derivation, which cast suspicion upon the results. Hence, although the passband response appeared favourable, no attempt was made to recover a wavefield from the noisy image. Nevertheless, rank reduction methods are known to be reliable in many applications, and should be investigated as a possible means by which to extend the capability of the vector filtering technique developed during this project.

REFERENCES

- [1] Guy, E.V., and Khan, R.H. (1994), "Three-Channel Wiener Filter for Suppression of Speckle Noise in SAR Images of Ocean Scenes". Proceedings of 1994 IEEE Canadian Conference on Electrical and Computer Engineering, Halifax, N.S., September 25-28, Vol. 2, pp. 433-437.
- [2] Goodman, J.W. (1985), Statistical Optics. (New York: John Wiley & Sons, Inc.).
- [3] Goodman, J.W. (1976), "Some Fundamental Properties of Speckle". Journal of the Optical Society of America, Vol. 66, No. 11, November, pp. 1145-1150.
- [4] Knodo, K., Ichioka, Y., and Suzuki, T. (1977), "Image Restoration by Wiener Filtering in the Presence of Signal-Dependent Noise". Applied Optics, Vol. 16, No. 9, September, pp. 2554-2558.
- [5] Lim, J.S., and Nawab, H. (1981), "Techniques for Speckle Noise Removal". Optical Engineering, Vol. 20, No. 3, May/June, pp. 472-480.
- [6] Lim, J.S. (1990), Two-Dimensional Signal and Image Processing. (Englewood Cliffs, New Jersey: Prentice Hall, Inc.).
- [7] Tur, M., Chin, K.C., and Goodman, J.W. (1982), "When is Speckle Noise Multiplicative?". Applied Optics, Vol. 21, No. 7, 1 April, pp. 1157-1159.
- [8] Saleh, B.E.A., and Rabbani, M. (1980), "Linear Filtering of Speckled Images". Optics Communications, Vol. 35, No. 3, December, pp. 327-331.
- [9] Lee, J.S. (1981), "Speckle Analysis and Smoothing of Synthetic Aperture Radar Images". Computer Graphics and Image Processing, Vol. 17, No. 1, September, pp. 24-32.
- [10] Lee, J.S. (1986), "Speckle Suppression and Analysis for Synthetic Aperture Radar". Optical Engineering, Vol. 25, No. 5, May, pp. 636-643.
- [11] Frost, V.S., Stiles, J.A., Shannigan, K.S., and Holtzman, J.C. (1982), "A Model for Radar Images and its Application to Adaptive Digital Filtering of Multiplicative Noise". IEEE Transactions on Pattern Analysis and Machine Intelligence, Vol. PAMI-4, No. 2, March, pp. 157-166.
- [12] Azimi-Sadjadi, M.R., and Bannour, S. (1991), "Two-Dimensional Adaptive Block Kalman Filtering of SAR Imagery". IEEE Transactions on Geoscience and Remote Sensing, Vol. 29, No. 5, September, pp. 742-753.
- [13] Kuan, D.T., Sawchuck, A.A., Strand, T.C., and Chavel, P. (1987), "Adaptive Restoration of Images with Speckle". IEEE Transactions on Acoustics, Speech and Signal Processing, Vol. ASSP-35, No. 3, March, pp. 373-383.
- [14] Zaman, M.R., and Moloney, C.R. (1993), "A Comparison of Adaptive Filters for Edge-Preserving Smoothing of Speckle Noise". Proceedings of 1993 International

- Conference on Acoustics, Speech and Signal Processing, Minneapolis, pp. V77-V80.
- [15] Goldfinger, A.D. (1982), "Estimation of Spectra from Speckled Image.", IEEE Transactions on Aerospace and Electronic Systems, Vol. AES-18, No. 5, September, pp. 675-681.
- [16] Ouchi, K., and Burge, R.E. (1991), "Autocorrelation Function of Non-Gaussian Speckle in Synthetic Aperture Radar Images of Dynamic Sea Surfaces", International Journal of Remote Sensing, Vol. 12, No. 2, pp. 315-327.
- [17] Papoulis, A. (1991), Probability, Random Variables, and Stochastic Processes. (New York: McGraw Hill).
- [18] Cesson, T.M., Trusell, H.J., and Hunt, B.R. (1978), "Comparison of Different Image Restoration Methods". Applied Optics, Vol. 17, No. 21, 1 November, pp. 3384-3390.
- [19] Ekstrom, M.P. (1982), "Realizable Wiener Filtering in Two Dimensions". IEEE Transactions on Acoustics, Speech and Signal Processing, Vol. ASSP-30, No. 1, February, pp. 31-40.
- [20] Dudgeon, D.E., and Menseau, R.M. (1983), Multi-Dimensional Digital Signal Processing. (Englewood Cliffs, New Jersey: Prentice Hall, Inc.).
- [21] Chan, P. and Lim, J.S. (1985), "One-Dimensional Processing for Adaptive Image Restoration". IEEE Transactions on Acoustics, Speech and Signal Processing, Vol. ASSP-33, No. 1, February, pp. 117-126.
- [22] Peebles, P.Z., Jr. (1987), Probability, Random Variables, and Random Signal Principles. (New York: McGraw Hill).
- [23] Marple, S.L., Jr. (1987), Digital Spectral Analysis, With Applications. (Englewood Cliffs, New Jersey: Prentice-Hall, Inc.).
- [24] Bendat, S.J., and Persol, A.G. (1986), Random Data: Analysis and Measurement Procedures. (New York: John Wiley and Sons).
- [25] Priestly, M. (1981), Spectral Analysis and Time Series, (Vols. 1 and 2). (London: Academic Press).
- [26] Kay, S.M. (1993), Fundamentals of Statistical Signal Processing: Estimation Theory. (Englewood Cliffs, New Jersey: Prentice-Hall, Inc.).
- [27] Haykin, S.H. (1991), Adaptive Filter Theory. (Englewood Cliffs, New Jersey: Prentice-Hall, Inc.).
- [28] Papoulis, A. (1985), "Predictable Processes and Wold's Decomposition: A Review". IEEE Transactions on Acoustics, Speech and Signal Processing, Vol. ASSP-33, No. 4, August, pp. 933-938.
- [29] Robinson, E.A. (1983), Multi-Channel Time Series Analysis, with Digital Computer

Programs, Second Edition. (Houston: Goose Pond Press).

- [30] Bozic, S.M. (1979), Digital and Kalman Filtering. (London: Edward Arnold).
- [31] Little, J.N., Shure, L. (1993), Signal Processing TOOLBOX, for Use with MATLAB. (Natick, Mass.: The MathWorks, Inc.).
- [32] MATLAB (1992), MATLAB Reference Guide. (Natick, Mass.: The Mathworks, Inc.).
- [33] Haykin, S. (1994), Communication Systems. (Toronto: John Wiley and Sons, Inc.).
- [34] Munson, D.C., Jr., and Visentin, R.L. (1989), "A Signal Processing View of Strip-Mapping Synthetic Aperture Radar". IEEE Transactions on Acoustics, Speech, and Signal Processing, Vol. 37, No. 12, December, pp. 2131-3147.
- [35] Curlander, J.C., and McDonough, R.N. (1991), Synthetic Aperture Radar: Systems and Signal Processing. (New York: Wiley).
- [36] Fitch, J.P., with C.S. Burrows: Consulting Editor, (1988), Synthetic Aperture Radar. (New York: Springer-Verlag).
- [37] Krogstad, H.E. (1992), "A Simple Derivation of Hasselmann's Non-linear Ocean-Synthetic Aperture Radar Transform". Journal of Geophysical Research, Vol. 97, No. C2, pp. 2421-2425.

APPENDIX I

DISCRETE FOURIER TRANSFORM REPRESENTATION OF THE SIGNAL CROSS-CORRELATION FUNCTION

I.1 Introductory Concepts

This Appendix will derive the DFT representation for the signal component of the CCF previously defined by Eq. (2.13). To begin, consider a CCF of finite length $2N_R-1$, where N_R is the number of pixel elements in any given row of the image. The analytical form of this CCF, between any two rows separated by some fixed distance of β , may be represented as:

$$r_{xx}(\tau_R | \beta) = \sum_{k=1}^n a_k e^{-d_{kC}|\beta| - d_{kR}|\tau_R|} \cos(\omega_{kC}\beta + \omega_{kR}\tau_R) \quad (1.1)$$

$$-(N_C-1) \leq \beta \leq (N_C-1), \quad -(N_R-1) \leq \tau_R \leq (N_R-1)$$

where the index k denotes the k 'th element of some set of size n . The digital phasor increment pairs, ω_{kC} and ω_{kR} , are defined to be:

$$\omega_{kC} = \frac{2\pi\lambda_{kC}}{L_C}, \quad \omega_{kR} = \frac{2\pi\lambda_{kR}}{L_R}$$

where $(L_C, L_R) \in \mathbb{N}$, $L_C \ll N_C$, $L_R \ll N_R$

$$\text{and } (\lambda_{kC}, \lambda_{kR}) \in \{(\lambda_{1C}, \lambda_{1R}), \dots, (\lambda_{nC}, \lambda_{nR})\} \subseteq \{(\lambda_{kC}, \lambda_{kR}) \in \mathbb{I}^2 \mid 0 \leq \lambda_{kC} < L_C, 0 \leq \lambda_{kR} < L_R\} \quad (1.2)$$

It will be assumed that $L_C \ll N_C$ and $L_R \ll N_R$; since N_C and N_R are the dimensions of the image, this implies that the two-dimensional ACF from which Eq. (1.1) is derived, will incorporate many cycles of its lowest-frequency component. Furthermore, the subset indicated in Eq. (1.2) is defined to be a not-necessarily-contiguous subset of \mathbb{I}^2 .

For the k 'th sinusoid of the CCF, the terms d_{kC} and d_{kR} represent respectively, the damping factors along the column dimension and the row dimension; the term a_k represents the amplitude of the k 'th sinusoid. It will be assumed that each amplitude factor and each damping factor pair, represent the k 'th elements of their respective not-necessarily-contiguous subsets of size n , defined as:

$$\begin{aligned} a_k &\in \{ a_1, \dots, a_n \} \subset \{ a \in \mathbb{R} \mid 0 < a < \infty \} \\ (d_{kC}, d_{kR}) &\in \{ (d_{1C}, d_{1R}), \dots, (d_{nC}, d_{nR}) \} \subset \{ (d_C, d_R) \in \mathbb{R}^2 \mid 0 \leq d_C < \infty, 0 \leq d_R < \infty \} \end{aligned} \quad (1.3)$$

Therefore, Eqs. (1.1), (1.2), and (1.3) describe the general approximation of the one-dimensional CCF from a two-dimensional bandpass stochastic process contained in a digital image. For the special case in which the damping factors are identically zero and the process is narrow-band, the CCF in Eq. (1.1) reduces to a sum of n periodic sinusoids, where the k 'th component is of amplitude a_k .

Consider then, a contiguous subset of size N_R , containing coefficients taken from the right-hand side of the CCF for which the autocorrelation lag, τ_R , is non-negative. This subset may be represented as:

$$r_{gxy; \tau \geq 0} = \{ r_{gxy}(\tau_R | \beta) \mid \tau_R \geq 0 \} = \{ r_{gxy}(0 | \beta), r_{gxy}(1 | \beta), \dots, r_{gxy}(N_R - 1 | \beta) \} \quad (1.4)$$

where the elements of $r_{gxy; \tau \geq 0}$ are ordered based upon increasing values of τ_R . From analysis of $r_{gxy; \tau \geq 0}$, it is desired to obtain information regarding the spectral content of the row component of its generating stochastic process, $g(i, j)$. This analysis will be performed upon some contiguous, ordered subset within $r_{gxy; \tau \geq 0}$ of chosen size $\xi \ll N_R$, defined to be:

$$r_{gxy; \tau(\alpha)} = \{ r_{gxy}(\tau_R | \beta) \mid \alpha \leq \tau_R \leq \xi + \alpha - 1 \} = \{ r_{gxy}(\alpha | \beta), r_{gxy}(\alpha + 1 | \beta), \dots, r_{gxy}(\alpha + \xi - 1 | \beta) \} \quad (1.5)$$

where α is a non-negative integer, $0 \leq \alpha \leq N_R - \xi$. It will be assumed that ξ is chosen to be an

appropriate value such that $(\xi/L_R) \in N$; that is, L_R from Eq. (1.2) divides ξ with zero remainder. The fact that $r_{xy,(n)}$ is a discrete sequence of finite length, prompts use of the Discrete Fourier Transform (DFT) as the technique by which its spectral content will be determined. From inspection of Eq. (1.1), and by the definition of the DFT, it is easy to show that the cross-spectral density function, $G_{xy}(f|\alpha, \beta)$, for any arbitrary subset $r_{xy,(n)}$ of $r_{xy,(n)}$ may be represented as:

$$G_{xy}(f|\alpha, \beta) = \sum_{\kappa=0}^{\xi-1} r_{xy}(\kappa+\alpha|\beta) e^{jfk} \quad (1.6)$$

$$\text{for } f \in \left\{ \frac{2\pi v}{\xi} \mid v = 0, \dots, \xi-1 \right\}$$

$$\text{and, } 0 \leq \alpha \leq N_R - \xi$$

Now, by use of the well-known identity:

$$\cos(\theta) = \frac{e^{-j\theta} + e^{j\theta}}{2} \quad (1.7)$$

the negative complex exponential component of each sinusoid within the CCF, may be obtained from the analytical form of $r_{xy}(\kappa+\alpha|\beta)$. Substitution into Eq. (1.6) then yields:

$$G_{xy}(f|\alpha, \beta) = \sum_{k=1}^n \left\{ \sum_{\kappa=1}^{\xi-1} \frac{a_k}{2} e^{-d_{1c}|\beta|} e^{-d_{1s}\kappa} e^{-d_{2s}\kappa} e^{-j\omega_{1c}\beta} e^{-j\omega_{1s}\kappa} e^{-j\omega_{2s}\kappa} e^{jfk} \right\} \quad (1.8)$$

Rearranging terms, based on the index κ , gives the final form as:

$$G_{xy}(f|\alpha, \beta) = \sum_{k=1}^n \frac{a_k}{2} e^{-(d_{1c}|\beta| + d_{1s}\kappa)} e^{-j(\omega_{1c}\beta + \omega_{1s}\kappa)} \left\{ \sum_{\kappa=0}^{\xi-1} e^{(-d_{2s} - j\omega_{2s} + jf)\kappa} \right\} \quad (1.9)$$

From this it now follows that the k 'th component of $G_{xy}(f|\alpha, \beta)$ is simply:

$$G_{xy}(f|\alpha, \beta)_k = \frac{a_k}{2} e^{-(d_{1c}|\beta| + d_{1s}\kappa)} e^{-j(\omega_{1c}\beta + \omega_{1s}\kappa)} \left\{ \sum_{\kappa=0}^{\xi-1} e^{(-d_{2s} - j\omega_{2s} + jf)\kappa} \right\} \quad (1.10)$$

$$= \frac{a_k}{2} e^{-(d_{1c}|\beta| + d_{1s}\kappa)} e^{-j(\omega_{1c}\beta + \omega_{1s}\kappa)} \mathfrak{S}(f)_k$$

where $\mathfrak{G}(f)_k$ denotes the actual contribution to $G_{v_i}(f|\alpha,\beta)_k$ that is due to the DFT. Clearly, $\mathfrak{G}(f)_k$ is independent of α and β ; hence, for fixed α and β , the value associated with the k 'th spectral component of $G_{v_i}(f|\alpha,\beta)$ for any f , is determined by $\mathfrak{G}(f)_k$. The influence which $\mathfrak{G}(f)_k$ has on the outcome of $G_{v_i}(f|\alpha,\beta)_k$ can now be examined for three possible cases.

1.2 Case I: Damping Coefficients are Identically Zero

The first case to be investigated deals with the trivial situation in which the damping coefficients are identically zero, that is, $d_{ik} = d_{kR} = 0$, $k=1,2,\dots,N$. With reference to Eq. (1.10), it is easy to see that for this case, $\mathfrak{G}(f)_k$ reduces to:

$$\mathfrak{G}(f)_k = \sum_{\kappa=0}^{\xi-1} e^{-j(\omega_{kR}-f)\kappa} \quad (1.11)$$

Now, when $f = \omega_{kR}$, then $e^{-j(\omega_{kR}-f)} = 1$, from which it follows that:

$$\mathfrak{G}(f)_k = \sum_{\kappa=0}^{\xi-1} 1 = \xi, \quad \text{for } f = \omega_{kR} \quad (1.12)$$

However, when $f \neq \omega_{kR}$, then Eq. (1.11) represents the ξ 'th partial sum of a geometric series, which may be expressed as:

$$\mathfrak{G}(f)_k = \frac{1 - e^{-j(\omega_{kR}-f)\xi}}{1 - e^{-j(\omega_{kR}-f)}}, \quad \text{for } f \neq \omega_{kR} \quad (1.13)$$

Upon close examination of the complex exponential portion of the numerator in Eq. (1.13), it is seen that this may be written as:

$$e^{-j(\omega_{kR}-f)\xi} = \exp \left\{ -j \left(\frac{2\pi \lambda_{kR}}{L_R} - \frac{2\pi \nu}{\xi} \right) \xi \right\} \quad (1.14)$$

Given that L_{ν} divides ξ , then $(\xi/L_{\nu}) = r \in N$; also, $\nu \in I$ and $\lambda_{kR} \in I$. This permits the rewriting of Eq.

(1.14) as:

$$e^{-j(\omega_{kR}-f)\xi} = \exp \{ -j \{ 2\pi (\lambda_{kR}r - \nu) \} \} \quad (1.15)$$

From the preceding discussion, it is clear that $(\lambda_{kR}r - \nu) = \sigma \in I$, hence, for $f \neq \omega_{kR}$, $\mathfrak{G}(f)_k$ becomes:

$$\mathfrak{G}(f)_k = \frac{1 - e^{-j2\pi\sigma}}{1 - e^{-j(\omega_{kR}-f)\xi}} \quad \text{for } f \neq \omega_{kR} \quad (1.16)$$

However, $2\pi\sigma$ is a root of unity of the complex exponential. Hence, $e^{j2\pi\sigma} = 1$, and it follows that $\mathfrak{G}(f)_k = 0$ in Eq. (1.16). Consequently, the Fourier component of Eq. (1.10) may be summarized as:

$$\mathfrak{G}(f)_k = \begin{cases} \xi, & f = \omega_{kR} \\ 0, & f \neq \omega_{kR} \end{cases} \quad (1.17)$$

From these discussions it is clear that any k 'th component, $G_{xy}(f|\alpha, \beta)_k$, will be non-zero only when $f = \omega_{kR}$. It can now finally be concluded that the DFT of $r_{xy}(\tau_R|\beta)$, for the case of identically zero damping coefficients, is represented as:

$$G_{xy}(f|\alpha, \beta) = \sum_{k=1}^{\xi} \xi \frac{a_k}{2} e^{-j(\omega_{kR} \beta + \omega_{kR} \alpha)} \delta(f - \omega_{kR}) \quad (1.18)$$

Therefore, it has been shown that the spectrum of the process defined by the CCF of Eq. (1.1), can be represented as a sequence of line spectra for the case in which the damping coefficients are identically zero. The only prerequisite is that the length, ξ , of the DFT must be chosen such that (ξ/L_{ν}) is a member of the positive set of integers.

1.3 Case II: Damping Coefficients are Non-Zero

In this Section, the case for which all damping coefficients are non-zero will be examined. By inspection of Eq. (1.10), it is seen that in this case, $\mathfrak{G}(f)_k$ is expressed as:

$$\mathfrak{G}(f)_k = \sum_{\xi=0}^{\xi-1} e^{(-d_{ik} - j(\omega_{ik} - f))\xi} \quad (1.19)$$

Clearly, when $f = \omega_{ik}$, this equation reduces to the ξ 'th partial sum of a geometric series involving $e^{-d_{ik}}$, expressed as:

$$\mathfrak{G}(f)_k = \frac{1 - e^{-d_{ik}\xi}}{1 - e^{-d_{ik}}} \quad \text{for } f = \omega_{ik} \quad (1.20)$$

a result which is $\in \mathcal{R}$. However, for the general case in which $f \neq \omega_{ik}$, the ξ 'th partial sum of the geometric series in Eq. (1.19) is seen to be:

$$\begin{aligned} \mathfrak{G}(f)_k &= \frac{1 - e^{-d_{ik}\xi} e^{-j(\omega_{ik} - f)\xi}}{1 - e^{-d_{ik}} e^{-j(\omega_{ik} - f)}} \\ &= \frac{1 - e^{-d_{ik}\xi}}{1 - e^{-d_{ik}} e^{-j(\omega_{ik} - f)}} \quad \text{for } f \neq \omega_{ik} \end{aligned} \quad (1.21)$$

where the second step in Eq. (1.21) is due to the fact that $(\xi/\ell_{ij}) \in \mathcal{I}$, as was shown for Case I; this general result is $\in \mathcal{C}$. By algebraic manipulation of terms, it is possible to rewrite Eq. (1.21) as:

$$\mathfrak{G}(f)_k = \frac{e^{-\left\{\frac{d_{ik}\xi}{2}\right\}}}{e^{-\left\{\frac{d_{ik}}{2}\right\}} e^{-j\left\{\frac{(\omega_{ik} - f)}{2}\right\}}} \times \frac{e^{\left\{\frac{d_{ik}\xi}{2}\right\}} - e^{-\left\{\frac{d_{ik}\xi}{2}\right\}}}{e^{\left\{\frac{d_{ik}}{2}\right\}} e^{j\left\{\frac{(\omega_{ik} - f)}{2}\right\}} - e^{-\left\{\frac{d_{ik}}{2}\right\}} e^{-j\left\{\frac{(\omega_{ik} - f)}{2}\right\}}} \quad (1.22)$$

which leads to a final form, summarized as:

$$\mathfrak{C}(f)_k = e^{d_{kR}\left\{\frac{1-\xi}{2}\right\}} e^{j\left\{\frac{\omega_{kR}-f}{2}\right\}} \frac{\sinh\{d_{kR}\xi/2\}}{\sinh\{(d_{kR} + j\omega_{kR} - jf)/2\}} \quad (1.23)$$

Now, the exponential terms can never be zero, given finite values for their arguments, and the *sinh* function in the numerator of Eq. (1.23) can be zero only when $d_{kR} = 0$ or $\xi = 0$, both of which are impossibilities under the assumptions for Case II. Consequently, it now follows that if all damping coefficients are non-zero, then $\mathfrak{C}(f)_k$ is also non-zero for all f . By combining Eq. (1.10) and Eq. (1.23), it is seen that the general form of $G_{xy}(f|\alpha, \beta)$ under Case II may now be written as:

$$G_{xy}(f|\alpha, \beta) = \sum_{k=1}^n \frac{a_k}{2} e^{-\left(d_{kC}|\beta\right) \cdot d_{kR}\left[\frac{2n+\xi-1}{2}\right]} e^{-j\left[\omega_{kR}\beta \cdot \left[\frac{2\omega_{kR}n+f-\omega_{kR}}{2}\right]\right]} \frac{\sinh\{d_{kR}\xi/2\}}{\sinh\{(d_{kR} + j\omega_{kR} - jf)/2\}} \quad (1.24)$$

which is non-zero for all f . Hence, it has been shown that if all damping coefficients are non-zero, then the spectrum of the stochastic process described by $r_{xy}(\tau_R|\beta)$ *cannot be represented as a line spectrum*.

1.4 Case II!: Damping Coefficients are Combination of Zero and Non-Zero Terms

Following from the above discussions, it is easy to conclude that if some damping coefficients are zero while others are not, then $G_{xy}(f|\alpha, \beta)$ may be represented as a summed combination of the terms from the RHS of Eq. (1.18) and Eq. (1.24). This will not be explicitly shown, however, it does follow that if only one damping coefficient is non-zero within this summation, then $G_{xy}(f|\alpha, \beta)$ can never be a line spectrum and will be non-zero for all f .

APPENDIX II

PROCESSING ALGORITHMS FOR IMPLEMENTATION OF FILTERING TECHNIQUE

II.1 Overview

This Appendix describes a series of algorithms which can be used to implement the vector filtering operation developed during this project. These algorithms are written in the MATLAB protocol [31], [32], and incorporate the three-channel relationships which were formally defined in Chapter Two. There are two main algorithms, the first of which performs numerical estimation of one-dimensional correlation functions, while the second derives a three-channel transfer function based on the correlation estimates, and then implements the filtering operation. Both algorithms will operate only in the row dimension of the image; therefore, each has an associated calling algorithm which transposes the image after the row operations, so that both dimensions of the image may ultimately be processed. In adherence to the procedure which was established in Chapter Three, estimation of the correlation functions is performed for both the row and column dimensions of the noisy image; after this has been completed, the filtering algorithm is executed. Prior to the implementation of these algorithms, the image must be subjected to a two-dimensional detrending operation, which is needed in order to ensure that the image contains an approximately zero-mean process. The structure of these operations will now be described for an application involving the detrended, noisy image designated as *NOV18.mat*; the actual image matrix which exists within this file is assigned the variable name *IM*.

II.2 Description of Calling Programs

The numerical estimation of correlation functions is coordinated by the calling program *ACF_CALL.m*, which in turn calls the correlation estimation program *ACF.m*. By a similar procedure, the image filtering operation is coordinated by program *MCW_CALL.m*, which calls the filtering algorithm *MCW_F.m*.

The calling program *ACF_CALL.m* is structured as follows:

```
load NOV18.mat           % load data file.
beta = 3;                % define value for  $\beta$ .
ACF                      % call correlation estimation for rows.
ROW_C = R;              % assign row correlation average to storage variable.
r_zlag = zlag;          % store vector address which denotes  $\tau_r = 0$ .
IM = IM';               % transpose image to permit column estimation.
ACF                      % call correlation estimation for columns.
COL_C = R;              % assign column correlation average to storage variable.
c_zlag = zlag;          % store vector address which denotes  $\tau_c = 0$ .
clear IM R zlag
save NOV18_1D_ACF       % save correlation functions to disk.
```

The calling program *MCW_CALL.m* has been organized in the following format:

```
alpha = 3;               % define value for  $\alpha$ .
beta = 3;                % define value for  $\beta$ .
xi = 3;                  % define value for  $\xi$ .
load NOV18.mat
load NOV18_1D_ACF.mat
R = ROW_C;               % assign row correlation functions.
```

```

zlag = r_zlag;           % assign vector index specifying position of zero lag.
MCW_F           % implement derivation of row operator, and filtering.
T_ROW = F;       % assign row transfer functions to storage variable.
[x1,y1] = size(IM); % prepare for scaling of row-filtered image.
top = ROW_C(5,zlag);
bot = sum(sum(IM.^2))/(x1 * y1);
scale = sqrt(top/bot);
IM = IM*scale;      % scale row-filtered image back to power levels at input.
R = COL_C;         % REPEAT ABOVE PROCEDURE FOR COLUMNS.
zlag = c_zlag;
MCW_F
T_COL = F;
[x1,y1] = size(IM);
top = COL_C(5,zlag);
bot = sum(sum(IM.^2))/(x1 * y1);
scale = sqrt(top/bot);
IM = IM*scale;
save NOV18_FILT IM T_ROW T_COL

```

Note that after each filtering operation, the output image is scaled to ensure that it incorporates the same average level of power as that which existed within the unfiltered input image. This scale factor is derived with reference to the power value associated with the zero autocorrelation lag of the original image. A scaling operation of this nature has no mathematical impact upon the filtering operation; hence, it does not improve the accuracy of the output in any way. However, when either the row-filtered or final output image is compared to the noisy

version, on a video display terminal, the equivalence of power within both images permits use of a common grey-scale mapping algorithm. Without this, several attempts might be required in order to display the filtered image with an acceptable range of grey levels.

11.3 Estimation of Correlation Functions

The correlation relationships which exist within any row triplet will generate nine correlation functions. These functions and their ensemble averages, are estimated from the rows or columns of the image by the algorithm *ACF.m*. The program utilizes biased correlation estimates which are formally discussed in [24] & [31]. One advantage of biased estimates is that they eliminate the need for tapering windows, which are otherwise needed with unbiased estimates in order to reduce error at large lag numbers, where fewer samples are involved. The correlation estimation program is structured as follows:

```
[x1,y1] = size(IM);
R = zeros(9,(2*y1)-1);
Rt = R;
div = 0;
for im = (beta + 1):(x1-beta),
    div = div + 1;
    Rt(1,:) = xcorr(IM(im-beta,:),IM(im-beta:),'biased');
    Rt(2,:) = xcorr(IM(im,:),IM(im-beta:),'biased');
    Rt(3,:) = xcorr(IM(im+beta,:),IM(im-beta:),'biased');
    Rt(4,:) = xcorr(IM(im-beta,:),IM(im:),'biased');
    Rt(5,:) = xcorr(IM(im,:),IM(im:),'biased');
    Rt(6,:) = xcorr(IM(im+beta,:),IM(im:),'biased');
    Rt(7,:) = xcorr(IM(im-beta,:),IM(im+beta:),'biased');
```

```

Rt(8,:) = xcorr(IM(im,:),IM(im + beta,:), 'biased');
Rt(9,:) = xcorr(IM(im + beta,:),IM(im + beta,:), 'biased');
R = R + Rt;

end

R = R./div;

zlag = y1;

clear div Rt x1 y1

```

II.4 Derivation of Transfer Functions and Implementation of Filtering Operation

The program *MCW_F.m*, for derivation of transfer functions and implementation of the filtering operation, is structured as follows:

```

[x1,y1] = size(IM);
% CONSTRUCT  $R_{3\ell \times 3\ell}$  (MATRIX VARIABLE NAME PHI), AS DEFINED BY EQ. (2.66)
% PHI IS INITIALIZED AS A BLOCK VECTOR, THEN BUILT UPON
PHI = zeros(3,3*xi);
for r = 1:xi,
    A = zeros(3,3);
    for c = 1:xi,
        k = 0;
%        BUILD INDIVIDUAL ELEMENTS ( $3 \times 3$  MATRICES) OF  $R_{3\ell \times 3\ell}$ 
        for i = 1:3,
            for j = 1:3,
                k = k + 1;
                TR(i,j) = R(k,zlag + (c-r));
            end
        end
    end
end

```

```

        end

    end

% APPEND EACH ELEMENT COLUMN-WISE

    if c == 1
        A = TR;
    else
        A = [A,TR];
    end

end

end

% APPEND EACH BLOCK ROW VECTOR ROW-WISE TO PHI

    if r == 1
        PHI = A;
    else
        PHI = [PHI;A];
    end

end

end

DESR = zeros(3,3);

% CONSTRUCT  $r_{3 \times 3}$  (MATRIX VARIABLE NAME DESR) AS DEFINED BY EQ.
% (2.66)

for c = 1:xi,
    k = 0;

% BUILD INDIVIDUAL ELEMENTS ( $3 \times 3$  MATRICES) OF  $r_{3 \times 3}$  (DESR)

    for i = 1:3,
        for j = 1:3,
            k = k + 1;

```

```

        TR(i,j) = R(k,(zlag-1) + c + alpha);
    end
end
% APPEND ELEMENTS COLUMN-WISE
if c == 1
    DESR = TR;
else
    DESR = [DESR,TR];
end
end
% DERIVE BLOCK ROW VECTOR,  $h_{3 \times 3P}$  OF MATRIX TRANSFER FUNCTION
% COEFFICIENTS AS DEFINED BY EQ. (2.66). STORE RESULT IN (3 × 3 $\beta$ ) MATRIX
% MCTRANS.
MCTRANS = DESR*inv(PHI);
% REMOVE INDIVIDUAL ELEMENTS FROM MCTRANS AND CONSTRUCT TRANSFER
% FUNCTIONS  $h_{11}, h_{12}, h_{13}, h_{21}, h_{22}, h_{23}, h_{31}, h_{32}, h_{33}$  FOR SCALAR OPERATIONS
F = zeros(9,xi);
for i = 1:xi,
    for j = 1:3,
        F(3*(j-1) + 1:3*j,i) = (MCTRANS(j,(3*(i-1) + 1:(3*i))))';
    end
end
%
F = fliplr(F);
% PROCEED TO FILTER IMAGE

```

```

for j = 1:2,
    [x1,y1] = size(IM);
    for im = (beta + 1):(x1-beta),
        c1 = hankel(IM(im-beta,1:(y1-xi + 1)),IM(im-beta,(y1-xi + 1):y1));
        c2 = hankel(IM(im,1:(y1-xi + 1)),IM(im,(y1-xi + 1):y1));
        c3 = hankel(IM(im + beta,1:(y1-xi + 1)),IM(im + beta,(y1-xi + 1):y1));
        fc1 = c1 * F(4,:)' ; %  $h_{21}$  operates.
        fc2 = c2 * F(5,:)' ; %  $h_{22}$  operates.
        fc3 = c3 * F(6,:)' ; %  $h_{23}$  operates.
        IM2(im,1:(y1-xi + 1)) = (fc1 + fc2 + fc3)';
        %
        if (im >= (beta + 1)) & (im <= (2 * beta)),
            fc1 = c1 * F(1,:)' ; %  $h_{11}$  operates.
            fc2 = c2 * F(2,:)' ; %  $h_{12}$  operates.
            fc3 = c3 * F(3,:)' ; %  $h_{13}$  operates.
            IM2(im-beta,1:(y1-xi + 1)) = (fc1 + fc2 + fc3)';
        end
        %
        if (im >= (x1-(2 * beta) + 1)) & (im <= (x1-beta)),
            fc1 = c1 * F(7,:)' ; %  $h_{31}$  operates.
            fc2 = c2 * F(8,:)' ; %  $h_{32}$  operates.
            fc3 = c3 * F(9,:)' ; %  $h_{33}$  operates.
            IM2(im + beta,1:(y1-xi + 1)) = (fc1 + fc2 + fc3)';
        end
    end
end
end

```

```

        IM2 = flipplr(IM2);
        IM = flipud(IM2);
        clear IM2
end
%
clear x1 y1 PHI A r c k j i TR R
clear DESR MCTTRANS c1 c2 c3 fc1 fc2 fc3
IM = IM';

```

II.5 An Algorithm for Detrending the Noisy Image

At present, neither the core MATLAB [32] nor the MATLAB Signal Processing Toolbox [31], provide any algorithm for implementation of the two-dimensional polynomial detrending operation discussed in Chapter Four. To fill this void, a routine has been borrowed from the *m*-file library of the Remote Sensing Group at C-CORE, Memorial University of Newfoundland. This detrending procedure is structured as follows:

```

% This routine fits 2D polynomials and detrends a 2-D data set
% function [z,p] = trend(z, x, y, lord)
% For example, a 3rd order has the form:
%  $z(y,x) = p_0 + p_1*y + p_2*x + p_3*y^2 + p_4*y*x + p_5*x^2$ 
%  $+ p_6*y^3 + p_7*y^2*x + p_8*y*x^2 + p_9*x^3$ 
% p - polynomial coefficients in ascending order
% z - two-dimensional data matrix m x n
% x - x-axis values, length m
% y - y-axis values, length n

```

```

% iord - polynomial order
% Detrended data is returned in original array z
%
function [z,p] = trend(z, x, y, iord)
[n,m] = size(z);
% number of coefficients in p
ncoef = (iord + 1) * (iord + 2) / 2;
% error checking, check sizes of x and y
x = x(:);
y = y(:);
if max(size(x)) ~= m,
    error('Length of vector x must equal number of columns in z')
end
if max(size(y)) ~= n,
    error('Length of vector y must equal number of rows in z')
end
% compute components of A'A and A'Z, corresponding to each column
ata = zeros(ncoef,ncoef);
atz = zeros(ncoef,1);
for zcol = 1:m
    ajcol = 1;
    for k = 0:iord
        for subk = 1:k+1
            aj(:,ajcol) = y .^(k+1-subk) * x(zcol)^(subk-1);
            ajcol = ajcol + 1;
        end
    end
end

```

```

        end

    end

    ata = ata + aj.' * aj;

    atz = atz + aj.' * z(:,zcol);

end

%   compute polynomial coefficients

p = inv(ata) * atz;

%   detrend data, column by column

for zcol = 1:m

    ajcol = 1;

    for k = 0:iord

        for subk = 1:k+1

            aj(:,ajcol) = y .^(k+1-subk) * x(zcol)^(subk-1);

            ajcol = ajcol + 1;

        end

    end

    z(:,zcol) = z(:,zcol) - aj * p;

end

```

APPENDIX III

FREQUENCY RESPONSE MAGNITUDE CHARACTERISTICS OF VECTOR FILTERS

III.1 Overview

This Appendix presents the frequency response magnitude characteristics, of the three-channel filters which were derived for row and column operations performed in Chapters Two and Three. Figures III.1 and III.2 present frequency response magnitudes which were obtained with $\xi=60$ and $\xi=150$, for the recovered wavefields which have been displayed in Figures 3.17 and 3.18 respectively. Figures III.3 and III.4 present the frequency response magnitudes derived from the Nov. 14 and Nov. 18 noisy SAR images respectively; their corresponding recovered images are displayed in Figures 4.9 and 4.13. For filtering operations involving the SAR images, an operator length of $\xi=200$ was used.

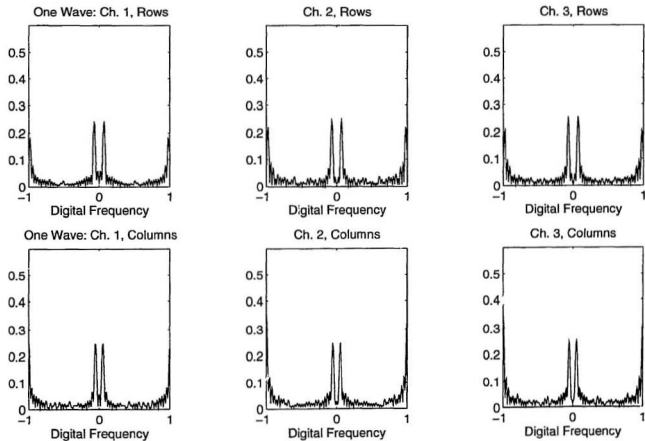


Figure III.1: Magnitude of frequency response, for filters used in recovery of one-component simulated wavefield presented in Figure 3.17.

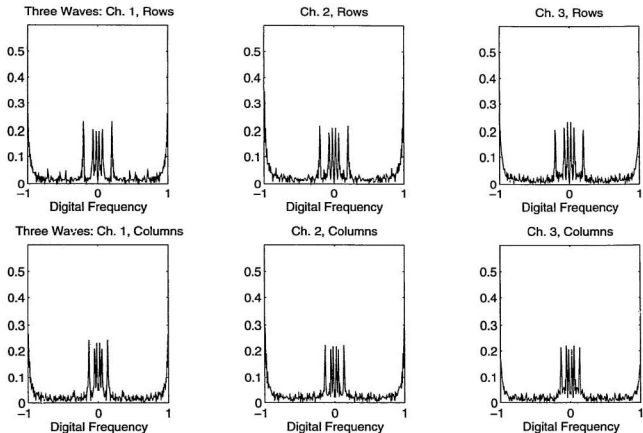
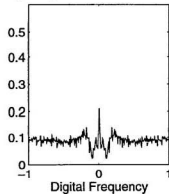
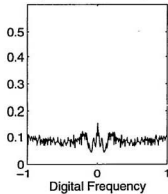


Figure III.2: Magnitude of frequency response, for filters used in recovery of three-component simulated wavefield presented in Figure 3.18.

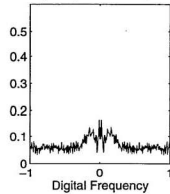
Freq. Response Nov. 14: Ch. 1, Rows



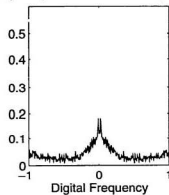
Freq. Response: Ch. 2, Rows



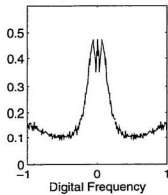
Freq. Response: Ch. 3, Rows



Freq. Response Nov. 14: Ch. 1, Columns



Freq. Response: Ch. 2, Columns



Freq. Response: Ch. 3, Columns

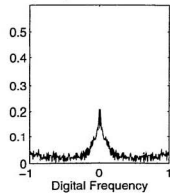


Figure III.3: Magnitude of frequency response, for filters used in recovery of Nov. 14 bandpass process presented in Figure 4.9.

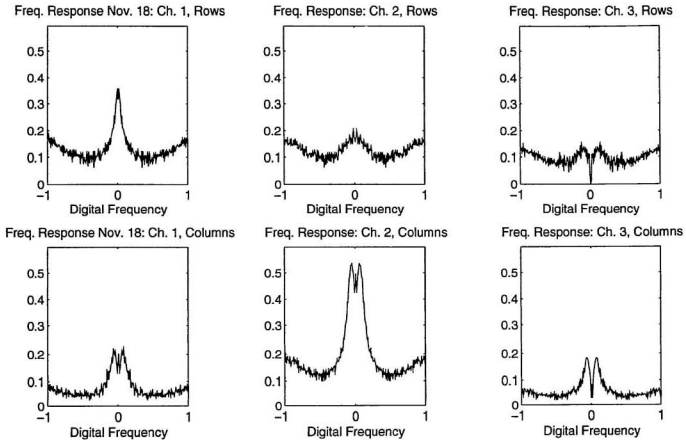


Figure III.4: Magnitude of frequency response, for filters used in recovery of Nov. 18 bandpass process presented in Figure 4.13.

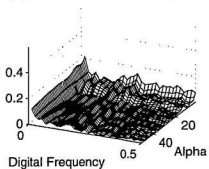
APPENDIX IV

FREQUENCY RESPONSE OF VECTOR FILTER AS FUNCTION OF VARIATIONS IN α AND β

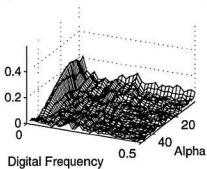
IV.1 Overview

This Appendix presents magnitude frequency response surfaces for transfer functions h_{21} , h_{22} , and h_{23} , corresponding respectively to Channels 1, 2, and 3, of the vector Wiener filter. These were derived for varying combinations of α and β , as described in Chapter Five. Results obtained for both the row and column filters have been displayed, for varying α in the range of $3 \leq \alpha \leq 50$ with $\beta=3$, and for jointly varying $\beta=\alpha$ in the range of $3 \leq (\beta=\alpha) \leq 50$. Figures IV.1 and IV.2 present results based on correlation data from the rows and columns respectively, of the unfiltered Nov. 14 image. Similarly, Figures IV.3 and IV.4 show results for the rows and columns of the unfiltered Nov. 18 image.

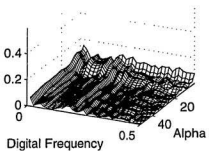
(a) Nov. 14 Rows: Channel 1, Beta=3



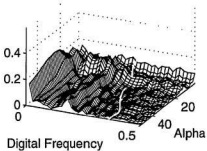
(d) Nov. 14 Rows: Channel 1, Beta=Alpha



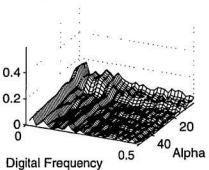
(b) Rows: Channel 2, Beta=3



(e) Rows: Channel 2, Beta=Alpha



(c) Rows: Channel 3, Beta=3



(f) Rows: Channel 3, Beta=Alpha

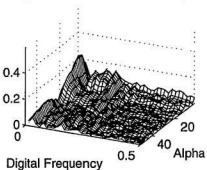


Figure IV.1: Magnitude frequency response surfaces of Nov. 14 row filter, for varying α with fixed β , shown in (a), (b) and (c), and jointly varying $\beta=\alpha$, shown in (d), (e), and (f).

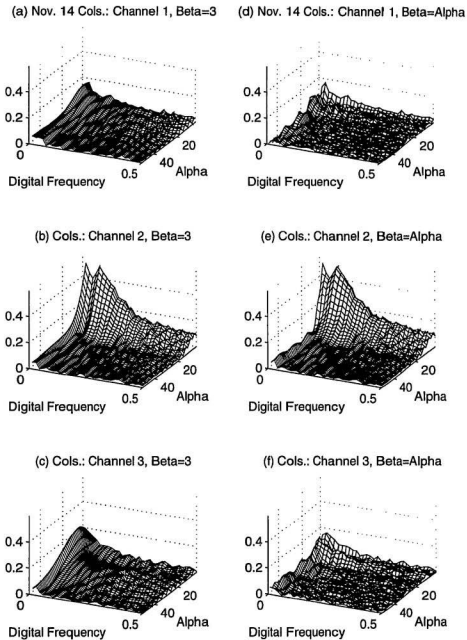
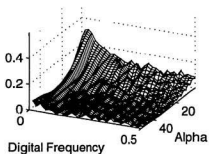
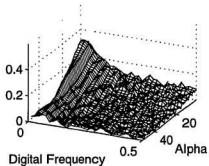


Figure IV.2: Magnitude frequency response surfaces of Nov. 14 column filter, for varying α with fixed β , shown in (a), (b) and (c), and jointly varying $\beta=\alpha$, shown in (d), (e), and (f).

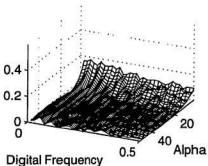
(a) Nov. 18 Rows: Channel 1, Beta=3



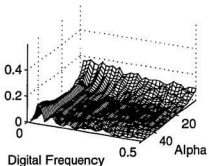
(d) Nov. 18 Rows: Channel 1, Beta=Alpha



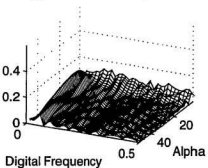
(b) Rows: Channel 2, Beta=3



(e) Rows: Channel 2, Beta=Alpha



(c) Rows: Channel 3, Beta=3



(f) Rows: Channel 3, Beta=Alpha

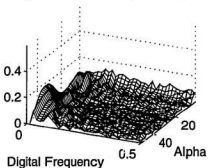


Figure IV.3: Magnitude frequency response surfaces of Nov. 18 row filter, for varying α with fixed β , shown in (a), (b) and (c), and jointly varying $\beta=\alpha$, shown in (d), (e), and (f).

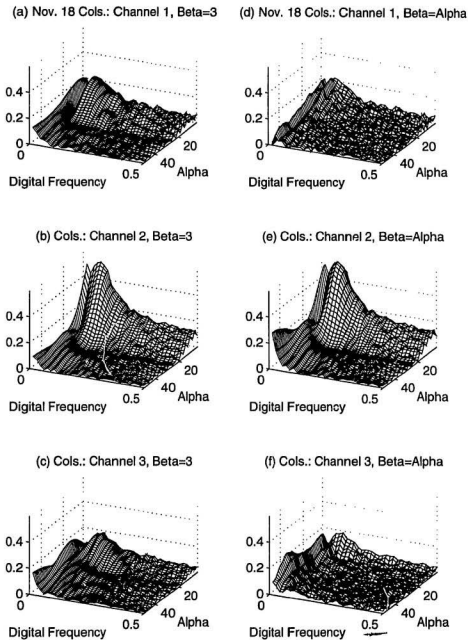


Figure IV.4: Magnitude frequency response surfaces of Nov. 18 column filter, for varying α with fixed β , shown in (a), (b) and (c), and jointly varying $\beta=\alpha$, shown in (d), (e), and (f).

APPENDIX V

FFT ANALYSIS OF RECOVERED IMAGES PRESENTED IN CHAPTER FIVE

V.1 Overview

This Appendix presents an FFT analysis of each image which has been presented in Chapter Five for selected combinations of α and β . Figures V.1, V.2, V.3, and V.4 present a row and column analysis for the recovered wavefields shown in Figures 5.4, 5.5, 5.6, and 5.8 respectively. These are based on 1024-point FFT's for the digital frequencies $-1 < f \leq 1$, of which a bandwidth corresponding to $-0.25 \leq f \leq 0.25$ has been displayed here.

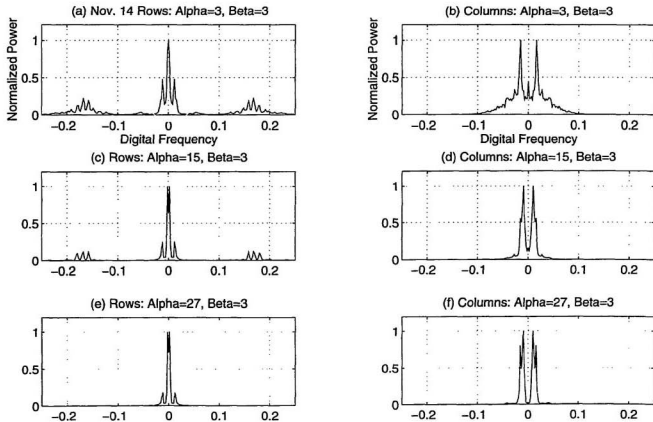


Figure V.1: FFT analysis for recovered images shown in Figure 5.4.

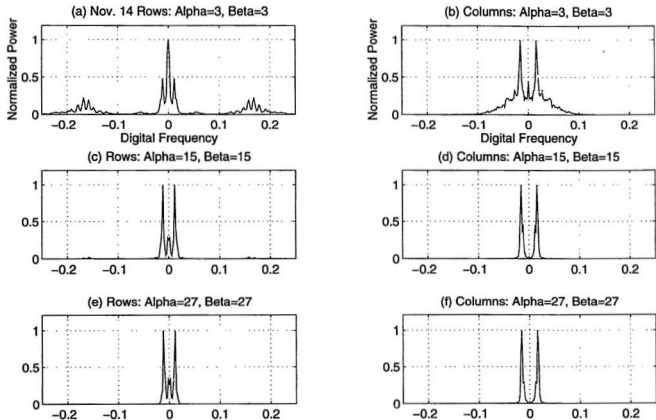


Figure V.2: FFT analysis for recovered images shown in Figure 5.5.

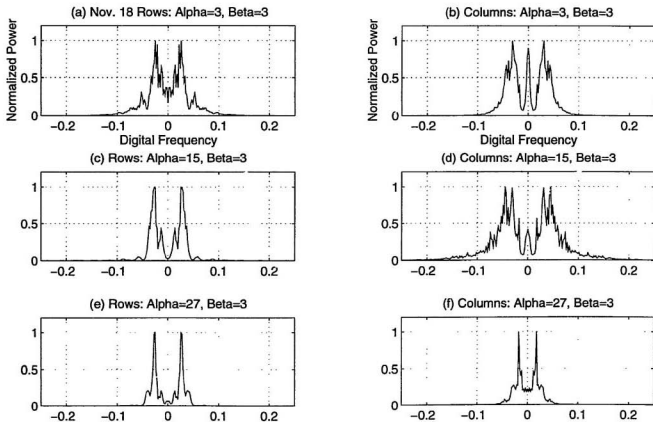


Figure V.3: FFT analysis for recovered images shown in Figure 5.6.

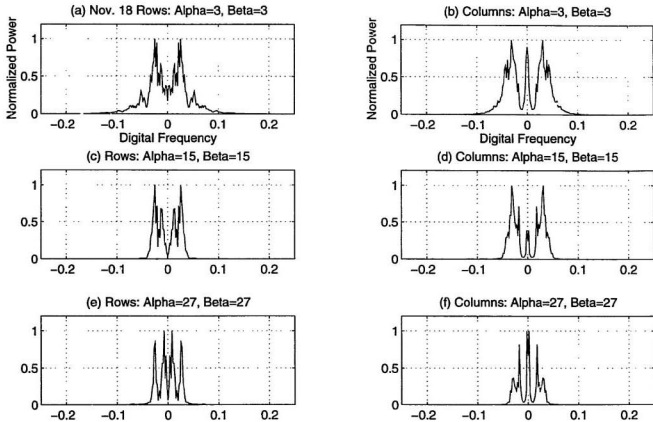


Figure V.4: FFT analysis for recovered images shown in Figure 5.8.



